TECHNISCHE UNIVERSITÄT MÜNCHEN

Physik Department E20
-
Molekulare Nanowissenschaften & Chemische Physik von Grenzflächen

Adsorbates on Noble and Ferromagnetic Metals: From Structural and Electronic Properties to Ultrafast Spin-Dependent Electron Transport

Florian Blobner

Vollständiger Abdruck der von der Fakultät für Physik der Technischen Universität München zur Erlangung des akademischen Grades eines

Doktors der Naturwissenschaften (Dr. rer. nat.)

genehmigten Dissertation.

Vorsitzender:		Univ.-Prof. Dr. Wilhelm Zwerger
Prüfer der Dissertation:	1.	apl. Prof. Dr. Peter A. Feulner
	2.	Univ.-Prof. Dr. Ulrich K. Heiz
	3.	Univ.-Prof. Dr. Wilfried Wurth, Universität Hamburg

Die Dissertation wurde am 10.04.2013 bei der Technischen Universität München eingereicht und durch die Fakultät für Physik am 18.06.2013 angenommen.

Abstract

The electronic and structural properties of adsorbates on metal surfaces, including the dynamics of electron transfer processes, are of key importance in the field of nanotechnology as well as from a fundamental point of view. In this thesis, self-assembled monolayers on noble metals and ferromagnetic substrates serve as model systems for investigating the ordering, bonding mechanisms, thermal stability and charge transfer dynamics in adsorbate/substrate complexes. The headgroup-substrate interaction is investigated in detail for two different types of self-assembled monolayers on a Ni(111) surface and is found to show significant differences, thus influencing the practical applicability of these systems in nanotechnology. To identify possible candidates for application in molecular electronics, tailgroup-to-substrate charge transfer dynamics is examined by means of the core hole clock method for self-assembled monolayers on Au(111) and Ni(111). Finally, ultrafast, spin-dependent charge transfer is investigated for argon monolayers physisorbed on thin ferromagnetic films in a proof of principle experiment. The results show the way towards atom-, orbital- and spin-sensitive electron transport investigations with the core hole clock method.

Kurzfassung

Die elektronischen und strukturellen Eigenschaften von Adsorbaten auf Metalloberflächen, sowie die Dynamik von Ladungstransferprozessen, sind von grundlegendem Interesse sowohl im Bereich der Nanotechnologie als auch der Grundlagenforschung. Im Rahmen dieser Arbeit dienen selbstorganisierende Monoschichten auf Edelmetallen und ferromagnetischen Oberflächen als Modellsysteme zur Untersuchung von Ordnung, Bindungsmechanismen, thermischer Stabilität, sowie Ladungstransferdynamik in Adsorbat/Substrat Komplexen. Detaillierte Untersuchungen zur Bindungsgruppen-Substrat Wechselwirkung für zwei verschiedene Typen von selbstorganisierenden Monoschichten auf Ni(111) zeigen signifikante Unterschiede, welche die praktische Anwendbarkeit der Systeme im Rahmen der Nanotechnologie beeinflussen. Um geeignete Systeme für die Anwendung im Bereich der molekularen Elektronik zu identifizieren, wird der Ladungstransfer von der Endgruppe zum Substrat mit Hilfe der Core Hole Clock Methode für selbstorganisierende Monoschichten auf Au(111) und Ni(111) untersucht. Abschließend wird der spinabhängige Ladungstransfer von physisorbierten Argon Monoschichten auf dünnen, ferromagnetischen Filmen im Rahmen eines “Proof of Principle” Experimentes untersucht. Die Ergebnisse weisen dabei den Weg in Richtung Atom-, Orbital- und Spin-aufgelösten Elektronentransport Messungen mit Hilfe der Core Hole Clock Methode.

Contents

List of Figures

List of Tables

Chapter 1

Introduction

Ever since the discovery of the transistor effect in 1947 by Bardeen, Brattain and Shockley [1], miniaturization of structures and their control at a microscopic level have been of key importance for the further development of modern technologies. Not only the fabrication of computer chips and the miniaturization of integrated circuits, but also the development of "new materials", such as biocompatible implants [2,3], organic solar cells [4] or graphene [5], to name but a few, require the precise understanding and control of physical and chemical processes at the atomic level. The surfaces or interfaces of these materials are of special interest, since they determine the microscopic and macroscopic properties to a great extent. In many cases, like, e.g. the above mentioned transistor effect, the operation principle of organic light emitting diodes and the interaction of human tissue with implants, the *interface* rather than the *bulk* is largely responsible for their functionality. The rise of nanotechnology as an interdisciplinary field between physics, chemistry and biology, impressively shows the significance of the control of matter on the nanometer (nm) scale, where 1 nm corresponds to 1×10^{-9} m.

Two contrasting techniques are essentially available for creating well-defined structures on the nanometer scale: First, the so called *top-down* approach, where small structures are built by removing material from initially larger entities with appropriate tools like lithography. Todays semiconductor industry successfully employs this method for fabricating devices with dimensions down to 22 nm, as for example the Intel Core i7-3770K [6]. Nevertheless, decreasing the fabrication size comes with a large increase in cost and complexity, therefore motivating the development of new approaches. One possibility to avoid these problems is provided by the second method, the so-called *bottom-up* approach [7]. Here, single atoms and molecules are used as individual building blocks for assembling complex structures. This can be achieved by manipulating each entity with tools like a scanning tunneling microscope, which lacks the practical use, or, by exploiting the self-assembling properties of the building blocks themselves. The large progress in synthetic organic

chemistry enabled the production of individually tailored molecules that can be used to precisely steer the self-assembly [8]. The *bottom-up* approach using self-assembly has many advantages like lower cost, minimal instrumentation, easy parallelization and enhanced control compared to the *top-down* method [7]. Yet, the development is in its infancy stage, with many problems to be solved and many gaps of understanding to be covered, whereas conventional *top-down* methods rely on decades of research and development and are still used for fabricating the majority of state-of-the-art technology. Nevertheless, exploiting the self-assembly capabilities even for relatively complex biomolecules like DNA has resulted in the possibility of creating arbitrary two- and three-dimensional shapes, thus having a tremendous potential [9, 10].

One of the main issues is therefore the interaction of the atoms or molecules with each other and with the underlying surface, since this determines important properties like thermal stability, electrical conductance, interfacial properties and film quality. The large toolbox that modern surface science has to offer [11], allows detailed investigations of complex systems, yielding results on the structural as well as the electronic properties and their dynamic evolution. Combining the results from experiment and theory helps to identify the appropriate building blocks and substrates for a specific purpose, ranging from systems like corrosion-inhibiting self-assembled monolayers [12] to molecular spin-transistors [13].

Within this thesis, self-assembled monolayers (SAMs) on noble- and ferromagnetic substrates are investigated with respect to their geometric and electronic structure, thermal stability and charge transfer dynamics. SAMs represent a prototypical system for nanotechnology, since they combine the advantages of easy fabrication, low cost and versatile applications on the nanometer scale [14–17]. Small organic molecules consisting of few tens of atoms are used as building blocks, which are then bonded to the surface to obtain ordered structures. Especially the effect of the coupling to the substrate as well as charge transfer through the monolayers are the focus of this work. Information on the "conductivity" of these entities is important for identifying molecules that could be used in organic electronics, whereby the coupling to the surface also influences this conductivity and affects the stability of the monolayers. Furthermore, charge transfer through molecules in combination with ferromagnetic substrates or electrodes opens up a route towards molecular spintronics.

Often, the electron transport through molecular entities coupled to metal electrodes is quite complex, thus hindering a quantitative understanding of the underlying physical mechanisms. Therefore, simpler model systems with

a weak interaction between the adsorbate and substrate are often desired. Noble gases adsorbed on metal surfaces have proven to be most suited for interpreting complex behavior of electron transport and are also used in this work for investigating spin-dependent electron transport.

The thesis is structured as follows: Chapter 2 introduces the basic concepts of self-assembled monolayers on metal substrates with emphasis on bonding mechanisms on noble and ferromagnetic substrates as well as charge transfer dynamics. Physisorbed argon on metal substrates as one of the simplest model systems for adsorbate/substrate complexes is also briefly introduced. Afterwards, Chapter 3 gives a survey of the experimental techniques that are used within this work, together with an instrumental development for the acquisition of x-ray absorption spectra, namely a novel partial electron yield detector.

In the first experiment (Chapter 4), the well-studied system of cyano terminated alkanethiol SAMs on gold is used to investigate the tailgroup-to-substrate charge transfer dynamics with linearly polarized synchrotron radiation. Thereby, the core hole clock method is shown to be capable of resolving subtle polarization-dependent differences of the charge transfer times.

Chapter 5 constitutes the main part of the work and reports on the preparation and characterization of self-assembled monolayers on Ni(111) as a reactive, ferromagnetic transition metal substrate. Fluorine-terminated, aromatic SAMs with thiol- and carboxyl headgroups as connecting links to the metal are investigated and their electronic structure, adsorption geometry, thermal stability and charge transfer dynamics are analyzed and compared.

As a proof of principle experiment, spin-dependent electron transport between core-excited argon monolayers and thin ferromagnetic films is investigated in Chapter 6. This study further extends the toolbox of the core hole clock method to allow spin-sensitive charge transfer investigations.

Finally, Chapter 7 summarizes the results and addresses emerging questions. The implications of this work are discussed and an outlook for future research is given.

Chapter 2

Fundamentals of the Investigated Systems

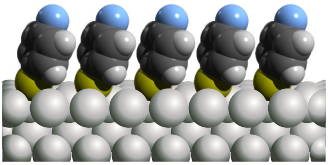

Abstract In this chapter, the basic properties of the systems investigated in this thesis are briefly described, beginning with an overview on self-assembled monolayers on metal surfaces. First, the preparation, bonding and structure of SAMs will be discussed, followed by comments on the charge transfer dynamics and by a section on the use of ferromagnets as substrates for the growth of self-assembled monolayers. Argon adsorbed on metal surfaces will be introduced in the second part, and its relevance as a model system for investigating charge transfer dynamics will be motivated.

2.1 Self-Assembled Monolayers on Metal Substrates

The first section introduces self-assembled monolayers, which are the basis for the majority of investigations performed during this thesis. Here, only general concepts will be presented, more detailed information on the analyzed systems can be found in the introduction of the respective chapters.

In 1946, Zisman and coworkers published a manuscript entitled "Oleophobic monolayers: I. Films adsorbed from solution in non-polar liquids" [18], which is often credited for originating the SAM concept [16]. Nevertheless, the full potential of self-assembly was only recognized considerably later, triggered by work of Nuzzo and Allara in the early 1980s on the preparation of SAMs of alkanethiols on gold from solution [19]. Since these discoveries, the interest in SAMs has risen continuously until today.

One of the main reasons for the large interest is that SAMs allow an easy and inexpensive modification and functionalization of surfaces, which enables the production of individually-tailored interfaces. The applications range from surface coatings for controlling the adhesion and wetting properties as well as ensuring biocompatibility to molecular recognition for sensors and nanofabrication for molecular electronics [14–17]. This interdisciplinary field allows fundamental research on, e.g. charge transfer dynamics between layer and substrate as well as application-based investigations for enhancing the corrosion-protection of metal coatings.

2.1.1 Preparation, Bonding and Structure of SAMs

According to a commonly accepted definition, self-assembled monolayers are ordered molecular structures spontaneously formed by adsorption of precursor molecules with specific affinity to a solid (metal) substrate [14, 15]. Usually, SAMs consist of a headgroup, which defines the bond to the surface, a spacer unit that separates the substrate from the SAM-vacuum interface and finally a tailgroup which is responsible for the interfacial properties. An idealized, schematic representation of typical SAMs is shown in Figure 2.1. Depending on the nature of the spacer units, self-assembled monolayers can be categorized into two groups: aromatic and aliphatic SAMs. The headgroup is especially important, since it establishes the bonding of the molecules to the surface. Furthermore, it stabilizes the surface atoms and modifies the electronic states of both surface and molecule via hybridization [17]. The interfacial properties can then be tuned by selecting an appropriate tailgroup, which acts

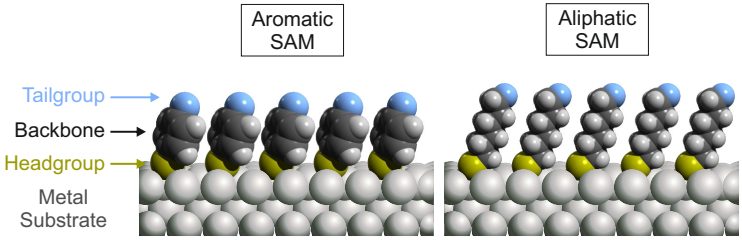

Figure 2.1: Schematic depiction of ideal self-assembled monolayers adsorbed on a metal surface, which differ by the nature of their spacer units. Aromatic (left) and aliphatic (right) refer to the backbone, which is a single phenyl ring in the aromatic SAM, in contrast to a methylene chain in the aliphatic SAM for the depicted molecules.

as the SAM-vacuum (or ambient) interface. In the following, we will briefly discuss the preparation and the constituents of SAMs.

Preparation Methods SAMs can either be fabricated wet-chemically, i.e. by immersion of the freshly-prepared gold substrate into a solvent-precursor molecule mixture for several hours, or by vapor deposition under ultrahigh vacuum (UHV) conditions. The first preparation method is rather simple and results generally in SAMs of good quality, whereas the second is more challenging but gives access to further properties like the behavior during the initial stages of growth or phase changes during deposition. Furthermore, deposition in UHV enables the use of atomically clean *reactive* substrates, which are hard to control during the immersion procedure. The commonly-used substrates for SAMs adsorbed from solution are thin films of noble metals (10 to 200 nm thickness) that have been evaporated on a silicon or glass substrate using an adhesion layer. This procedure typically results in films with an island or grain size from 10 to 1000 nm and a dominant (111) texture [17]. Conversely, SAMs on arbitrary single crystal surfaces (e.g. stepped surfaces) can be prepared under UHV conditions.

Influence of the Substrate The vast majority of studies on self-assembled monolayers is conducted on gold substrates, mostly due to the inertness of the metal and the simplicity of the procedure which yields good-quality gold films, as described above. Furthermore, gold binds thiols, which are the standard headgroup for SAMs on gold, with a high affinity [20], without formation of unwanted species like sulfides. Silver and copper come next in the row of most-studied substrates, nevertheless they introduce a variety

of complications because of their higher reactivity [17]. Copper itself would be interesting especially for molecular electronic applications, since it is a common material for interconnects in conventional electronics. Moving one step further, molecular spintronics based on self-assembled monolayers would require ferromagnetic substrates, which are even more reactive and prone to oxidation. The much more difficult preparation conditions for such substrates in part explain the comparably small number of studies conducted for theses interesting systems.

Headgroup As already mentioned, most SAMs on noble metals are prepared by using a thiol headgroup for bonding to the surface. The thiol group undergoes deprotonation upon adsorption at room temperature and subsequently forms a thiolate bond [17]. This Au-S bond is a relatively strong bond with a homolytic bond strength of approximately 40 kcal/mol [14]. Apart from the well-studied thiol headgroup, disulphides [21], amines [22], silanes [16], or acids (e.g. carboxylic acids) [14] can also be used for coupling the precursor molecules to the substrate. Most of these other coupling mechanisms result in a much weaker bond; the Au-O and Au-N bond strengths are only of the order of 2 and 8 kcal/mol, respectively [22]. When precursor molecules that contain two coupling units are adsorbed, e.g. COOH-terminated thiols on gold, the headgroup that forms the stronger bond to the substrate typically "wins" the competition process and binds to the surface, while the COOH group acts as a tailgroup in the above mentioned case [23].

Backbone The backbone of the SAMs separates the functional tailgroup from the metal interface and acts as a physical barrier. Furthermore, the thickness (typically 1 to 3 nm) of the organic layer can be controlled by specifically designing the backbone, e.g. by adding or removing methylene or phenyl units. Typically, alkane chains or phenyl rings are used as spacer units, giving rise to the aliphatic or aromatic classification of the SAMs (see above and Figure 2.1). One of the main differences between aromatic and aliphatic spacer units which is of interest here, is their conductivity, as it will be discussed in Section 2.1.2.

Tailgroup The tailgroup defines the organic-vacuum (or ambient) interface and determines the surface properties of the system. Macroscopic behavior, such as wettability [24], can be precisely engineered by selecting the appropriate tailgroups. Furthermore, biological interfaces can be mimicked for studying, e.g. the adsorption of proteins or cells [25, 26] on surfaces, and the work function of the system can be tuned by varying the functional group

of the monolayers [27, 28]. The latter has proven especially useful for controlling the charge-carrier injection barriers in semiconductor devices, which can lead to a significant increase in efficiency [29, 30]. In addition to that, tailgroups can also be used as spectroscopic markers, e.g. for unambiguously defining the starting point of a charge transfer reaction, as discussed in Section 2.1.2.

Structure One often speaks of well-ordered SAMs if the molecules adopt a uniform adsorption geometry (tilt angle of the molecule with respect to the surface) and form a superstructure with respect to the underlying substrate. The resulting structure of the SAM is mainly determined by the geometric arrangement of the headgroup moieties on the substrate and the van der Waal and hydrogen bond interactions between neighboring molecules due to a minimization of the free energy [17]. Alkanethiol SAMs on gold for example are known to form a superstructure based on a $\left(\sqrt{3} \times \sqrt{3}\right) \mathrm{R}\,30^\circ$ overlayer in their high-coverage phase, with the molecules standing upright in most cases [17]. In contrast, the same molecules tend to adopt a flat-lying configuration with a rectangular unit cell in the low coverage phase, also know as the striped phase [31]. In order to functionalize the surface in a controlled way or for probing charge transport through the layers, upright standing SAMs that expose the tailgroup are preferable in most cases.

2.1.2 Charge Transfer Dynamics in SAMs

During the last two decades, the field of molecular electronics, based on the use of molecules instead of the standard semiconductor materials for electronic devices, has received considerable attention (see, e.g. Refs. [32–35]). Nevertheless, the beginning dates back to the early 1970s, with the seminal paper by Aviram and Ratner [36], in which they predict rectifying behavior for a simple organic molecule. The smaller intrinsic size of molecules and the possible cost-efficient production compared to standard semiconductor technology [32] are among the main reasons for the large interest, together with the higher flexibility offered by the richness of molecular building blocks. In order to achieve this goal, molecules that possess the typical properties of electronic circuit elements, such as conducting, insulating, rectifying or amplifying behavior, need to be identified. Therefore, the relationship between the measured electron transfer characteristics and the molecular structure, the influence of the coupling to the substrate and the mechanism of electron transport have to be understood.

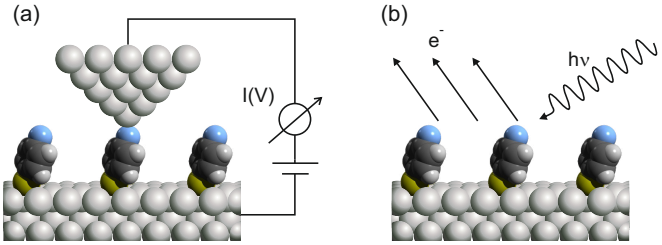

Figure 2.2: Illustration of different techniques for measuring the charge transport through molecules. **(a)** Establishing contact to individual molecules within a self-assembled monolayer via a scanning tunneling microscope tip. The charge transfer is measured by the acquisition of I-V curves. **(b)** Illustration of a spectroscopic method for obtaining charge transfer times for electron transport through molecular entities. The SAMs are irradiated with x-ray radiation and the decay electrons are monitored, which allows conclusions on the charge transfer through the molecules.

One large class of experiments uses a metal-molecule-metal junction in order to measure current-voltage (I-V) curves, either by contacting single molecules within a self-assembled monolayer with a scanning tunneling microscope (STM) tip (see Figure 2.2 (a)) or by using, e.g. mechanically controlled break junctions with individual molecules in between [37, 38]. Since these experiments will not be considered in this thesis, we will not go into further detail. Nevertheless, one crucial point for this type of experiments is the contact between the molecule and the metal. In fact, the exact contact geometry significantly influences the observed I-V curves, complicating the analysis of the results considerably [37–40].

A different approach is depicted in Figure 2.2 (b), where the SAMs are irradiated with narrow-bandwidth synchrotron radiation, thus promoting electrons into unoccupied electronic levels. When, e.g. a core-level electron of the tail-group is excited, it will delocalize into the substrate after a certain amount of time via tunneling through the molecule, if energetically possible. By recording the decay electrons emitted following the core hole decay, the charge transfer time of the initially excited electron can be extracted. A detailed description of this method, the *core hole clock method*, will be given in Section 3.3; here we will focus on results obtained with this method for charge transfer in self-assembled monolayers. One advantage of this method is the ability to probe the charge transfer without the need of a second contact to the molecule which might influence the measured conductance.

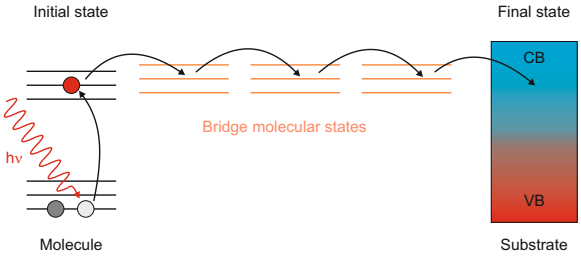

Figure 2.3: Schematic illustration of the electron transfer process from a core-excited molecule to a metal substrate by tunneling via several bridge molecular states. CB and VB denote the conduction and valence band of the metal, respectively. Figure after [41].

It is generally accepted that the electron transport through small molecules with a strong coupling to the substrate, such as those depicted in Figure 2.2, occurs via electron tunneling; implying that the molecule only mediates the transport, but the charge does not reside on the molecule for a significant amount of time [17, 39, 41]. This can be different for large complex molecules like proteins, where the charge transport is best described by sequential hopping [35, 42, 43]. Figure 2.3 schematically shows the electron transfer process from a small, core-excited molecule to a substrate. The charge transfer can involve several transient bridge molecular states, which mediate the tunneling process to the conduction band of the metal. Accordingly, the electron transfer strongly depends on the electronic interaction between the discrete molecular states and the substrate continuum, as well as on the coupling between the bridge molecular states. Entities with transiently occupied states delocalized throughout the molecule yield an efficient electron transfer and hence good conductivity. Therefore, aromatic SAMs often show faster charge transfer times or, in other words, a higher conductivity compared to aliphatic SAMs of comparable length [39, 44–46]. Simple aromatic SAMs can therefore be seen as "molecular wires", whereas aliphatic SAMs often correspond to "molecular insulators".

2.1.3 From Noble Metals to Ferromagnetic Substrates

In the discussion above on charge transport and molecular electronics, we have only focused on the charge of the electron as a potential carrier of information. Besides that, the electron's spin is also considered to be a valuable degree of freedom, which might even be superior to the mere charge [47, 48].

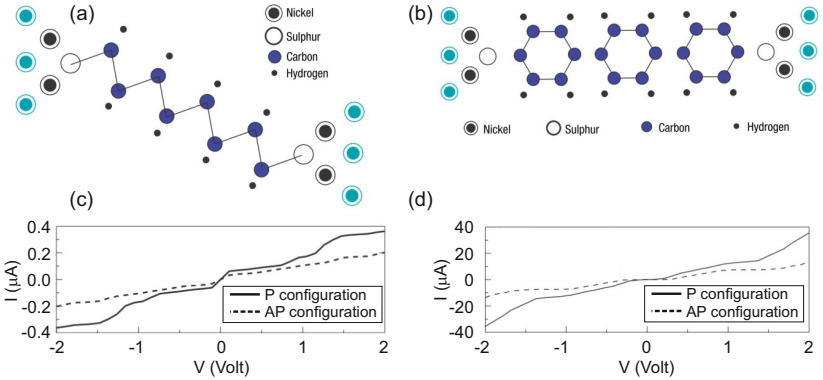

Figure 2.4: Schematic structure of octane **(a)** and tricence **(b)** coupled with thiol groups to two Ni(001) terminal surfaces for measuring spin-dependent currents through organic molecules. The calculated magneto-transport properties (I-V curves) for octane and tricence are shown in **(c)** and **(d)**, respectively, for parallel (P) and antiparallel (AP) magnetization alignment of the two terminals. Figure from Ref. [50]

.

So far, most studies focused on conventional, inorganic semiconductor devices for exploiting the spin properties [47, 48], but recently, spin in organic electronics has received considerable interest, theoretically [49–53] and experimentally [13, 53–57]. Due to the weak spin-orbit and hyperfine interactions in organic materials, spin-coherence can be preserved over times and distances that are much longer compared to conventional metals or semiconductors [50]. One way of measuring spin-dependent currents through molecules is by replacing the noble metal substrate (and electrode) in Figure 2.2 with ferromagnetic contacts and measuring the current for parallel or antiparallel alignment of the magnetization of the two terminals. This procedure is depicted for two types of molecules in Figure 2.4. Generally, one expects a larger current for parallel magnetization of both terminals compared to the antiparallel alignment, as shown for the calculated I-V curves in (c) and (d) of Figure 2.4. Correspondingly, the SAMs have to be adsorbed on reactive ferromagnetic substrates, such as nickel, cobalt or iron, with all the complications mentioned in Section 2.1.1.

Figure 2.5 shows the calculated spin-resolved density of states (DOS) of bulk nickel. Besides the large DOS near the Fermi level, which is responsible for the high reactivity of nickel, the different densities for spin-up (majority) and spin-down (minority) electrons is apparent. This is especially striking in the

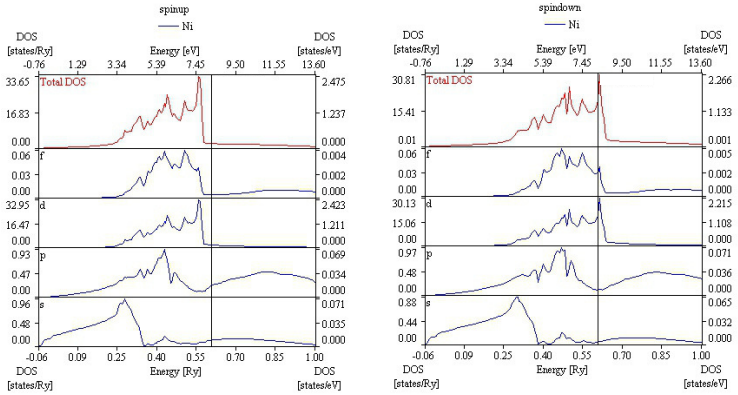

Figure 2.5: Calculated spin-resolved density of states for bulk nickel. The total DOS as well as the contributions from f, d, p and s-bands are depicted for spin-up (left) and spin-down (right) electrons. The vertical line represents the Fermi level in both plots. Figure from Ref. [58].

.

regime close above the Fermi level (vertical line in fig. 2.5), where minority holes dominate the empty DOS. Since this unoccupied density of states significantly influences the charge transfer properties (cf. Section 2.1.2), a different behavior can be expected for majority and minority electrons tunneling from the adsorbate into the substrate.

Nevertheless, the combined density of states of the adsorbate/substrate system can be quite different, due to the strong interaction of the chemisorbed SAMs with the substrate. So far, only few reliable studies exist for the structure and bonding of SAMs on ferromagnetic substrates, as will be reviewed in Section 5.1. Although, proceeding from reasonably inert noble metals to highly reactive substrates like Ni(111) will not only help identifying possible candidates for molecular spintronics, but also results in a better understanding of the mechanisms that are responsible for the ordering, thermal stability and charge transfer dynamics in self-assembled monolayers in general.

2.2 Argon on Surfaces as a Model System for Charge Transfer Dynamics

Especially when investigating complex reactions, like charge transport from adsorbates to substrates (cf. Section 2.1.2), simple model systems with known or predictable properties are desirable for a deeper insight into the observed effects. Within the last years, the rare gas argon adsorbed on metal surfaces has proven to be versatile for analyzing ultrafast charge transfer in adsorbate/substrate combinations [59–65]. One of its advantages is certainly the weak interaction between adsorbate and substrate due to physisorption, which rarely modifies the electronic structure of both constituents, compared to chemisorbed entities [66]. Therefore, it enables the comparison of experimental results with high-quality, ab-initio theoretical studies, as for e.g. the charge transfer dynamics of argon on ruthenium [66].

Within this thesis, charge transfer investigations of argon adsorbed on thin ferromagnetic films serve as a proof-of-principle experiment for demonstrating spin-sensitive charge transport across the atom/metal surface in Chapter 6. Furthermore, a route towards possible spin-dependent electron transport measurements for self-assembled monolayers on ferromagnetic substrates is presented.

Chapter 3

Experimental Methods

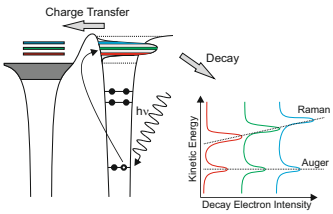

Abstract In this chapter, the experimental methods that were used for investigating the systems of this thesis are briefly described. Most of the experiments exploited photoexcited electrons as surface sensitive probes, which can be used to explore the geometric as well as the electronic structure and electron dynamics of complex adsorbate-substrate systems.

Well-established surface science techniques like photoelectron spectroscopy in combination with state-of-the-art methods such as spin-dependent resonant Auger spectroscopy can give new insights into fundamental physics at a microscopic level. Since most modern electron spectroscopy techniques require a high-brilliance, tunable excitation source, experiments are typically conducted at third-generation synchrotron radiation facilities. In the last part of this chapter, the development of a novel partial electron yield detector will be introduced.

3.1 Introduction

Electron spectroscopy in general deals with the detection of electrons which originate from a primary excitation step within an atom or molecule. In this thesis, soft x-rays were used to promote initially bound electrons into unoccupied bound states below the vacuum level or into free continuum states above the vacuum level. In the first case, information about the excitation step can be obtained by monitoring electrons which stem from decay processes, whereas in the latter the excited electrons can be detected directly. These techniques owe their surface sensitivity to the fact that the inelastic mean free path of electrons with kinetic energies between 10 and 2000 eV in solids is on the order of few tens of Ångstroms or even below [67].

Depending on the excitation and detection conditions, a variety of methods have been developed over the past decades. The techniques, which are relevant for this work, will be briefly described in the following sections. A detailed and comprehensive review of most modern electron spectroscopy techniques can be found in excellent textbooks, such as Ref. [11].

3.2 Photo- and Auger Electron Spectroscopy

Whenever the primary excited electron is directly detected, the method is labeled either x-ray photoelectron spectroscopy (XPS) or ultraviolet photoelectron spectroscopy (UPS), depending on the energy of the exciting photons.

Commonly used excitation sources for XPS are magnesium or aluminum anodes as laboratory sources on the one hand, and large scale synchrotron facilities on the other hand. Since the energy of the radiation is in the soft x-ray regime (0.1 - 2 keV), strongly bound core electrons are probed which contain information on, e.g. the elemental composition, the chemical environment and the oxidation state.

For UPS, discharge lamps operated with noble gases produce photons in the energy range of 10 to 50 eV and give access to weakly bound valence electrons. Since these electrons participate in the formation of bonds, UPS is especially useful for monitoring the changes of the frontier orbitals upon adsorption of atoms or molecules on surfaces. Furthermore, the work function of the system can be accurately determined[1], thus giving insight into the charge

[1] It should be noted that the work function can usually be extracted using various excitation sources. The advantage of UPS is the exact knowledge of the excitation energy, which avoids problems related to the zero-point offset of the electron analyzer.

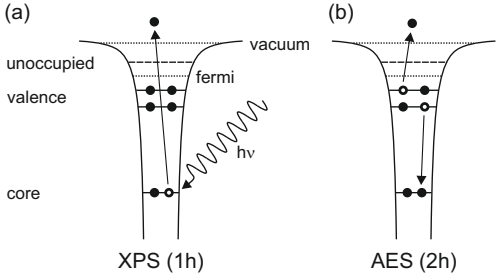

Figure 3.1: Schematic depiction of the excitation and subsequent ejection of **(a)** a primary electron and **(b)** a secondary electron after adsorption of a photon of energy $h\nu$. The different final states of the two processes are also indicated in brackets.

distribution in the region at the interface between adsorbate and substrate, as will be discussed in more detail below.

Photon absorption and subsequent electron emission are schematically depicted for XPS in Figure 3.1 (a). By detecting the emitted electrons with an energy-sensitive detector, their kinetic energy E_{kin} can be determined, whereas the binding energy E_{bind} follows from energy conservation:

$$E_{kin} = h\nu - E_{bind} \tag{3.1}$$

$$E_{bind} = h\nu - E_{kin} \tag{3.2}$$

Here, we referenced the binding and kinetic energies to the Fermi level E_{fermi}, which is common practice for solid samples that are in electrical contact with the electron analyzer. If the vacuum level E_{vac} is taken as a reference for the kinetic energy, the work function $\Phi = E_{vac} - E_{fermi}$, which is required to promote an electron from the Fermi level to the vacuum level, enters Equations (3.1) and (3.2).

Since the binding energies for pure elements and such in compounds are tabulated [68], it is rather straightforward to identify the chemical composition of the sample once the XPS spectrum has been acquired. Furthermore, the binding energy is also sensitive to the chemical environment of a particular atom, an effect that leads to the occurrence of *chemical shifts* [68]. This enables for example the distinction between carbon atoms with different ligands in a complex organic molecule by their binding energies.

The primary excitation in Figure 3.1 (a) leads to a core hole with $E_{bind,c}$ remaining in the system, which is then no longer in its ground state, but in an excited 1-hole (1h) state. This state is not stable and will decay within the core hole lifetime τ_{core} by filling the core hole with an energetically higher-lying electron of binding energy $E_{bind,v1}$. The excess energy can then be transferred either to another electron with $E_{bind,v2}$, which will be emitted as an Auger electron, leading to a 2-hole (2h) final state, or in a radiative decay process to a photon. The non-radiative decay process, which prevails in low energy transitions ($E_{bind} < 500\,eV$) [69], is depicted in Figure 3.1 (b).

The kinetic energy E_{kin} of the Auger electron follows from [68]:

$$E_{kin,aug} = E_{bind} - E_{bind,v1} - E_{bind,v2} - U(v1, v2) \tag{3.3}$$

where $U(v1, v2)$ describes the interaction energy of the two remaining holes in the final state. Auger electron spectroscopy (AES) is commonly used for similar purposes as XPS, in particular for determining the chemical composition of samples. The fact that the kinetic energy of the Auger electrons is independent of the excitation energy allows the use of electrons rather than photons as exciting particles, which results in an easier experimental setup. In this work, AES is mainly used in combination with its resonant form, RAS, with the aim of obtaining information on charge transfer dynamics, as detailed in Section 3.3.

Work Function Measurements UPS is also an ideal tool for determining the work function of the investigated sample. Specifically, it allows following the work function change upon adsorption of molecules onto a clean substrate. Figure 3.2 shows the method commonly used for extracting the work function from an UPS spectrum [70]. The width W of the spectrum is defined as the energy range between secondary electron cut-off on the high binding energy side and the Fermi level on the low binding energy side. For a given excitation energy $h\nu$, the work function can be calculated as:

$$\Phi = h\nu - W \tag{3.4}$$

The precise knowledge of the excitation energy for typical discharge lamps (e.g. He-I line at 21.22 eV, He-II at 40.8 eV) enables the accurate (± 0.05 eV) determination of the sample work function with laboratory methods. Since residual magnetic fields strongly influence especially the low energy electrons, the sample is typically negatively biased between -5 V and -10 V to increase the kinetic energy of the escaping photoelectrons [70].

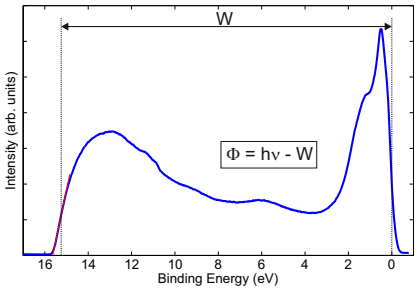

Figure 3.2: Extended UPS spectrum from clean Ni(111) sample illustrating the methodology for determining the work function. The linear part of the secondary electron cut-off (red line) is used to determine the intersection with the energy axis and together with the Fermi level determines the spectral width W. The width in turn yields the work function Φ of the sample, according to Equation (3.4).

Data Acquisition and Analysis The majority of the XPS and UPS spectra were collected using a state-of-the-art SPECS Phoibos 100 CCD electron energy analyzer, which is also capable of monitoring the emission angle (and therefore the wavevector) distribution of the outgoing photoelectrons. This type of analyzer has a high transmission and efficiency, which leads to short data acquisition times that are necessary to avoid beam damage within the organic layers. In our experimental setup, the electrons were usually recorded in a normal emission geometry, with the light impinging on the surface under a grazing incidence angle of 7° measured between the photon wave vector and the surface plane.

The subsequent data analysis of the spectra was performed following standard data processing and curve fitting routines for photoelectron spectra [71]. The core level XPS spectra acquired at the synchrotron were typically measured with an excitation energy about 100 eV above the respective ionization threshold to maximize both the surface sensitivity and photoionization cross sections [68]. All XPS energies were referenced to the corresponding Fermi level acquired at the same excitation energy to correct for analyzer work function changes as well as photon energy offsets. Afterwards, a linear plus Shirley-type background [72] was subtracted and the spectrum was fitted using multiple Voigt-type line profiles. This procedure enables a precise determination of the surface composition in the vast majority of cases.

3.3 Resonant Auger Spectroscopy

When the primary excitation process promotes the electron not to a state in the *continuum*, but to an unoccupied bound state *below* the vacuum level E_{vac}, the excitation is called resonant. For an isolated system, the possible non-radiative decay mechanisms after resonant excitation are shown in Figure 3.3. Depending on whether the initially excited electron takes part in the decay process or not, the decay channels are labeled *participator* and *spectator* decay, respectively. This difference is also evident in the final states of the two decay modes: a 1-hole final state for the participator and a 2-hole 1-electron final state for the spectator channel. Another peculiarity becomes apparent when the photon energy is scanned over the resonance width: The decay electrons show a linear dispersion in energy as a function of the photon energy, in stark contrast to normal Auger decay. This effect arises due to energy conservation in the isolated system and is called Auger resonant Raman effect [73].

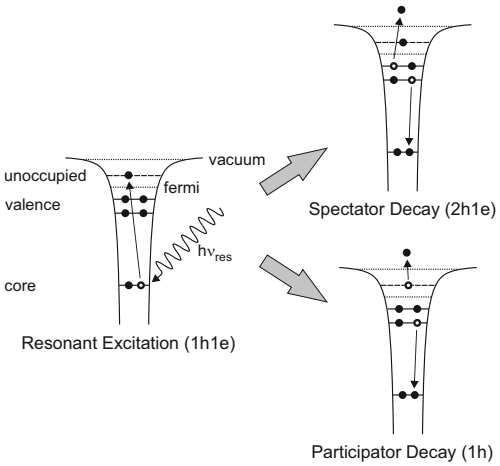

Figure 3.3: Illustration of two possible decay channels after resonant excitation of an isolated atom (similar for a molecule). The resonantly excited electron can either take part in the decay (participator decay, bottom), or remain in the resonance during the core hole lifetime (spectator decay, top).

The situation gets more involved when the system is coupled to a continuum, as in the case of a typical adsorbate/substrate combination. Here, an addi-

tional possibility exists: charge transfer of the initially excited electron into the substrate by, e.g. a tunneling process within the resonance lifetime τ_{ct}. The resulting decay channels are shown in Figure 3.4.

In the case where the core hole decay takes place *before* charge transfer occurs, the decay channel is called autoionization channel and follows the previous description of the isolated system. This process is shown on the left hand side of Figure 3.4. If the core hole decays *after* the charge has already been transferred into the substrate, the final state of the system (2h) is equivalent[2] to normal Auger decay and therefore labeled Auger channel (right hand side of Figure 3.4).

Since the two processes, core hole decay within τ_c and charge transfer within τ_{ct}, are independent in good approximation [74], the intensities in the autoionization I_{auto} and Auger I_{Auger} channels can be related by a simple rate approach [74]:

$$\frac{I_{auto}}{I_{Auger}} = \frac{\tau_{ct}}{\tau_c} \tag{3.5}$$

This gives direct access to the charge transfer time of the resonantly excited electron itself:

$$\tau_{ct} = \frac{I_{auto}}{I_{Auger}} \cdot \tau_c \tag{3.6}$$

In this picture, the core hole acts as an internal time reference, therefore the technique is often called core hole clock (CHC) method [74]. Since the core hole lifetimes are known for a variety of atoms [75], the charge transfer time can be calculated once the autoionization and Auger intensities have been determined. However, the measured decay spectra consist of a superposition of autoionization and Auger decays, with weighting factors according to their probabilities (see eq. (3.5)). In general there are two effects that help to disentangle them into I_{auto} and I_{Auger}, as shown schematically in Figure 3.5:

[2] "Equivalent" refers here to the energy of the final state, whereas the Auger branching ratios for example are not necessarily identical for the two scenarios.

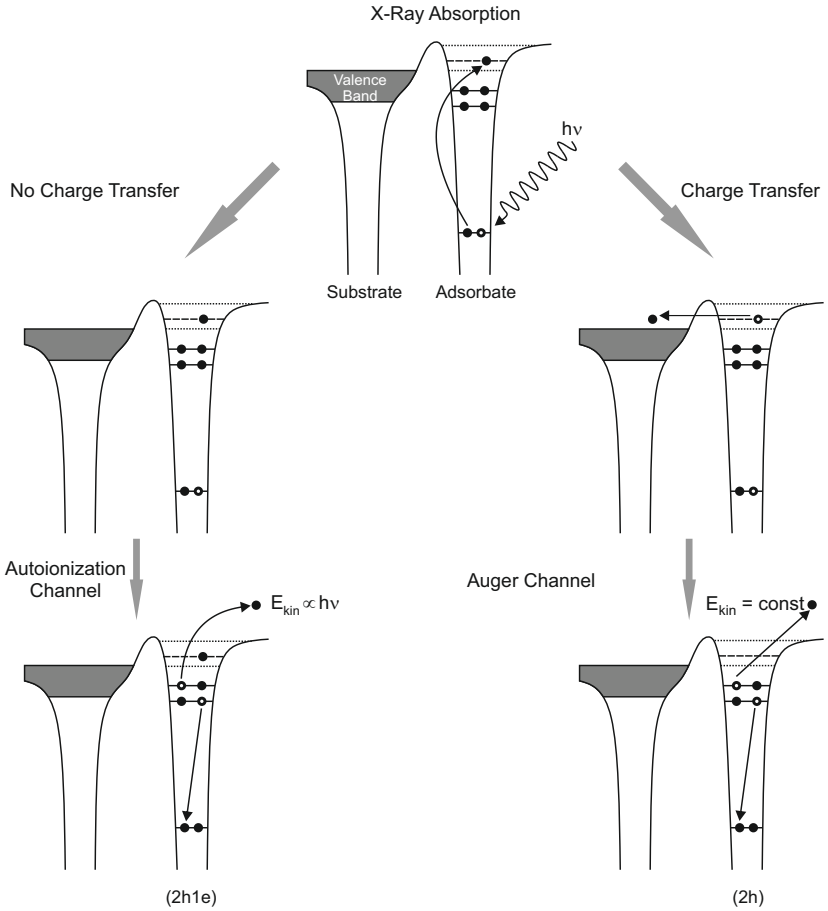

Figure 3.4: Schematic depiction of different de-excitation pathways for a system coupled to a continuum after resonant excitation. Following the left route (no charge transfer), the core hole decays *before* the electron has been transferred to the continuum, resulting in a (2h1e) final state. On the contrary, the route on the right (charge transfer) illustrates the case where the core hole decays *after* the electron has been transferred into the substrate, leaving the system in a (2h) final state. The left route is referred to as autoionization channel, whereas the right is denoted as Auger channel. The participator decay with its (1h) final state (cf. isolated system in fig. 3.3), which belongs to the autoionization decay channel, has been omitted for clarity.

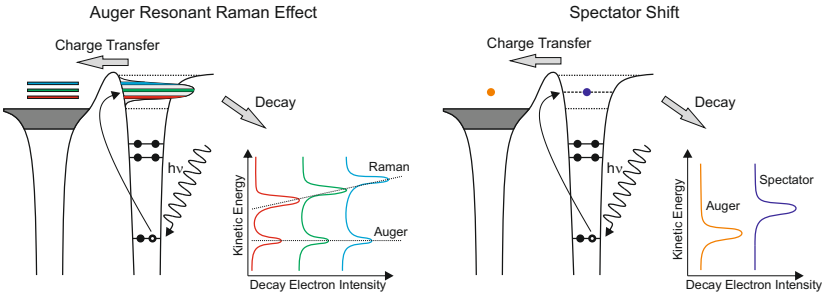

Figure 3.5: The Auger resonant Raman effect (left) illustrates the observed linear dispersion in energy as a function of photon energy for electrons from resonant decay, thus facilitating the separation of autoionization and Auger decay electrons. Similarly, the spectator shift (right), which arises due to additional screening by the electron in the resonance, leads to a separation of Auger and spectator electrons in energy.

1. Auger resonant Raman effect
   As previously described, decay electrons from autoionization decay exhibit a linear dispersion in energy as a function of the photon energy. Scanning the excitation energy over the resonance width will yield decay components *with* dispersion, I_{auto}, and *without* dispersion, hence I_{Auger}, if plotting the spectra versus the kinetic energy.

2. Spectator shift
   If the resonantly excited electron remains localized on the adsorbate during the core hole decay, it will partially screen the positive core hole, which leads to smaller Coulomb interaction between core hole and outgoing decay electrons and consequently to a higher kinetic energy. This so-called spectator shift is strongly dependent on the efficiency of the screening process and can range from several meV to a few eV in kinetic energy.

Since many core holes of interest (Ar[2p], N[1s], F[1s] in this work) decay within a few femtoseconds, the accessible charge transfer times lie in the ultrafast, low femtosecond (10^{-15} s) regime. Nevertheless there are limitations of the core hole clock method:

1. In order to reliably separate autoionization and Auger fractions, the charge transfer time should fulfill the following restriction: $0.1\,\tau_c \leq \tau_{ct} \leq 10\,\tau_c$

2. The resonance energy E_{res}, defined with respect to the Fermi level, has

to be positive, i.e. lie above the Fermi level, to allow charge transfer *from* the adsorbate *to* the substrate.

3. Since the vibrational progression in autoionization and Auger decay channels can be quite different when molecules are investigated [76], the disentangling procedure can become ambiguous.

Taking all that into account, the core hole clock method provides a versatile tool for investigating ultrafast charge transfer dynamics in a spectroscopic manner.

3.4 X-Ray Absorption Spectroscopy

In x-ray absorption spectroscopy (XAS), the energy dependent absorption of photons in matter is investigated. In contrast to XPS, where the occupied density of states (DOS) is probed, XAS provides information on the unoccupied DOS. Since the attenuation of the incident radiation cannot be measured directly in transmission mode for ultrathin overlayers adsorbed on thick solid samples, secondary processes like Auger electron emission have to be exploited.

This makes XAS similar to resonant Auger electron spectroscopy, with the difference that the energetic distribution of the decay electrons is not of interest, only their total amount at a given photon energy. Since the number of decay electrons is proportional to the number of adsorbed photons, they provide a measure of the extend of x-ray absorption.

3.4.1 X-Ray Linear Dichroism

An often used refinement of XAS in surface science is called NEXAFS (near-edge x-ray absorption fine structure) spectroscopy and deals with the fine structure in the absorption cross section close to the ionization threshold of a core level. Figure 3.6 (a) illustrates the x-ray absorption process and the resulting NEXAFS spectrum for diatomic molecules like CO or NO coupled to a substrate. The first transition into the lowest unoccupied molecular orbital (LUMO) results in a sharp peak in the absorption spectrum, which is in this case a π^* orbital. If the electron is excited into a quasi-bound state above the ionization potential (IP), the resonance is called *shape resonance*, which, in a molecular picture, corresponds to the excitation of a core level electron into an antibonding σ^* orbital.

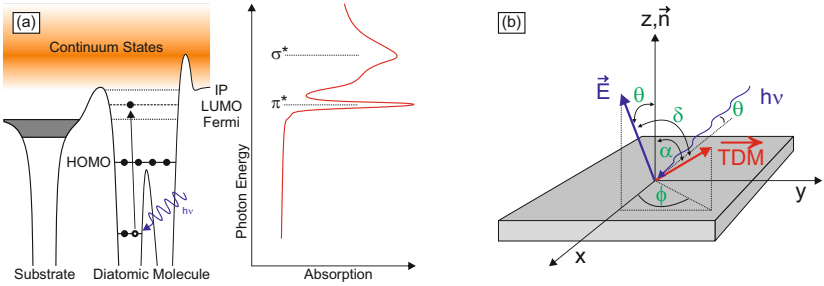

Figure 3.6: (a) Illustration of the x-ray absorption process for a diatomic molecule coupled to a substrate. Excitation of electrons from core levels into unoccupied molecular orbitals (LUMO,LUMO+1,..) leads to characteristic peaks in the absorption cross-section which can be related to π^* and σ^* resonances. **(b)** Depiction of the measurement geometry for a vector type orbital, with $\vec{n}$ denoting the surface normal vector, $\vec{E}$ the vector of the electric field and $\vec{O}$ the transition dipole moment (TDM) vector. The angle between electric field and TDM is labeled δ.

The main reason for the popularity of NEXAFS in surface science is that it provides information on the orientation of molecules adsorbed on surfaces and is inherently element- and site-specific [77]. The capability of delivering geometric information arises due to the fact that the NEXAFS resonances show a strong dependence on the polarization of the exciting radiation. This can be understood from the x-ray absorption cross-section σ_{xas} in the dipole approximation [77]:

$$\begin{aligned}\sigma_{xas} &= \frac{4\pi^2\epsilon^2}{m^2 c\,\omega}\left|\langle f|\vec{e}\cdot\vec{p}|i\rangle\right|^2 \rho_f(E) \\ &\propto \left|\vec{e}\cdot\langle f|\vec{p}|i\rangle\right|^2 \\ &\propto \cos^2(\delta) \end{aligned} \tag{3.7}$$

where $|i\rangle$ and $|f\rangle$ denote the initial and final state orbitals, respectively, $\vec{e}$ is the unit vector in the direction of the electric field and $\vec{p}$ is the sum momentum operator of the involved orbitals. The vector $\langle f|\vec{p}|i\rangle$ is often referred to as the transition dipole moment (TDM), whereas the angle between electric field polarization and TDM is denoted as δ.

In the case that $|i\rangle$ is a s-type core orbital, only transitions into the p-component of $|f\rangle$ are allowed according to the dipole selection rule. Accordingly, the TDM will be directed along the p-like final state orbitals. Since bonds and molecular orbitals (MO) are strongly oriented in molecules, the

TDMs also point in specific directions within the molecule. Therefore, for molecules adsorbed on surfaces, the absorption depends strongly on the orientation of the electric field vector relative to the orientation of the molecule. One can further discriminate between vector-type and plane-type final state orbitals, where the direction of the p-components are described by a vector or by a plane, respectively.

For the vector-type (I_v) and plane-type (I_p) orbitals with the TDM aligned as indicated in Figure 3.6 (b) and the substrate being 3-fold symmetric (e.g. Ni(111)), the polarization dependent absorption intensity can be written as [77]:

$$I_v = cos^2\theta \cos^2\alpha + \frac{1}{2}\sin^2\theta \sin^2\alpha \tag{3.8}$$

$$I_p = 1 - cos^2\theta \cos^2\gamma - \frac{1}{2}\sin^2\theta \sin^2\gamma \tag{3.9}$$

being θ the angle between polarization vector and surface normal and α the angle between TDM and surface normal (in the case of a vector type orbital). For a plane-type orbital, γ is the angle between the normal vector of the orbital plane and the surface normal. In practice, the polarization vector is changed by rotating the sample with respect to the incoming synchrotron radiation (rotation around x-vector in Figure 3.6 (b)). By collecting NEXAFS spectra under 2-3 different angles, the orientation of the molecule can basically be determined with an accuracy of $\pm$ 5 to 10°.

Data Acquisition and Analysis The NEXAFS spectra shown in this work[3] were typically recorded with a homemade partial electron yield (PEY) detector which covers a large solid angle of almost 2π and can be operated in a quantitative way (cf. Section 3.6.4 and Ref. [78]). To achieve the same detection conditions under every angle, sample and detector were rotated simultaneously, keeping the angle between sample and detector fixed (normal emission) Typical retardation potential for suppressing secondary electrons for adsorbates on Ni(111) were -150 V for C1s, -260 V for N1s, -400 V for O1s and -560 V for F1s. In order to compensate for beam fluctuations and contaminations of the beamline optics as well as structures inherent to the clean substrate, a standardized normalization procedure [77] was applied to all shown spectra, unless otherwise stated:

$$\text{processed spectrum} = \frac{\text{adsorbate covered sample - clean sample}}{\text{monochromator transmission}} \tag{3.10}$$

[3] Except those shown in Chapter 4, which were acquired using a standard multiplier-based partial electron detector.

where the monochromator transmission was recorded with a type-calibrated GaAsP-Diode [79]. Afterwards, the spectra were normalized to the range [0..1], where 0 corresponds to the pre-edge region and 1 to the intensity after the main resonance region. By subsequent identification of the main absorption features and comparison of their relative intensities under different polarizations, the adsorbate angles with respect to the surface can be determined according to the formulas given in Equations (3.8) and (3.9). Depending on the energy resolution, definition, nature and complexity of the resonance features, the spectra can be fitted with Gaussian and Voigt lineshapes to facilitate a more accurate determination of adsorption angles.

3.4.2 X-Ray Magnetic Circular Dichroism

X-ray magnetic circular dichroism (XMCD) spectroscopy allows the element-specific investigation of magnetic properties such as spin and orbital momentum of solid samples. The dichroism effect arises due to directional symmetry breaking of magnetic origin, e.g. the spin-alignment in ferromagnets. XMCD has been theoretically predicted in 1975 [80] and experimentally confirmed in 1987 at the iron K-edge [81]. Generally, the magnetic properties of the 3d transition metals Fe, Co and Ni are mainly dominated by their d valence electrons, where the spin magnetic moment due to exchange interaction is given by the difference between the number of spin-up and spin-down electrons [82, 83]. Usually, the magnetic properties of these materials are probed by exciting 2p core electrons from the L_2 and L_3 edges into unoccupied 3d states. Figure 3.7 (a) illustrates this process in a simple one-electron picture and the common two-step description [82, 83].

The use of circularly polarized radiation is crucial for the application of XMCD: Right (σ^+) or left (σ^-) circularly polarized photons transfer their angular momentum of $\hbar$ or $-\hbar$ to the excited photoelectron in the first step. Since the photoelectrons from the 2p levels are spin-orbit split, the angular momentum can be partially transferred to the spin by means of spin-orbit coupling [82]. Furthermore, the spin polarization is opposite for electrons originating from the L_2 and L_3 edges due to their different spin-orbit coupling, which is given by l-s and l+s, respectively. Consequently, the excited photoelectron possesses an effective orbital and spin polarization following the initial excitation step. “Spin-up” and “spin-down” are defined relative to the photon spin or helicity, which is parallel (σ^+) or anti-parallel (σ^-) to the photon propagation direction in the adsorption step.

In the second step, the spin-split valence shell serves as a spin-sensitive detector for the excited photoelectrons due to the different unoccupied density of

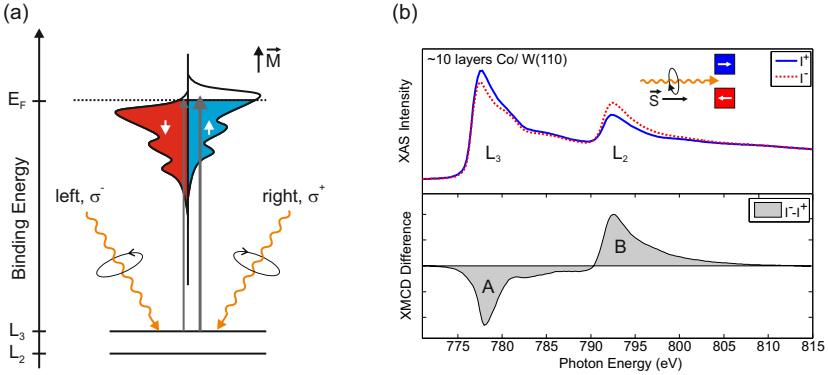

Figure 3.7: (a) Schematic depiction of x-ray absorption with circularly polarized photons at the $L_{2,3}$ edge of a ferromagnet. $\vec{M}$ denotes the sample magnetization and determines the orientation of spins in the metal states. **(b)** Exemplary XMCD spectra of a thin film of Co deposited on W(110). The top panel shows the x-ray absorption profiles for two photon spin/magnetization alignments, the bottom panel shows the difference curve. The directions of magnetization and photon helicity are defined according to Ref. [83].

states for spin-up and spin-down electrons. The same is true, if the d valence shell possesses an orbital momentum, then it also acts as an orbital-sensitive detector. For maximum dichroism, the quantization axis of the "detector", which is the direction of magnetization, and the photon propagation direction need to be aligned parallel. It is worth noting that switching the photon helicity and reversing the magnetization direction gives the same results [82], which can be used for eliminating experimental asymmetries.

Figure 3.7 (b) shows an exemplary XMCD spectrum of a thin, in-plane magnetized Co film grown on W(110). The top panel shows the absorption profiles for parallel (blue) and anti-parallel (red) alignment of photon spin and sample magnetization, whereas the difference spectrum is depicted in the lower panel. As mentioned above, the peaks in the difference spectrum for the L_3 (A) and L_2 (B) edges show a reversed behavior due to opposite spin-orbit coupling. By applying the sum rules derived for XMCD spectroscopy [84,85], it is possible to relate the measured difference intensities A and B to the spin and orbital momentum. Since the main purpose of XMCD in this thesis was the control of the magnetization of the grown layers, it shall not be further detailed here. A comprehensive review about XMCD and its applications be found in, e.g. Refs. [82,83].

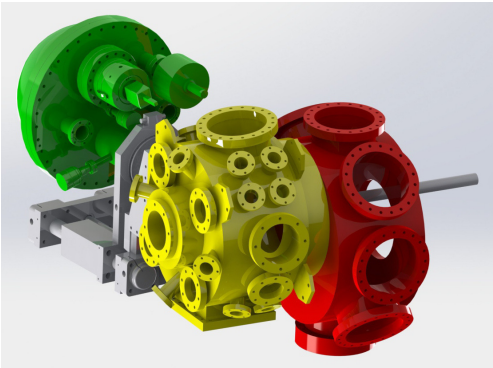

Figure 3.8: Computer drawing of the ultrahigh vacuum system used for experiments within this work. Preparation chamber (red), analysis chamber (yellow) and the hemispherical electron analyzer (green) are depicted. The other parts described in the main text have been omitted for clarity.

3.5 Ultrahigh Vacuum System

Most of the experiments (except the results presented in Chapter 4) were conducted in a home-made ultrahigh vacuum (UHV) system which is depicted in Figure 3.8. Briefly, the system consists of two cylindrically-shaped chambers which are connected and serve as preparation (red) and analysis (yellow) chamber. To ensure a base pressure below 5×10^{-11} mbar, two subsequent turbo pumps (180 l/s) together with a liquid nitrogen cooled titanium-sublimation pump (500 l/s) run during normal operation. A small ion-getter pump (20 l/s) serves as a back-up pump in case of a failure of the turbo pumps. The sample is mounted on a manipulator with a flow-cryostat, which reaches temperatures below 20 K with liquid helium cooling. Electron bombardment heating of the sample enables annealing temperatures above 2000 K, which is sufficient even for cleaning the tungsten crystal. The chamber also comprises a load-lock system that allows a fast sample transfer without breaking the main vacuum. During synchrotron experiments, the chamber is connected with the analysis part separated by a valve to the beamline output, i.e. the radiation is coming from the left side in Figure 3.8.

The preparation chamber is equipped with a ribbon-type metal evaporator for preparing thin films of nickel, iron and cobalt on the W(110) crystal. Therefore, the evaporator resistively heats a thin (50 µm), high-purity metal sheet to ensure a clean film-growth process, which is further controlled in-situ

by a quartz-microbalance acting as a thickness monitor. In order to magnetize the thin films, a ferromagnetic core coil has been constructed, which can be placed above the sample and magnetize it by applying a current pulse of about 50 A, corresponding to a magnetic field of $\sim$ 250 mT, for 1-2 seconds. A gas dosing system is used for adsorbing gases and liquids onto the sample through a small stainless steel tube, which can be controlled by leak valves. Solid substances with a lower vapor pressure were adsorbed by sublimation through a gate valve directly onto the sample. An ion-sputter gun is available for sample cleaning, whereas a standard LEED system is used for checking the surface quality.

During this work, a new Specs Phoibos 100 CCD electron analyzer has been installed in the analysis chamber, which is shown in green in Figure 3.8. For laboratory measurements, the chamber has also been equipped with an Omicron HIS-13 UV lamp with additional polarizer. Furthermore, the analysis chamber comprises a twin anode x-ray tube (Mg/Al) and a custom-built quadrupole mass-spectrometer for high-resolution ion detection [86]. For x-ray absorption measurements, a novel partial electron yield detector was constructed, as detailed in Section 3.6.

One advantage of this UHV system is that sample and detector orientation can be adjusted independently of each other. This is accomplished by a differentially pumped, rotatable analysis chamber and allows, e.g. a constant sample-detector alignment during NEXAFS measurements. For synchrotron measurements, the chamber was transported to the radiation source BESSY II in Berlin and subsequently connected to the beamline outputs.

3.6 A Versatile Partial Electron Yield Detector with Large Acceptance Angle and Well-Defined Threshold Energy and Gain

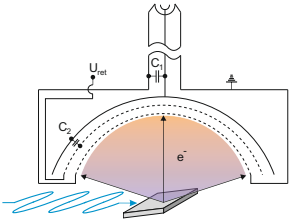

Abstract We describe a partial electron yield detector for x-ray absorption studies with a large angle of acceptance of π sr, a well-defined electron cut-off energy due to a spherical retardation optics, and a linear, well reproducible gain. The detector operates without electron multipliers and is assembled from standard replacement parts of conventional low energy electron diffraction (LEED) optics.

This section was published in Reference [78]. Reproduced with permission.

3.6.1 Introduction

X-ray absorption spectroscopy (XAS) with synchrotron radiation sources is a key technique for investigating the electronic and geometric structure of materials [77]. In the soft x-ray regime, direct XAS measurement by recording the photon energy dependent attenuation of the light is possible only for optically very thin targets, e.g. gas cells or very thin films of condensed matter. For solid samples, secondary processes have to be exploited to get access to the primary absorption step. Suitable probes are fluorescence photons and Auger electrons emitted upon the decay of primary inner-shell vacancies. Particularly for low-Z materials and shallow core holes the non-radiative Auger decay prevails [87]. By selective detection of these decay electrons, the XAS spectra related to the excitation of distinct core orbitals are monitored. Commonly this is accomplished either by a band pass-type electron energy analyzer or by a partial electron yield (PEY) detector acting as a high pass filter. The optimum PEY detector should accept a large solid angle in order to integrate over the angular distribution of the decay electrons. For oriented molecules on surfaces, this distribution can show strong modulations due to contributions from different final states of the core decay [88]. It is a crucial point that recording XAS with a small angle of acceptance can yield ambiguous results because distinct decay channels may be selectively enhanced or suppressed.

The detector should also have a well-defined low energy cut-off with a narrow threshold region; furthermore it should not compromise the signal-to-noise (s/n) ratio of the original signal. In addition, a linear response with reproducible gain is necessary. For surface science applications, compatibility with ultra high vacuum conditions is required. Here we present a straightforward detector design that meets all of the aforementioned requirements. We further demonstrate its performance by a quantitative analysis of the PEY signal obtained from a monolayer CO adsorbed on the Ru(0001) surface.

3.6.2 Experimental Details

Conventional PEY detectors consist of a plane grid assembly acting as a high pass and an electron multiplier for current amplification. In most cases, multichannel plates (MCPs) or channeltrons serve as electron multipliers. Although such setups are used in many XAS experiments, they are accompanied by several drawbacks. First of all, the amplification factor of the electron multipliers is difficult to determine and changes with contamination history and accumulated charge, making a reliable and quantitative interpretation of the primary signal in terms of "electrons per second" difficult and complicating the comparison of experimental and theoretical results. More important, the use of MCPs etc. makes the design of a detector that covers a large solid angle elaborate and expensive. The plane retardation optics that is used in most of such devices introduces severe angular dependent variations of the cut-off threshold. For a solid angle of 1.85 sr corresponding to an opening angle of $\pm 45^\circ$, the deviation of the cut-off energy between center and rim is already 30%.

These drawbacks are overcome with the design of a PEY detector displayed in Figure 3.9, which shows the basic principle of operation.

The setup of the detector is simple; it is based on a modification of a conventional LEED (Low Energy Electron Diffraction) optics. LEED optics consists of 3 or 4 hemispherical grids in front of a hemispherical fluorescent screen. Grids and screen are arranged concentrically, typically covering a solid angle of acceptance of π sr. We modified such a LEED optics in a way that only two grids and the solid screen remained. From the screen serving as an electron collector, the fluorescent coating has been removed and all center holes provided in the original design for the electron gun have been closed. The first grid is grounded to avoid electric fields outside the detector, whereas the second grid provides the retarding potential as in conventional PEY detectors; this (negative) potential defines the low energy cut-off of the high pass

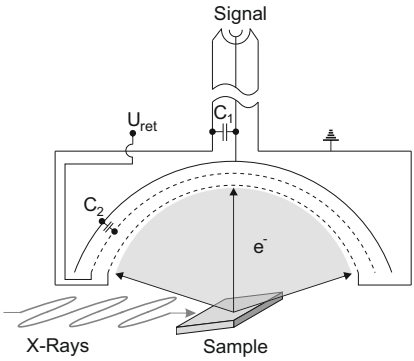

Figure 3.9: Schematic of the PEY detector (see text for details). C_1 and C_2 denote the capacitances between electron collector and ground, and between electron collector and retard grid, respectively.

filter. The electron current onto the collector is amplified outside the vacuum with a standard current amplifier with a well-defined gain (fig. 3.10). With the sample in the center of the spherical grid/screen assembly of a standard LEED optics, the angle of acceptance is π sr, which is large enough to eliminate spurious effects due to the angular distribution of decay electrons. In our experimental setup, the light beam illuminates the sample under grazing conditions (7° with respect to the surface plane). The polarization of the light is changed either by an elliptical undulator, or by rotating sample and detector around the beam in order to avoid mixture of angle- and polarization-dependent effects in the measured signal.

An important issue is to guarantee a satisfactory s/n-ratio of the final PEY signal without the use of an electron multiplier. Electron multipliers introduce some noise due to the stochastic amplification process, but their noise floor at zero input is exceptionally low because of their very small dark currents. This is different for a conventional current amplifier as depicted in Figure 3.10.

Nevertheless, its s/n ratio suffices for nearly all applications. This can be understood by analyzing the different sources contributing to the overall noise current of an amplifier as depicted in Figure 3.10. We base our estimate on a low bias current operational amplifier (OP-Amp OPA 129 [89]) with a feedback resistor of 10^{11} Ohm corresponding to a bandwidth of ∼10 Hz. For larger bandwidths or currents larger than 10^{-10} A, smaller resistors are required. For our measurements shown below, we use the OPA 129 amplifier

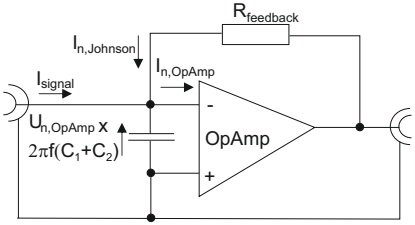

Figure 3.10: Schematic of the current amplifier. Noise sources are labeled with the index "n".

with feedback resistors switchable in decades from 10^8 to 10^{11} Ohm. Note, however, that other amplifiers with similar noise characteristic can be used as well, homemade as well as commercially available devices. Noise sources include the white noise current of the OP-Amp ($1 \times 10^{-16}\mathrm{A}/\sqrt{\mathrm{Hz}}$) (see [89] and Appendix A) and the noise current produced by the noise voltage of the OP-Amp at the detector capacitance $C_1 + C_2$ (fig. 3.9; 70 pF in our case). The noise from this source (average value $2.4 \times 10^{-16}\mathrm{A}/\sqrt{\mathrm{Hz}}$ for f $\leq$ 10 Hz, see Appendix A) is blue, i.e. increases with frequency, because the frequency dependencies of OP-Amp voltage noise [89] and capacitive impedance compensate only partly. For f $\leq$ 10 Hz, the largest contribution is the Johnson noise of the feedback resistor ($4 \times 10^{-16}\mathrm{A}/\sqrt{\mathrm{Hz}}$ @ 300 K); other noise sources can be neglected. For a bandwidth of 10 Hz, corresponding to a dwell time per photon energy channel of $\sim$0.1s, we obtain a total noise current of 1.5 fA. We compare this value to the excitation energy dependent decay electron signal from an adsorbate given by [77]:

$$I(h\nu) = \frac{\Omega}{4\pi} \times J_0 \times \sigma_x(h\nu) \times \rho \times \omega_\alpha \times \frac{1}{\sin\alpha} \times T \times e \qquad (3.11)$$

Where Ω is the detection solid angle, J_0 the intensity of the incoming radiation, $\sigma_x(h\nu)$ the adsorption cross-section at photon energy $h\nu$, ρ the surface density of the adsorbate, ω_α the Auger fraction of the core decays, α the angle of incidence with respect to the surface (7° in our case), T the optical transmission of the two grids (56%) (see Appendix A for details) and e the elementary charge. We assume a dilute monolayer of particles on the surface (10^{14} molecules per cm^2) with a (low) excitation cross section of 1 Mbarn measured with a (low) photon flux of 10^{11} photons/s. With these values we obtain a collector current of 1.8 pA, i.e. a signal three orders of magnitude above the noise floor. With samples of larger cross sections and higher photon flux the s/n ratio would be even better. A noise level of 0.1% of the signal

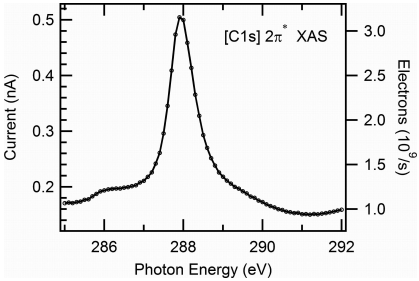

Figure 3.11: XAS from a CO monolayer on Ru(0001) in the $[C1s]2\pi^*$ region measured with a low photon flux of 1.4×10^{11} photons/s. Raw data without further processing are shown (the shape of the background is due to strong modulation of the photon flux at the carbon K-edge caused by contamination on the optical elements of the beamline).

will be sufficient for all NEXAFS experiments; even a value of 1% will be acceptable for most systems.

3.6.3 Results and Discussion

To verify our quantitative approach, the XAS spectrum of the CO/Ru(0001) $[C1s]2\pi^*$ resonance was recorded at the synchrotron radiation source BESSY II. The spectrum presented in Figure 3.11 shows a well-resolved resonance centered around 288 eV and a low background noise resulting in an excellent s/n-ratio above 1000. Figure 3.11 shows the raw data, recorded with a photon step width of 0.1 eV and a dwell time of 1 s per channel (shorter time bins have been avoided due to limiting undulator and monochromator settling speeds). The retarding voltage was set to -95 V. The photon flux (1.4×10^{11} photons per second) was determined with a UHV compatible GaAsP photodiode [79], and the CO density at saturation coverage (1×10^{15} molecules per cm^2) was taken from the literature [90].

We compare our measured data to cross-section measurements of the CO molecule in the gas-phase by electron energy loss spectroscopy [91, 92]. The value for the $[C1s]2\pi^*$ resonance of CO adsorbed on a transition metal surface compared to gas phase data is expected to be smaller because, compared to the isolated molecule, the local $2\pi^*$ density of states at the carbon atom is reduced upon chemisorption [93]. In order to account for different photon energy resolution and different line shapes in the two experiments, we use for both datasets cross section values that have been energy-integrated

over the resonance. We calculate 15.6 Mbarn x eV for our data compared to 16.4 Mbarn x eV for the reference data. Although we obtain a quantitative result that reproduces the expected reduction of the $[C1s]2\pi^*$ excitation cross section by the formation of the chemisorptive bond, we note that our value for the photon flux might still be of limited accuracy due to yield scatter of the photodiode. In further quantitative XAS experiments that will become possible with our detector, individually calibrated photodiodes have to be used. The data shown in Figure 3.11 corresponds to the raw data of the experiment, i.e. no normalization, background subtraction or smoothing has been performed.

As shown above, amplifier noise is a minor problem in our design. Interference of electric pick-up and microphonic effects can be more important and should be carefully minimized. Particularly, the voltage source feeding the retard grid must be absolutely noise free because this grid directly couples to the collector via C_2 (fig. 3.9; see Appendix A). On the other hand, inserting a grounded third grid for decoupling both electrodes would remove the retarding field that keeps secondary electrons from leaving the collector, apart from transmission effects. The connection between the collector and the signal feedthrough should also be mechanically stable and of low capacitance. We use a stiff stainless steel wire inside the mounting tube of the whole assembly, resulting of a C_1 value of 55 pF (fig. 3.9). The amplifier is attached directly to the feedthrough.

3.6.4 Conclusions

In summary, we could demonstrate that our novel partial electron yield detector generates high-quality x-ray absorption spectra with an excellent signal-to-noise ratio. The use of spherical retard optics guarantees a constant cut-off energy for all electron trajectories reaching the detector. The absence of intrinsic electron amplification with channelplates or other multiplier devices is compensated by the large acceptance angle in combination with low-noise current amplification. This simple detector design enables a reliable and quantitative analysis of the measured partial electron signal from adsorbed species on surfaces in the mono- and sub-monolayer range.

Chapter 4

Orbital-Symmetry-Dependent Charge Transfer Through Molecules Assembled on Metal Substrates

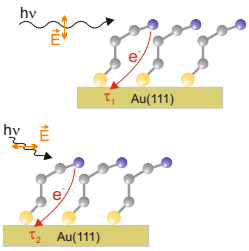

Abstract Femtosecond charge transfer dynamics in self-assembled monolayers of cyano-terminated ethane-thiolate on gold substrates was investigated with the core hole clock method. By exploiting symmetry selection rules rather than energetic selection, electrons from the nitrogen K-shell are state-selectively excited into the two symmetry-split π^* orbitals of the cyano end group with x-ray photons of well-defined polarization. The charge transfer times from these temporarily occupied orbitals to the metal substrate differ significantly. Theoretical calculations show that these two π^* orbitals extend differently onto the alkane backbone and the anchoring sulfur atom, thus causing the observed dependence of the electron transfer dynamics on the symmetry of the orbital.

This chapter was published in Reference [94].

4.1 Introduction

Since the pioneering electron paramagnetic resonance (EPR) experiments of Weissman [95] and Voevodskij et al. [96] on intramolecular charge exchange and the related theoretical interpretation by McConnell [97], charge transport through molecular entities and its microscopic details have attracted continuously increasing interest due to their fundamental importance for many fields and applications. Important examples include: i) electron transfer and redox reactions in chemistry, electrochemistry, and biology [98–100]; ii) materials modification by electronic excitations [101], including irradiation induced tailoring of thin organic films [102] and beam effects in spectroscopy and microscopy [103]; iii) molecular photovoltaics [104, 105]; and iv) the field of molecular electronics [35]. The most direct access to charge transport through molecules is certainly by making contact either to single, or groups of molecules and measuring current vs. voltage (I-V) curves (see Ref. [37] for a review of connection techniques). Extensive theoretical work is available for the interpretation of such I-V results [35, 39]. Further detailed insight is obtained from the analysis of fluctuations of the electrical current and the study of inelastic processes such as current-induced vibrational and conformational excitations [35, 106, 107].

The EPR studies mentioned above, however, belong to a different class of experiments. There, spectroscopic features related to an intrinsic time scale are analyzed. The EPR spectra from an uncompensated electron spin in anions consisting of two aromatic rings connected either by one [96] or two [95] aliphatic chains show hyperfine interaction with either one or both rings, or an intermediate signature, depending on the electron exchange rate as a function of chain length. In these experiments, the limiting time resolution was the inverse frequency of the hyperfine interaction in the 0.1 to 1 µs range [95, 96], i.e. the method is appropriate for slow transfer. For tracking faster processes a shorter time interval reference is required and as such the lifetime of inner shell vacancies [75] proved to be valuable. By this core hole clock method (CHC), the transfer dynamics of an electron resonantly excited from an inner shell is obtained from the ratio of resonant and non-resonant core decay spectra in combination with the known lifetimes of core holes [74, 108]. In most cases, the delocalization time of the resonantly excited core electron into a continuum, e.g. the conduction band of a metallic substrate or another conductor, during the lifetime of the core hole is recorded; the inverse process, i.e. the promotion of an electron from the continuum towards the core ionized atom before core decay, is however possible as well [74]. Despite its limitations due to the "availability" of core levels and resonances with appropriate lifetimes and energies, the CHC method has the advantage

that it represents an atom selective probe of the electron relaxation dynamics [41, 74, 108, 109].

It was used by some of us for investigations of charge transport in thiolate bonded self-assembled monolayers (SAMs) with aliphatic [44, 110] and aromatic, as well as mixed aliphatic/aromatic backbones [45, 111]. We demonstrated that CHC is well suited for the investigation of charge transport dynamics, through the backbones as well as through the anchor of the SAMs, yielding data corroborating and supplementing results from theory and I-V conductance measurements [44, 45, 110, 111]. In addition, we could show that electron transfer from a core-excited N atom in a cyano (CN) substituent group through an adjacent aromatic backbone and into the substrate can depend strongly on the orbital to which the core electron has been primarily promoted. In a CN group attached to an aromatic ring, the π^* degeneracy is lifted, yielding in-plane and out-of-plane [N1s]π^* resonances. By selective excitation of these resonances - their excitation energies differ by 0.95 eV [45] - we found much faster charge transfer for the out-of-plane π^* orbital, which is strongly coupled to the aromatic π system [45], relative to the in-plane orbital, which is not π-coupled. In the present work we show that a similar symmetry dependent effect exists for aliphatic CN-terminated SAMs as well. This is remarkable because for these systems the effect of symmetry breaking is much weaker: The energy separation of the two [N1s]π^* resonances of the CN ligand at 399.6 and 399.7 eV, i.e. 1.1 and 1.2 eV above the Fermi edge, is nearly one order of magnitude smaller than their spectral widths [44, 110] and selective electron transfer into one of the two unoccupied orbitals simply by selecting the correct photon energy is impossible. Instead, by applying an approach developed for CHC experiments on atomic adsorbates [112], we use the well-defined polarization of soft x-ray photons from a synchrotron storage ring for orbital-selective excitation. We believe that at present CHC is the only method enabling such an orbital *and* site selective look on charge transport processes as reported here.

4.2 The Core Hole Clock Method

In Figure 4.1 (a), the schematic of core excitation and de-excitation routes in a molecule coupled to a continuum shows the essential basis for evaluating the decay spectra in the framework of the CHC method. First, a core electron (N1s) is promoted by synchrotron radiation to an unoccupied bound state above the Fermi level. The subsequent decay of the core hole can take place *before* or *after* the transfer of the resonantly excited electron to the substrate continuum. Since the resulting decay spectra differ for decay events

before and *after* delocalization of the charge, measured data containing contributions from both routes can be decomposed into purely resonant (decay before delocalization) and purely non-resonant (decay after delocalization) fractions[1].

In the non-resonant case (route 1), the final state is a 2-hole (2h) state that corresponds to normal Auger decay (A), whereas in the resonant case two possible pathways (routes 2a and 2b) for core decay exist. On the one hand, the electron in the resonance can participate in the decay; then the final state is a 1h state which is labeled participator decay (P). If the electron on the other hand does not participate in the core hole decay, the final state becomes a 2-hole 1-electron (2h1e) state, hence called spectator decay (SP).

To allow for a decomposition of the resonant decay spectrum into resonant and non-resonant contributions, pure resonant and pure non-resonant spectra have to be acquired. The pure non-resonant ($S_{non-resonant}$) spectrum is obtained by excitation above the resonance threshold, corresponding to normal Auger decay, whereas resonant excitation of a similar system where charge transfer does not take place yields a pure resonant spectrum ($S_{resonant}$). Reproducing the experimentally obtained resonant decay spectrum by a linear combination of $S_{resonant}$ and $S_{non-resonant}$ allows the calculation of the charge transfer time according to the core-hole clock framework using the expression: $\tau_{CT} = \tau_{core}\,(I_{resonant}/I_{non-resonant})$ [74], where τ_{core} is the core-hole lifetime and the I-terms are the respective weights of the linear combination.

4.3 Experimental Methods

We performed our experiment with thiolate-bonded Au-S-$(CH_2)_2$-CN and Au-S-$(CH_2)_{16}$-CN SAMs, abbreviated as C2CN and C16CN. They have been prepared by a standard immersion procedure [17] on Au(111) substrates (with randomly oriented domains) evaporated (100 nm) on Si(111) wafers primed with a thin (5 nm) Ti layer to improve adhesion[2]. Experiments were performed at the HESGM beamline of the synchrotron radiation facility BESSY II, Berlin. For nearly noise free decay electron spectra the energy resolution of this dipole beamline was set to a medium value of ≈ 0.4 eV at the N1s

[1] It should be noted that we used the terms *resonant* and *non-resonant* throughout this publication instead of *autoionization* and *Auger*, respectively, as introduced in Section 3.3.

[2] The sample preparation was performed by the group of M. Zharnikov, University of Heidelberg.

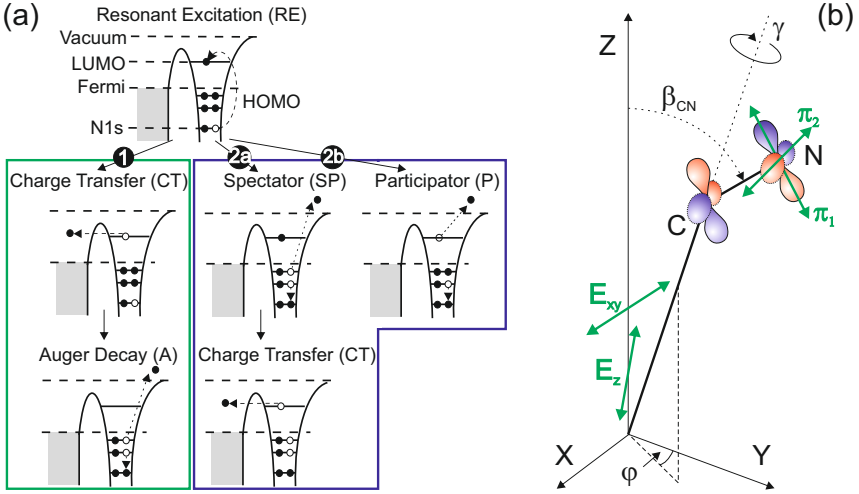

Figure 4.1: (a) Schematic of core excitation and de-excitation pathways for a molecule coupled to a continuum. Following resonant excitation, non-resonant (1) and resonant (2a,2b) pathways exist for the de-excitation, resulting in distinguishable decay electron spectra. **(b)** Measurement geometry and relevant angles of the molecule on the surface.

edge. X-ray absorption spectra (XAS) were acquired with a standard partial electron yield detector; x-ray photoelectron (XPS) as well as decay electron spectra with a hemispherical electron energy analyzer (Scienta R3000). Sample temperatures were always 300 K. The cleanliness of the samples was checked by XPS. C1s, N1s and S2p binding energies agreed well with previous measurements [44,110]. XAS results complied with results of previous studies from which tilt angles of the C-N axis with respect to the surface normal of 65° and 60° were obtained for C16CN [113] and C2CN [44], respectively (see Figure 4.1 (b) for experimental geometry).

For the ideal geometry of the C2CN moiety (i.e. at low temperature and without further intermolecular interactions), the orbitals representing the π^* resonances can be labeled according to their orientation with respect to the plane defined by the aliphatic planar C-C-C conformation structure. Their nodal planes are either perpendicular ([N1s]π_1^* at 399.6 eV) or parallel to this plane ([N1s]π_2^* at 399.7 eV). For SAMs, the aliphatic backbones (and the terminal groups, see above) are commonly tilted with respect to the surface normal (see, e.g. Refs. [15, 17]). In addition, twisting around the molecular axes of the tilted molecules is possible [15]. XAS and decay electron spectra were recorded for two different polarizations of the light, A_z and A_{xy}. In A_{xy} polarization (normal incidence), the E-vector of the radiation was oriented perpendicular to the surface normal (see fig. 4.1 (b)). Taking the random orientation of domains into account by averaging azimuthally around the surface normal and correcting for the tilt angle of 60° and the small cross section differences due to slightly different resonance energies, but assuming zero twist angle, we expect for this polarization an excitation ratio of 4.3 to 1 for [N1s]π_2^* compared to [N1s]π_1^* for C2CN (see Appendix B for details). The A_z polarization experiments were carried out with a grazing incidence photon beam to give an E-vector tilted by 10° with respect to the surface normal (see fig. 4.1 (b)) so the excitation of [N1s]π_1^* should be favored by a factor of 49.

A non-zero twist angle would reduce this contrast because then the C-C-C planar symmetry is broken thereby reducing the difference between [N1s]π_1^* and [N1s]π_2^* contributions in the XAS signals. For a 60° tilt and a 30° twist we expect [N1s]π_1^* and [N1s]π_2^* intensity ratios of 2.3/1 and 1/1.9 for A_z and A_{xy} light, respectively. Since the exact average and distribution of the molecular twist angles is not known it is problematic to make accurate predictions at present.

4.4 Results and Discussion

NEXAFS spectra of the [N1s]$\pi^*_{1,2}$ absorption edge of the C2CN sample with A_z and A_{xy} polarization are shown in Figure 4.2 (a). The spectra show a small shift of the two absorption maxima (399.6 eV and 399.7 eV) of about 0.1 eV depending on the polarization, whereas the difference spectrum confirms the above mentioned orientation of the C-N group with respect to the substrate. According to their energetic positions, the two absorption maxima are assigned to excitation into the [N1s]π^*_1 (LUMO) and [N1s]π^*_2 (LUMO+1) orbitals.

4.4.1 Determination of the Charge Transfer Times

Figure 4.2 (b) shows the decay electron spectra used for the CHC analysis. For the two polarizations, measured decay spectra of C2CN for π-resonant excitation were reproduced by linear combinations of pure resonant and pure non-resonant line shapes, both normalized to unit area. Contributions from direct photoemission have been subtracted. We obtained pure resonant spectra from resonantly excited C16CN samples with 16 methylene spacer units. Since the charge transfer times in alkanethiols increase exponentially with increasing chain length [110], no charge delocalization is expected within the investigated timescale for chains with more than 4 methylene units. Furthermore, for long chains like C16CN, the resonance energy shifts below the Fermi energy, thus making charge transfer from the cyano group to the substrate energetically forbidden [44]. The non-resonant spectra recorded 5 eV above the resonance show maxima around 360 eV (A2) and 377 eV (A1) (see fig. 4.2 (b)). These belong to two-hole final states with both holes in outer, and holes in inner and outer orbitals, respectively. In the resonant spectra, these maxima (SP1, SP2) correspond to spectator states that are blueshifted by ≈ 8 eV. This large spectator shift eases the decomposition of the measured spectra and makes the CN group a favorite choice for CHC studies. The third maximum at highest kinetic energy (393 eV) (P1) has been assigned to a participator decay process [44, 110]. These participator lines correspond energetically to photoemission final states, although often with different vibrational progressions due to the evolution of the conformation during the lifetime of the core hole [74]. Inspecting the traces of Figure 4.2 (b), it is evident that the non-resonant fraction (green trace) that indicates charge transfer to the substrate before core hole decay is larger for A_z (nearly exclusively [N1s]π^*_1) than for A_{xy} ([N1s]π^*_2 dominates).

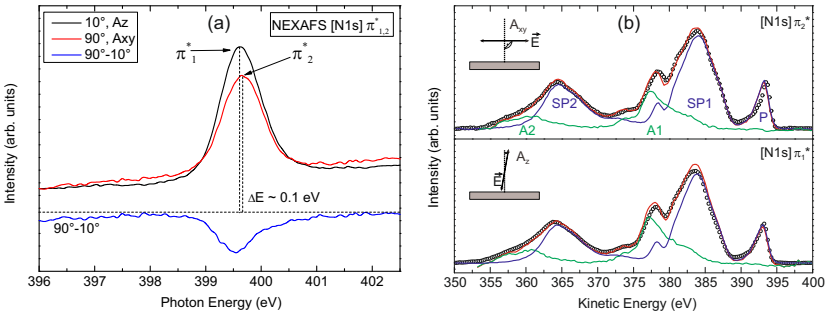

Figure 4.2: (a) NEXAFS spectra of C2CN measured at the N1s absorption edge with two different polarizations. **(b)** CHC evaluation of data sets for A_{xy} (top) and A_z (bottom) light. The experimental decay spectra obtained from C2CN samples at resonance (black points) are reproduced by a linear combination (red line) of the non-resonant line shape recorded for C2CN above resonance (green line), and a purely resonant decay spectrum from C16CN (blue line). Photoemission contributions from the Au substrate and the organic layer have been determined by measurements in the pre-edge range and subtracted.

From the ratios of resonant and non-resonant intensities ($\frac{I_{resonant}}{I_{non-resonant}}$) of 2.58 ± 0.15 for [N1s]π_1^* and 3.28 ± 0.15 for [N1s]π_2^* and the lifetime τ_{core} of the N1s core hole of 6.4 fs [114], we obtain averaged charge transfer times of two independent data-sets of 16.5 fs and 21.0 fs. These turn into i) 15.9 fs for [N1s]π_1^* and 22.2 fs for [N1s]π_2^* after applying the above mentioned excitation energy and tilt angle correction, and into ii) 11.7 fs and 26 fs after considering in addition a twist angle of 30° (see Appendix B for details). We note that correction i) is well justified by experimental and theoretical results (see below). The twist angle of the SAMs, on the other hand, is not known. The estimate for correction ii) shows, however, that such a possible geometry effect would increase the observed contrast, but not cause any decrease.

It is remarkable that the transfer of the resonantly excited electron is faster for the [N1s]π_1^* state despite its by 0.1 eV smaller resonance energy. We also note the good reproducibility of the CHC results for this material; measurements from different preparations and at 3 different experimental stations yielded values for the charge transfer time between 14 fs and 16.5 fs for A_z polarization [44, 110]. We further note that the total error of ±4 fs in Refs. [44, 110] is mainly governed by the uncertainty of τ_{core} which does not enter the comparison made here, whereas the error of determining the ratio

$I_{resonant}/I_{non-resonant}$ is due to the fitting procedure and is estimated to be ± 0.15, which contributes with ± 1 fs to the total error of the charge transfer times.

4.4.2 Theoretical Calculations

To elucidate the electron transfer mechanism and the origin of the different electron injection times, we have simulated the electron transfer (ET) process using a protocol that combines electronic structure calculations at the density functional theory (DFT) level with quantum dynamics simulations (see Refs. [115–117] for details)[3]. The ET dynamics simulation is performed using a diabatic representation where the (quasi)diabatic basis is constructed using charge localized electronic states relevant for the process. For the particular case discussed in this work, these states are the donor state, $|\psi_d\rangle$, that corresponds (in the vanishing coupling limit) to the product of an excited state localized in the photo-absorbing tailgroup and an empty band of the metal surface and a quasi-continuum set of acceptor states, $|\psi_a\rangle$, corresponding (in the zero coupling limit) to the product of the ground state of the cation of the donor and a band state of the metal that gets populated as a consequence of the ET. In this basis, the Hamiltonian for the electronic dynamics takes the form

$$\hat{H} = |\psi_d\rangle\, E_d\, \langle\psi_d| + \sum_a |\psi_a\rangle\, E_a\, \langle\psi_a| + \sum_a (|\psi_d\rangle\, V_{da}\, \langle\psi_a| + \\ + |\psi_a\rangle\, V_{ad}\, \langle\psi_d|), \tag{4.1}$$

where E_d and E_a, the diagonal elements of the diabatic potential matrix, are the energies of the donor and acceptor states involved in the ET process, respectively, and the off-diagonal elements, V_{ad}, are the donor–acceptor ET coupling terms. The parameters used in the ET Hamiltonian (the donor and acceptor energies and the coupling terms, see eq. (4.1)) have been obtained using a partitioning method. The Hamiltonian and the molecular orbitals needed in the partitioning technique have been calculated using a mean-field single electron approach based on DFT methods for a cluster model of the extended system. To this end, in the first step of the procedure we have determined the adsorption geometry of the organic molecule at the Au surface in the low coverage limit using periodic calculations. It was found that the most stable geometry is fcc-bridge like with the C-N axis tilted 70.7° with respect to the surface normal (see Figure 4.3), in reasonable agreement with

[3] The theoretical calculations were performed by M.Thoss and P.B. Coto, University of Erlangen-Nürnberg, together with their collaborators.

the experimental value. We note that for this geometry the twist angle would be zero. In the second step, we have determined the donor and acceptor states and the donor-acceptor couplings using a cluster model obtained from the periodic calculations. These parameters have subsequently been employed for the simulation of the electron injection dynamics process using eq. (4.1). In all calculations, the polarizing effect of the N1s core hole has not been taken into account. This may affect the energetics and extension of the orbitals and can cause quantitative discrepancies with the experimental injection times. However, it is expected that the π_1^* and π_2^* resonances are influenced in a similar way by the core hole and, therefore, the qualitative difference in the mechanism underlying the charge transfer process from the π_1^*, π_2^* donor orbitals should not be altered by including the core hole.

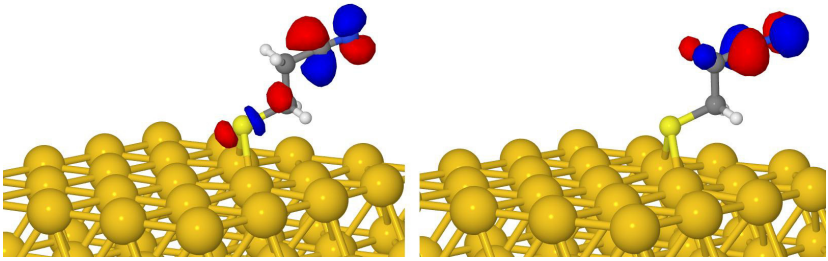

Figure 4.3: Orbitals representing the π_1^* (left) and π_2^* (right) donor states.

Figure 4.3 shows orbitals representing the π_1^* and π_2^* donor states. The π_1^* state exhibits contributions not only at the nitrile group, but also on the aliphatic backbone as well as at the sulfur atom of the thiolate bond. The π_2^* state, on the other hand, is localized at the nitrile group and the hydrogen atoms of the upper methylene group of the backbone, i.e. it has negligible density at atoms close to the substrate. The significant contribution at the aliphatic bridge causes a stronger donor-acceptor coupling for the π_1^* state, which results in the different electron transfer times of the two donor states. The simulation of the electron injection dynamics reveals electron transfer times of 3.8 fs for the π_1^* state and 46.8 fs for the π_2^* state, giving a factor of $\approx$12 increase in the rate due to orbital overlap. These results reproduce the experimentally observed trend within the limitations of the model used. In particular, the model neither takes into account the possible existence of defects in the Au surface, which may modify the type of binding of the organic molecule, nor includes temperature related effects. Thermal excitation can cause, for example, a non-negligible population of non-planar C-C-C con-

figurations, which may influence the electron transfer dynamics through the C-C-C unit. This would, in the limit of an average rotation twist of the CN group, completely break the symmetry of the overlap geometry and give a single value of the lifetime, which is not observed.

4.5 Conclusions

In summary, we have demonstrated by applying the CHC method that charge transport in organic layers can depend on the initially excited resonance state even in cases where the energy separation of the respective states is much smaller than their width and selective excitation is only possible by exploiting symmetry. Calculations explain this effect by the different shape of the orbitals representing the resonance states, in particular their extensions onto the backbone and headgroup. We believe that this technique is applicable to a large variety of systems with negligible energy splitting, e.g. functional groups attached to alkane chains. Because the activation energy for gauche defects is low in alkanes (less than 4 kJ/mole [118]), we expect even larger contrast at sample temperatures lower than 300 K for which the perfect anti-periplanar configuration is more likely.

Chapter 5

Self-Assembled Monolayers on Ni(111)

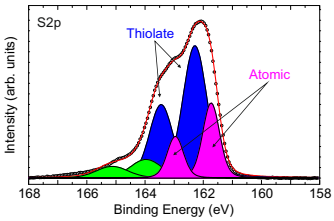

Abstract Self-assembled monolayers of 4-fluorothiophenol and 3- and 4-fluorobenzoic acids on Ni(111) adsorbed under UHV conditions are studied in this chapter. The influence of the different headgroups, which are used to couple the molecules to the surface, is investigated with respect to adsorption geometry, thermal stability and charge transfer dynamics. Depending on the headgroup, significant differences are found concerning the thermal stability of the molecules. Whereas the thiolate-coupled molecules decompose at low temperatures, the carboxylate-coupled monolayers survive annealing above room temperature without dissociation. Furthermore, resonant excitation of the F1s resonance is shown to result in an ultrafast dissociation process which leads to the desorption of atomic fluorine. Investigations on the tailgroup-to-substrate charge transfer yield that all systems exhibit fast electron transfer in the low femtosecond regime, with a more efficient coupling of the thiolate-anchored groups.

5.1 Introduction

Self-assembled monolayers on ferromagnetic substrates constitute an ideal playground for investigating the properties of molecules coupled to magnetic substrates and have potential application in the field of molecular spintronics, as already discussed in Section 2.1.3. Furthermore, corrosion protection is required if nickel is used as a contact material in electronic devices, which can also be facilitated by SAMs [119]. Nevertheless, the number of studies on self-assembled monolayers on nickel surfaces is limited [120–128] and some conflicting evidence regarding the thermal stability of the SAMs is present, that has not yet been resolved (see Section 5.2.2). The low number of studies might be due to the difficulties that arise when preparing SAMs on reactive substrates, such as nickel. One main experimental challenge is the presence of a native oxide of Ni, that hinders the direct adsorption of SAMs from solution and requires a complicated electrochemical pretreatment [121, 128] or the adsorption under UHV conditions [129–132].

The self-assembled monolayers presented in this chapter are therefore prepared under well-defined ultrahigh vacuum conditions on a freshly cleaned Ni(111) single crystal sample. Nickel was chosen as a substrate due to the following reasons:

- Ferromagnetic nature of Ni, with regard to potential spin-dependent measurements
- Reasonably easy preparation methods for obtaining clean surfaces under UHV, in comparison to iron and cobalt [133]
- High surface quality compared to polycrystalline samples
- Among the ferromagnetic substrates, most of the literature involving SAMs considers nickel

The explored SAMs on Ni(111) consist of aromatic precursor molecules, which all have a single phenyl ring as a backbone unit in common. Thiol as well as carboxylic acid headgroups are used to attach the molecule to the surface, whereas a fluorine substituent acts as a tailgroup and therefore determines the interfacial properties of the system. Figure 5.1 shows the investigated molecules consisting of the aforementioned functional units. The molecular properties as well as the protocols for the deposition concerning the various precursor molecules are summarized in Table 5.1.

In the following sections, the differences and similarities of the self-assembled monolayers formed from the presented precursor molecules will be investigated in terms of surface coverage, adsorption geometry, thermal stability

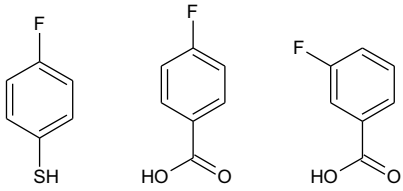

Figure 5.1: Sketches of the precursor molecules used for preparing the self-assembled monolayers on Ni(111) in this thesis. All molecules have a single phenyl ring as a backbone unit in common and are endowed with different headgroup/tailgroup combinations.

Table 5.1: Physical properties, deposition methods and supplier information for the precursor molecules depicted in Figure 5.1. Depending on the vapor pressure of the substances, dosage through a *leak* or a *gate* valve was used for deposition. SA* = Sigma-Aldrich (Supplier)

Abbrev.	Full Name	Phase	Deposition	Suppl.	Purity
4-FTP	4-Fluorothiophenol	liquid	Leak Valve	SA*	98%
4-FBA	4-Fluorobenzoic Acid	solid	Gate Valve	SA*	99%
3-FBA	3-Fluorobenzoic Acid	solid	Gate Valve	SA*	97%

and charge transfer dynamics on the single crystal Ni(111) surface. At the end of the chapter, these results are summarized and some general conclusions, regarding the influence of head- and tailgroup on the aforementioned properties, are drawn.

First, the thiolate-bonded monolayers will be discussed, beginning with the most comprehensively studied molecule, 4-FTP.

5.2 4-Fluorothiophenol SAMs on Ni(111)

Coupling molecules via a thiol linker to the nickel surface in order to obtain self-assembled monolayers is motivated by the large success using the same linker group on gold, silver and copper (see Section 2.1). Nevertheless, even the increased reactivity of *copper* compared to *gold* leads to a variety of new effects, where one of the most apparent is the decreased thermal stability of the self-assembled monolayers [134, 135]. Mainly due to the increased Cu-S bond strength, the molecules become more susceptible for S-C bond

cleavage [134, 135], which results in an ill-defined SAM. Studies of the adsorption of benzenethiol performed on Ni(100) [129, 136, 137], Ni(110) [130] and Ni(111) [131, 137] have shown that the molecules undergo S-H bond scission at low temperatures around 100 K, thus also forming a phenyl thiolate as the primary surface species. However, annealing the high-coverage phase to temperatures above 200 K resulted in cleavage of the S-C bond and the subsequent formation of atomic sulfur [129–131]. The dissociation of the molecules and the presence of atomic sulfur on nickel is in contrast to the behavior of benzenethiol on gold, were intact molecules form well-ordered SAMs at room temperature [138, 139]. This illustrates the increased reactivity of nickel, compared to the reasonably inert gold substrate, and the arising consequences.

Prior work has shown that substitution of benzenethiol with the highly electronegative fluorine can be used to control the work function of the substrate, which already has applications in molecular electronics [27–30, 140]. Furthermore, the fluorine tailgroup serves as a spectroscopic marker, which can be used for obtaining additional data on the orientation from x-ray absorption spectroscopy [141]. The self-assembly of 4-FTP monolayers has been studied on gold [142, 143] and copper [140, 144], where the molecules formed well-ordered monolayers of intact molecules at room temperature. Wang et al. also studied the interfacial charge transfer from 4-FTP adsorbed on Au(111) by resonant photemission spectroscopy [41, 142]. They found that the transfer between resonantly excited C1s electrons and the gold substrate strongly depends on the molecular orientation and the hybridization of phenyl ring orbitals with substrate states [41, 142]. Substituting a hydrogen with a fluorine atom in the para position of the phenyl ring might also be used here to unambiguously define the starting point for the charge transfer process.

In this section, fluorine-substituted benzenethiol (4-FTP) adsorption on Ni(111) will be investigated with focusing on the electronic structure and adsorbate geometry as well as on the thermal stability and charge transfer dynamics.

5.2.1 Electronic Structure and Adsorbate Geometry

Multilayer To begin with, a multilayer of 4-FTP was deposited on the cold substrate ($T_s = 80\,\mathrm{K}$) to check the integrity of the molecules and facilitate the identification of spectral features in XPS and NEXAFS for the more complex, chemisorbed monolayer, which is expected to show effects of the interaction with the substrate.

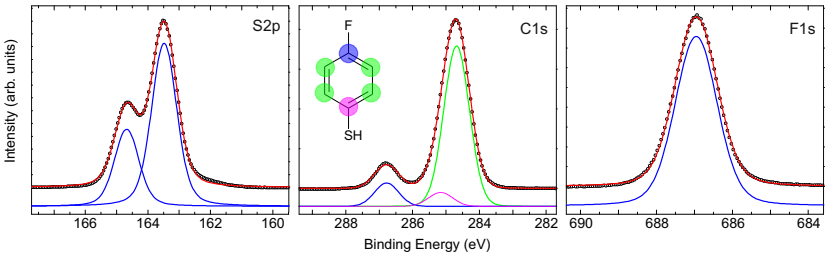

Figure 5.2: X-ray photoelectron spectra of the sulfur (S2p), carbon (C1s) and fluorine (F1s) core levels from a multilayer of 4-FTP on Ni(111). The solid lines are fits to the experimental data (circles). For the C1s spectrum, the decomposition into three peaks identifies the inequivalent carbon atoms of the phenyl ring, as depicted in the inset.

Figure 5.2 shows the S2p, C1s and F1s core level photoemission spectra of the adsorbed multilayer together with the respective curve fits. The S2p spectrum exhibits the expected spin-orbit split doublet with individual components at 163.5 eV ($p_{3/2}$) and 164.7 eV ($p_{1/2}$). In the following, only the peak position of the $2p_{3/2}$ level will be given for simplicity. Since the S2p XPS spectrum shows only one doublet, it is inferred that all molecules are in an identical chemical state that belongs, according to the binding energy [131, 145], to the free thiol, i.e. with the hydrogen atom still attached to the sulfur. In the C1s spectrum, three distinct components at 286.8 eV, 285.2 eV, and the most apparent at 284.7 eV are visible, which all correspond to emission from carbon in the phenyl ring [143]. The main emission peak at 284.7 eV belongs to the equivalent, aromatic C-C bonded carbon atoms of the phenyl ring. Since one carbon is also bonded to the highly electronegative fluorine atom, it shows a large chemical shift of 2.1 eV to higher binding energy and can therefore be easily identified as the peak at 286.8 eV. The sulfur atom attached to one carbon has a similar effect, but smaller in magnitude and can only be extracted after curve fitting, resulting in the emission at 285.2 eV. It should be noted, that the peak areas in the C1s spectrum slightly deviate from the expected ratio of 4:1:1 due to attenuation and photoelectron diffraction effects (see Section 5.2.1). The F1s spectrum is comparably simpler and shows only a single peak at 687.0 eV, as expected for the intact molecule. Furthermore, all peaks in the multilayer are relatively broad, due to the random interaction among physisorbed molecules in the condensed layer.

The corresponding NEXAFS spectra of the multilayer are shown in Figure 5.3. The most intense structures in the carbon spectrum are within the π^* region, which is shown in more detail in the inset of Figure 5.3. According to previous

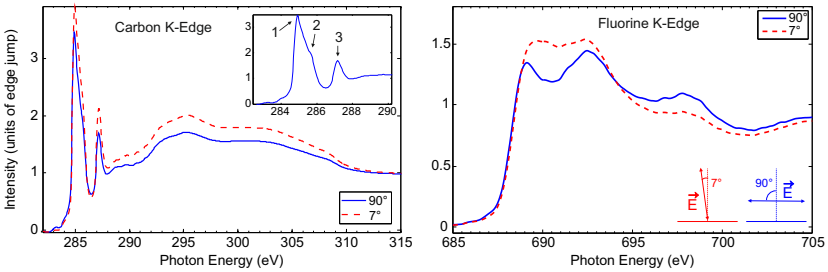

Figure 5.3: NEXAFS spectra of 4-FTP multilayer at the carbon (left) and fluorine (right) K-edge. The inset in the carbon spectrum shows a zoom-in in the relevant π-region, together with peak labeling. The angle θ of the electric field vector $\vec{E}$ is measured relative to the surface normal and varied between 90° and 7°.

literature [140, 142], the strongest feature (1) at 285.0 eV belongs to excitations from the aromatic carbon backbone of the molecule into the lowest π^* orbital, hence the LUMO. An additional shoulder (2) appears at a slightly higher excitation energy of 285.5 eV and can be assigned to contributions from carbon attached to the thiol group [140, 142]. A more distinct resonance (3) appears at even higher photon energy of 287.3 eV and belongs to the fluorinated carbon of the phenyl ring [140, 142]. Since the energy difference of the aforementioned resonances fits the chemical shifts of the corresponding species in XPS, mainly an initial state effect accounts for the three separate resonances. At excitations energies above 290 eV, overlapping σ^* and π^* resonances corresponding to excitations into higher unoccupied orbitals are responsible for the rather broad and smeared structure. Since the carbon (and fluorine) NEXAFS spectra show almost no dichroism, most likely the molecules do not have a strong preferential ordering within the multilayer.

The F1s NEXAFS spectrum is more difficult to analyze since it generally comprises several overlapping σ^* and π^* resonances, as it has been previously shown for adsorbed fluorinated aromatic molecules on gold [146] and fluorinated benzene in the gas phase [147,148]. Similar to the C1s data, the fluorine NEXAFS spectrum in Figure 5.3 shows almost no polarization dependence, thus supporting the assumed random orientation of the molecules in the multilayer. Due to the aforementioned overlapping resonances and the missing dichroism, a deconvolution of the fluorine x-ray absorption spectrum into the corresponding resonances is not feasible for the multilayer spectrum, but will be presented for the corresponding monolayer data below.

Since the goal of this study is to investigate the monolayer 4-FTP/Ni, a temperature programmed desorption (TPD) approach was used to obtain a monolayer from the condensed multilayer [149]. The corresponding TPD spectrum in Figure 5.4 shows the signal of the quadrupole mass spectrometer at mass/charge = 128, which corresponds to the intact molecule, as a function of the sample temperature. A number of features are visible, but here the main focus is on the desorption peak at 188 K, which represents the most intense signature in the spectrum. This temperature corresponds to molecules desorbing from the multilayer, thus leaving behind the monolayer above 200 K, in good agreement with the desorption temperature of 199 K for condensed benzenethiol on Ni(111) [131]. The smaller features around the main peak are most likely due to phase transitions within the layer, which can lead to a further desorption of molecules, but shall not be further investigated. According to this analysis, a monolayer can be prepared by annealing the multilayer to 200 K with a heating rate of 2 K/s, which shall be the starting point for the further analysis.

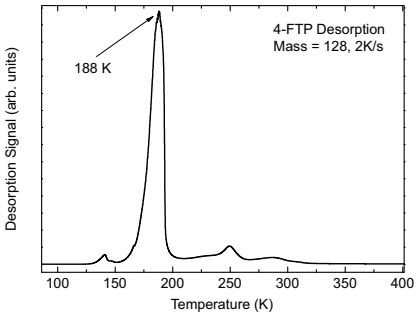

Figure 5.4: Temperature programmed desorption profile obtained for the 4-FTP multilayer on Ni(111). The main desorption peak at 188 K can be assigned to desorption of the multilayer, the other features are most likely due to further phase transitions and reordering processes within the adsorbed layer.

Saturated Monolayer Figure 5.5 shows the XPS spectra of the monolayer 4-FTP/Ni, prepared by desorbing the multilayer as discussed above. The most apparent change is visible in the S2p spectrum, where the dominant doublet is now located at 162.2 eV binding energy, which corresponds to a shift of 1.3 eV to lower binding energy compared to the molecules in the multilayer. This energy of S2p is typical for a thiolate bond with the Ni(111) surface [131, 132, 150] and indicates the attachment of the molecules with the

thiol headgroup to the substrate. The formation of a thiolate bond occurs upon cleavage of the S-H bond with subsequent formation of the metal-sulfur bond. Analyzing the fitted intensities shows that more than 80% of the molecules are in this particular chemical state.

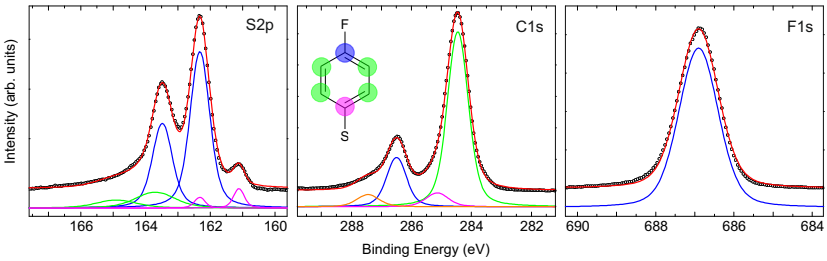

Figure 5.5: XPS spectra of the S2p, C1s and F1s core levels of the 4-FTP monolayer. The S2p spectrum shows mainly thiolate-bonded sulfur (blue solid line), whereas the little amount of atomic sulfur (pink solid line) is a consequence of S-C bond cleavage. The inset in the C1s spectrum shows the origin of the C1s emission peaks within the molecule.

The small peak at lower binding energy of 161.1 eV (pink curve) can be assigned to atomic sulfur on the nickel surface [131, 151], which results from S-C bond scission. This process is competing with the formation of thiolate bonds and is strongly temperature dependent, as it will be further detailed in Section 5.2.2. At 200 K however, the amount of atomic sulfur is only about 5% and can therefore be neglected in the further discussion. It is worth noting that even for thiolate-bonded SAMs on gold, some atomic sulfur is occasionally present on the surface [152–154]. Another byproduct can be identified at a higher binding energy of 163.7 eV (green curve), which is most likely due to either the formation of disulfide species [145] or to some remaining physisorbed fluorothiophenol molecules still trapped following desorption of the multilayer.

In the C1s spectrum the main peak is now located at 284.5 eV, which still belongs to the phenyl ring carbon and is typical for aromatic carbon not directly in contact with the surface [77]. The apparent intensity of the C-S carbon emission is decreased compared to the multilayer, a fact that can be presumably explained by attenuation of the photoelectrons that have to penetrate the self-assembled monolayer before reaching the detector [155,156]. Another new component is visible at the highest binding energy of 287.4 eV, which might originate from a shake-up process, but could not be identified unambiguously. The F1s emission remains unchanged, indicating no distinct

change in the chemical environment of the fluorine atom with respect to the multilayer, and therefore negligible interaction with the nickel substrate. Summarizing the XPS results, the majority of the molecules is bonded to the surface via a thiolate bond, with the phenyl ring and the fluorine tilted away from the surface.

To further elucidate the adsorption geometry of the monolayer, NEXAFS spectra have been acquired, which are reported in Figure 5.6. The carbon K-edge spectrum closely resembles that of the multilayer (Figure 5.3), with the difference, that now a distinct polarization dependence is visible. Since the spectral features for multi- and monolayer are very similar, no apparent change in the electronic structure of the carbon has occurred, as was already concluded by XPS. Analyzing the peak ratios for the C-C, C-S and C-F π^*-resonances for the different polarizations according to Equation (3.8) yields an adsorption angle of the molecules of $30 \pm 10°$ with respect to the surface normal, i.e. the molecules are standing largely upright on the surface, exposing the fluorine tailgroup. The small dip in the carbon spectra at 283.5 eV is due to contaminations on the beamline optics [77] and could not be removed by the normalization procedure as described in Section 3.4, however it does not influence the quantitative analysis for extraction of the adsorption angle.

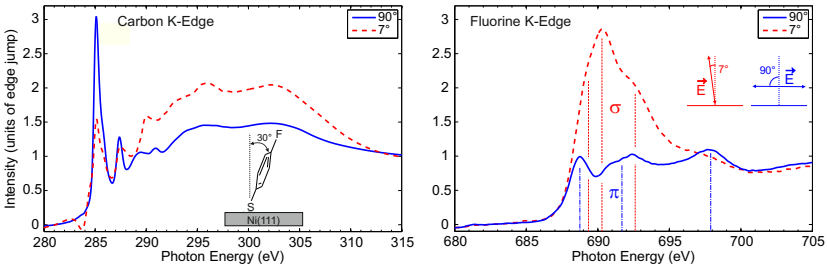

Figure 5.6: C1s (left) and F1s (right) NEXAFS spectra of the 4-FTP monolayer on Ni(111), where only two polarization curves are shown; the third, acquired at 50°, has been omitted for clarity. The inset in the carbon spectrum shows the determined adsorption angle of the molecules of 30°, defined between the phenyl ring backbone and the surface normal. For the fluorine spectrum, σ^* and π^*-type resonances are marked with red and blue lines, respectively.

The fluorine NEXAFS spectrum in Figure 5.6 (right) also shows a pronounced polarization dependence with an overall larger intensity for the 7° polarization and allows a separation into resonances of different characters. Since gas phase

calculations of 4-FTP show that a tilting of the C-F bond with respect to the phenyl ring plane is highly unfavorable [157], we can assume that the C-F bond angle is also about 30°, i.e. similar to the phenyl ring. The previous considerations and the reversed sign of the linear dichroism [146] relative to the C-K edge spectra point towards a dominant role of σ^*-type resonances in the 7° curve, in contrast to π^*-type resonances present under 90° polarization. This assignment will be further justified by the photon-stimulated desorption (PSD) experiments presented in 5.2.3.

Finally, from UPS measurements, the work function change upon monolayer adsorption can be determined from the width of the corresponding UPS spectra (not shown). The clean Ni(111) surface work function is measured to be $\Phi_{Ni(111)} = 5.33\,\text{eV}$, in very good agreement with common literature values [158], whereas the work function of the adsorbate covered surface is $\Phi_{4FTP} = 4.75\,\text{eV}$. This means that the work function is lowered by $\Delta\Phi = -0.58\,\text{eV}$ after formation of the monolayer. Taking a simple model into account, which has already proven useful for 4-FTP on Cu(100) and Cu(111), the change in work function upon adsorption of 4-FTP results mainly from two contributions: First, the intrinsic dipole of the molecule, which points from the fluorine substituent to the thiol group and is calculated to $|\mu_0| = 1.11\,D$ according to Ref. [140]. Second, the bond dipole upon metal-thiolate bond formation, which is proposed to point in the opposite direction of the intrinsic dipole in the case of 4-FTP/Cu(111) [140]. For the total dipole and hence the work function change, also the orientation of the molecules with respect to the substrate is important, since only the component of the intrinsic dipole that is parallel to the surface normal has an impact on the work function [140, 159]. Schmidt et. al observed a work function change of +0.16 eV for a saturation coverage of 4-FTP molecules, with a similar adsorption angle of 25° [140]. This result is in contrast to our findings and can tentatively be explained by the different S-Ni bond nature compared to S-Cu, which might result in a altered bond dipole. Furthermore, depolarization effects within the molecular layer could decrease the intrinsic dipole of the molecule [160,161] and explain the overall lowered work function obtained in our experiment.

5.2.2 Thermal Stability of the SAMs

Since the thermal stability of SAMs is a crucial property for possible applications, it will be investigated in this subsection by means of XPS. Typically, thiolate bonded self-assembled monolayers on rather inert metal surfaces like those of gold and silver are stable at room temperature [17,162], where stable

in this particular case means they do not undergo bond dissociation apart from the S-H bond cleavage upon adsorption. Considering the Ni(111) surface, further dissociation processes are likely to happen at elevated temperatures due to the increased reactivity of nickel compared to gold. Temperature dependent XPS spectra acquired to investigate possible dissociation mechanisms are shown in Figure 5.7.

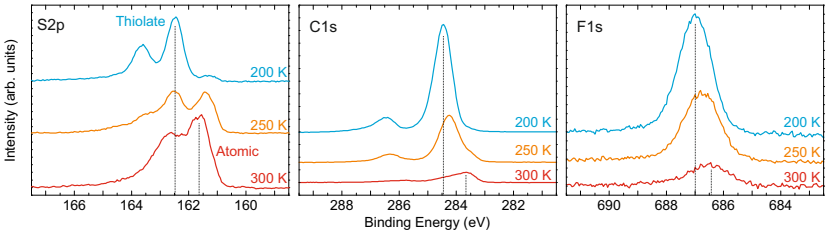

Figure 5.7: Temperature dependent XPS spectra of a 4-FTP monolayer on Ni(111), where the formation of atomic sulfur at temperatures above 200 K is visible in the S2p spectrum. In addition, the decomposition reaction can be followed by monitoring the evolution of the carbon and fluorine XPS spectra, as discussed in the main text.

S2p spectra taken at 200 K are identical to those in Figure 5.6 and show thiolate-bonded molecules as the majority species, whereas at 250 K, a mixture of thiolate and atomic sulfur is present on the surface. The C-S bond cleavage process is almost completed at 300 K, where atomic sulfur by far dominates in the surface composition. Comparing the intensities in the S2p spectra, it becomes evident that there is no desorption of sulfur from the surface, but rather formation of a sulfide overlayer occurs. By contrast, the intensity of the C1s peak decreases significantly upon annealing to 300 K, together with a lowering of the binding energy of the main C1s emission down to 283.6 eV. This is consistent with the interpretation that the S-C bonds break and the remaining aromatic carbon is in direct contact with the surface [163, 164], from where it finally desorbs or diffuses into the bulk at higher temperatures. The same holds for fluorine, which shows a similar trend in XPS, with a decrease in intensity accompanied by peak shift to lower binding energy. At 300 K, the F1s binding energy is lowered down to 686.4 eV, with a shift of −0.6 eV compared to the intact monolayer. This binding energy value excludes atomic fluorine directly on the surface [165], but rather suggests that the fluorine is still bound to the phenyl ring, although lying closer to the surface.

Summarizing these results, 4-FTP on Ni(111) is stable only up to 200 K;

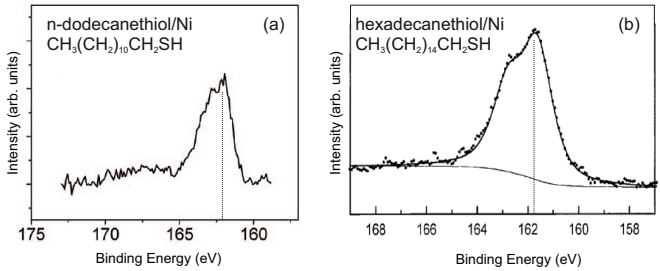

Figure 5.8: S2p XPS spectra of wet-chemically prepared alkanethiolate monolayers on nickel. Both spectra show a rather broad S2p doublet that is attributed to pure thiolate in the original articles. This assignment is questioned in this work as described in the text. Figures adapted from Refs. [121] and [128].

higher temperatures facilitate S-C bond cleavage and lead to an ill-defined monolayer consisting of atomic sulfur and phenyl ring fragments with fluorine still attached. These results are in excellent agreement with prior observations of benzenethiol on Ni(111), where S-C bond scission was shown to be the favored pathway for temperatures above 190 K [131], whereas methanethiol was found to dissociate at an even lower temperature of 150 K [166]. Nevertheless, some studies of alkanethiols prepared in solution on polycrystalline nickel suggest that formation of pure thiolate bonded monolayers without a considerable amount of atomic sulfur might be possible even at room temperature [121,128]. The S2p XPS core level spectra from these investigations are shown in Figure 5.8. Unfortunately, the spectra have not been acquired with a sufficient resolution nor has a peak fitting routine been applied, but they appear rather broad compared to those shown here for the intact monolayer (c.f. fig. 5.5). This suggests that the SAMs are not well-defined and a considerable amount of atomic sulfur is present, in contrast to the conclusions reported in the original articles.

To investigate the influence of the preparation conditions and to relate it to the above mentioned wet-chemical preparation method, 4-FTP was also deposited directly on the warm (300 K) substrate (still under UHV conditions), where the same amount of molecules as for preparing the multilayer in Section 5.2.1 was used. Figure 5.9 shows the XPS spectrum of the S2p core level together with the decomposition into the respective species. Clearly, the spectrum is less well defined compared to the preparation at 80 K (see Figure 5.5), and the most apparent change is the increase in the proportion of atomic sulfur from 5% to 25%. Comparing the spectra of Figure 5.8 with the

ones acquired in this work on the warm substrate (Figure 5.9) corroborates the conclusion that the surface composition of the wet-chemical preparation methods reported in Refs. [121] and [128] does not consist of pure thiolate bonded molecules, but can rather be described as a mixture of thiolate bonded species with a non negligible amount of atomic sulfur. This emphasizes the necessity of high-resolution XPS data to determine unambiguously the surface composition and chemical state of the rather complex, organic self-assembled monolayers on metal substrates.

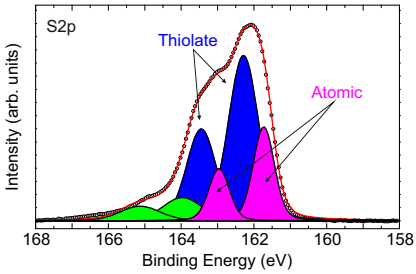

Figure 5.9: XPS of S2p core level for 4-FTP adsorbed on Ni(111) at 300 K. Experimental data are shown as dots, while the solid lines represent the results of curve fitting, where spin-orbit split doublets are marked with the same color. A high amount (>25%) of atomic sulfur is observable, and the overall peak shape is very similar to that of SAMs prepared under wet-chemical conditions (see Figure 5.8).

5.2.3 Evaluation of the Decay Spectra

As shown above, it is possible to prepare a well-defined, intact monolayer of 4-FTP on Ni(111), although only at temperatures below 200 K. Due to the fact that aromatic SAMs are promising candidates for molecular electronics (see e.g. [35]), the charge transfer dynamics for the tailgroup-to-substrate electron transport mechanism will be investigated in this subsection. Therefore, an electron from the F1s core level is resonantly excited into unoccupied molecular states and the decay electrons are analyzed within the framework of the core hole clock method (c.f. Section 3.3). Since excitation of an electron from the fluorine core level into an antibonding σ^* resonance is possible, the intermediate core-excited state can be dissociative, as it has been shown for halogen-containing molecules in the gas phase, like HBr, HCl or HF (see, e.g. [167–172]). This leads to a presence of both *molecular* and *atomic* features in the decay spectra and shall be investigated in the following for the

4-FTP monolayer.

Figure 5.10 shows a contour plot representation of the electron decay spectra following resonant F1s excitation in the range of the observed NEXAFS resonances for the multi- (a), (c) and monolayer (b), (d) as a function of the excitation energy. The polarization vector $\vec{E}$ of the electric field was chosen to be 7° with respect to the surface normal, to maximize the resonance intensity and hence the decay electron signal according to the NEXAFS data.

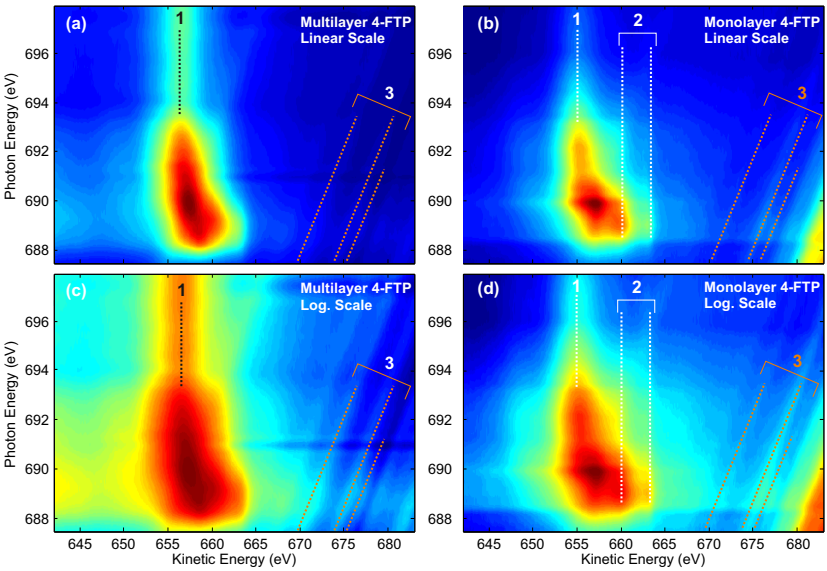

Figure 5.10: Contour plot representation of multilayer **(a)** and monolayer **(b)** electron decay spectra after resonant F1s excitation as a function of the photon energy. The data in the top panels **(a)** and **(b)** are plotted on a linear intensity scale, whereas **(c)** and **(d)** show the same data on a logarithmic scale to facilitate the peak identification also for the low intensity features. The decay channels are discussed in the text.

The decay spectra resemble the NEXAFS data, with a broad resonance centered around an excitation energy of 690 eV, which originates from resonant spectator and normal Auger decay. For photon energies higher than 693 eV, the various decay channels on the resonance converge into the normal Auger channel (1) of the intact molecule at 656 eV kinetic energy. A variety of bands with a linear dispersion (3) is visible at higher kinetic energies, their intensity

following the main resonance behavior. Due to their high kinetic energy and their dispersive behavior, they can be assigned to the participator lines of the intact molecule [171]. Two more features can be identified at constant kinetic energies of 659.5 eV and 693 eV, labeled (2) in Figure 5.10. These bands are more prominent in the monolayer, but close inspection shows that they are also weakly present in the multilayer. As mentioned above, dissociation via C-F bond breaking can occur after excitation of the F1s electron into an antibonding σ^* orbital, which would lead to the presence of decay electrons originating from *atomic* fluorine. According to their kinetic energies and their non-dispersive behavior, the bands denoted as (2) in Figure 5.10 are assigned to Auger decay electrons from atomic fluorine [171, 173]. The presence of the atomic bands in the monolayer decay spectra supports the dissociation of the intact molecule after populating the antibonding σ^* states of the F1s resonance.

To further elucidate the dependence of the dissociation process on the excitation energy, horizontal cuts at two different photon energies of the 2D decay spectra of Figure 5.10 are shown in Figure 5.11. By investigating the monolayer trace in Figure 5.11 (b), a clear enhancement of the peaks ascribed to the atomic Auger decay can be observed at an excitation energy of 689 eV, compared to the resonance maximum at 690 eV. Different final state configurations of the atomic fluorine decay are responsible for the two-peak structure, as it has also been observed in the dissociation of HF in the gas phase [171, 173]. The multilayer spectrum in (a) also shows the increase of the atomic fingerprint at 689 eV, but to a lower extent. This can be understood in terms of the ordering of the layers: In the monolayer, the molecules are standing approximately upright (see section 5.2.1), and the light vector of the exciting radiation is almost parallel to the C-F bond axis, which leads to a very effective population of the anti-bonding σ^* resonances. Conversely, the molecules are randomly oriented within the multilayer, and no special enhancement under this excitation geometry is expected.

To unambiguously identify the dissociation product as atomic fluorine and to support the previously drawn conclusions, the photon stimulated desorption (PSD) technique was applied to the system. Figure 5.12 (b) shows the experimental setup: The sample is irradiated with linearly polarized radiation and simultaneously, the F^+ fragments desorbing from the surface are monitored using a quadrupole mass spectrometer (QMS). Scanning the photon energy over the resonance yields the intensity of the fragment yield (F^+ in this case) versus the energy of the exciting radiation.

The experimental results for the PSD experiment of the 4-FTP monolayer are shown in Figure 5.12 (a, top), together with the corresponding NEXAFS

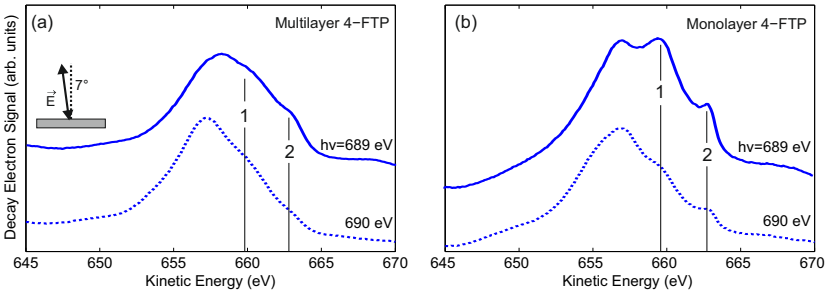

Figure 5.11: Electron decay spectra for 4-FTP/Ni of the multi- **(a)** and monolayer **(b)**. The features denoted with 1 and 2 originate from Auger decay of atomic fluorine and are discussed in the text. The inset in (a) depicts the polarization of the exciting radiation.

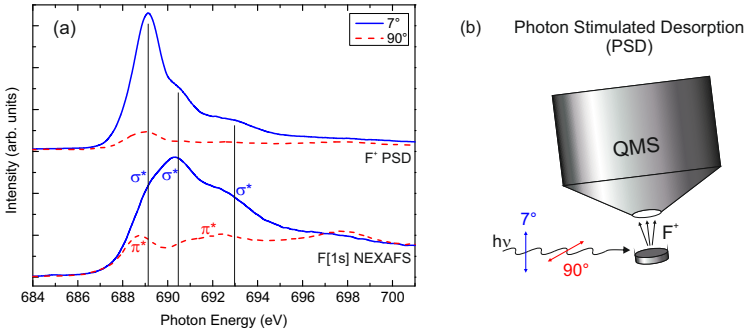

Figure 5.12: (a) PSD (top curves) and NEXAFS (bottom curves) spectra of a 4-FTP monolayer on Ni(111) shown for two different polarizations. According to the maxima in the PSD yield, an assignment of antibonding σ^* resonances and π^* resonances in the NEXAFS spectrum is facilitated. **(b)** Schematic experimental setup for PSD measurements, where fragments desorbing from the sample are detected with a quadrupole mass spectrometer (QMS) while the photon energy is varied.

spectra (a, bottom) for two different polarizations. The maximum of the PSD yield occurs at hν=689.1 eV, independent of the polarization vector and in excellent agreement with the interpretation of the decay spectra presented above. Furthermore, three distinct resonances can be identified from the PSD spectra with maxima at 689.1 eV, 690.5 eV and at 692.5 eV, which can also be correlated with maxima of the NEXAFS spectra. Another effect becomes apparent when comparing the PSD spectra of 7° (angle between light vector and surface normal) and 90°: The intensity of the 7° PSD curve is much higher compared to the 90° curve. This dichroism is due to fact that the excitation under 7° selectively promotes electrons into the antibonding σ^* orbitals that are oriented mainly along the C-F bond axis, whereas excitation into non-dissociative π^* orbitals is favored under 90° polarization. These results also enabled the determination of the resonance characters earlier in Section 5.2.1, as indicated in Figure 5.12.

Another important aspect concerns the timescale of the dissociation process: The excitation of an electron into a [F1s]σ^* resonance projects the molecule onto a different potential curve, which is in this case, due to its Ne-like behavior of F* in the Z+1 approximation, highly repulsive. While the molecule stays in the excited state, it keeps gaining energy from the elongation of the C-F bond until the excitation decays and the molecule reaches its final (core-excited) state. Depending on the energy gain during the lifetime of the resonance, the molecule will either end up in a *dissociated* or *intact* final state. Since here, an intense PSD signal of atomic fluorine in combination with atomic Auger features in the electron decay spectra are observed, we infer that the dissociation process must take place *before* the resonance is depopulated. The time necessary to depopulate the resonance is the charge transfer time τ_{ct}, which shall be investigated in detail in the following section.

5.2.4 Charge Transfer Dynamics

The study of charge transfer dynamics of the 4-FTP/Ni system is interesting by itself, since the F1s resonance has shown a quite complex behavior that can be reflected in the dynamics of the electron injection into the substrate as well. Furthermore, as mentioned above, it will help to determine the timescale of the dissociation process.

The starting point for evaluating the charge transfer process are again the decay spectra shown previously in Figure 5.10, but now with emphasis on the decay channels originating from the intact molecule. A distinct difference between the monolayer and multilayer spectra is the additional broadening

of the main resonance for the monolayer compared to the multilayer data. This broadening can originate from the presence of both autoionization and Auger decay channels in the monolayer, whereas for the multilayer, only the resonant decay is an effective de-excitation mechanism due to the missing coupling to the substrate. Therefore, the multilayer decay spectra serve as a reference for the lineshape of the "pure-autoionization" decay channel; a role similar to that of C16CN in Section 4.4.1.

The process for extracting the charge transfer times is identical as in Section 4.4.1: The decay spectra of the monolayer can be reconstructed by a pure autoionization and a pure Auger lineshape, with corresponding weighting factors. Here, the multilayer decay spectra represent the *pure autoionization* part (S_{auto}), and the Auger decay following non-resonant excitation of the monolayer at 705 eV corresponds to the *pure Auger* part (S_{Auger}). Applying a linear combination of these two contributions with the respective weighting factors I_{auto} and I_{Auger}, the monolayer decay spectrum can be reconstructed and the charge transfer time follows from: $\tau_{CT} = \tau_{core}\,(I_{auto}/I_{Auger})$ [74], with 3 fs for the lifetime τ_{core} of the F1s core hole [172].

Figure 5.13 shows the reconstruction procedure for two photon energies, (a) on the maximum of the resonance at 690 eV, and (b) at 691.5 eV. The measured decay spectrum of the monolayer (blue circles) is represented by a linear combination (red line) of the pure autoionization (green dash-dotted line) and the pure Auger (black dashed line) lineshapes. Prior to the reconstruction procedure, the non-resonant background (recorded at $h\nu = 680$ eV) as well as a Shirley-type background has been subtracted from all decay spectra and the spectra have been normalized to unit area. To obtain a good agreement between measured and reconstructed spectrum, the weighting factors were optimized until the sum of squared residuals has reached a global minimum. Is should be noted that the atomic decay features could not be reproduced adequately, because, as shown in Section 5.2.3, dissociation plays a minor role at $h\nu = 705$ eV, the energy where the Auger spectra were acquired.

In Figure 5.13 (a), corresponding to the maximum of the NEXAFS resonance, the autoionization part (0.64) is apparently larger than the Auger (0.36) fraction, resulting in a charge transfer time of 5.3 fs, whereas the situation is quite the opposite at a higher excitation energy of 691.5 eV, resulting in a much faster charge transfer of only 1.3 fs. Figure 5.14 shows the evaluation of the weighting factors (top panel) and the corresponding charge transfer times (bottom panel) for different photon energies across the resonance width. The error bars in Figure 5.14 result from the uncertainty of the reconstruction

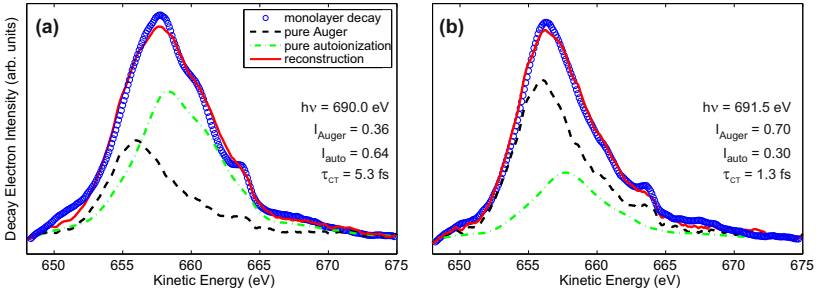

Figure 5.13: Reconstruction (red line) of the monolayer decay spectra (blue circles) by a linear combination of the pure resonant (green dash-dotted line) and pure non-resonant (black dashed line) lineshapes as described in the main text. Decay spectra on the resonance maximum at 690 eV **(a)** and at a photon energy of 691.5 eV **(b)** are shown. The resulting weighting factors and charge transfer times are also given in the respective plots.

procedure, whereas the error of the core hole lifetime has not been taken into account.

An overall trend of the charge transfer dynamics is the decrease of the CT time from 8 fs at the leading edge of the resonance to about 1 fs close to the ionization threshold at 691.75 eV. This decrease can be tentatively explained in terms of a lowering of the effective tunneling barrier with increasing excitation energy [60, 63], but it should be noted that the available free density of states and the overlap of the initial and final state wave functions can have a larger influence on the charge transfer times, as seen in Section 4.4.1. Also, the overlapping contributions of σ^* and π^* orbitals complicate a detailed analysis of the charge transfer dynamics. Interestingly, the charge transfer times show a maximum of 9.5 fs at 689 eV, which coincides with the maximum of the PSD yield. Since a longer lifetime of the resonance leads to a higher probability for dissociation (as discussed in 5.2.3), this explains the energetic position of the dissociation maximum, which *does not* simply coincide with the adsorption maximum at $h\nu = 690$ eV, but rather with the state associated with the longest charge transfer time.

Summarizing, these results show that the charge transfer from the core-excited fluorine to the nickel substrate takes place on an ultrafast timescale of only a few femtoseconds, which is in good agreement with similar aromatic self-assembled monolayers on gold [45]. This ultrafast process can be understood by the good conductivity of the aromatic system [35] and the rather

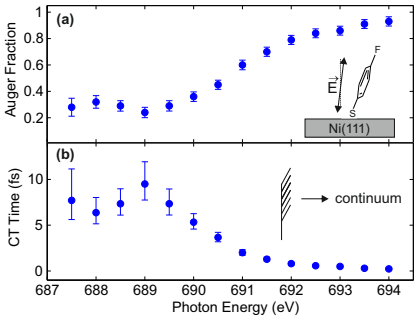

Figure 5.14: Behavior of the weighting factors **(a)** and resulting charge transfer times **(b)** as a function of the excitation energy. The inset in (a) shows the orientation of the electric field vector, whereas in (b) the threshold for continuum excitation is indicated.

high-lying resonance (2 eV above E_{Fermi} at $h\nu = 689$ eV) and furthermore shows the efficient coupling provided by the thiolate-nickel bond.

These findings also open up a route towards spectroscopic access to spin-dependent charge transfer dynamics in self-assembled monolayers: Once a monolayer of 4-FTP is grown on a magnetized thin film of nickel, spin-dependent detection of the decay electrons would allow one to determine charge transfer times that depend on the relative orientation of the spin of the excited electron and the magnetization direction of the substrate. This is possible, since the spin of the excited and detected electron are related for KLL Auger transitions, due to the prevalence of spin-singlet final states [174]. Due to the different available density of states for majority and minority carriers in ferromagnets, a significant difference in these transfer times can be expected, which would result in an organic spin-valve type behavior.

5.2.5 Conclusions for 4-FTP/Ni(111)

One of the main results of our study is that well-defined monolayers of 4-FTP can be prepared on Ni(111) under UHV conditions up to sample temperatures of 200 K. Below this temperature, the layers form thiolate bonds to the nickel surface and adapt an almost upright orientation, with the phenyl ring tilted about 30° away from the surface normal and the fluorine tailgroup exposed to the vacuum-monolayer interface. Annealing the layer to higher temperatures leads to a conversion from thiolate to atomic sulfur and the surface composition is no longer well-defined.

Analyzing the electron decay spectra following resonant F1s excitation revealed that the promotion of electrons into empty σ^* orbitals results in the ultrafast dissociation of the molecule. PSD measurements unambiguously identified F^+ ions as the dissociation product and enabled an assignment of the resonances observed in the fluorine K-edge NEXAFS spectrum. Furthermore, the charge transfer dynamics after resonant F1s excitation was studied and electron delocalization times between 10 and 1 fs could be obtained, thus illustrating the good conductivity of 4-FTP adsorbed on Ni(111).

5.3 3- and 4-Fluorobenzoic Acid SAMs on Ni(111)

In this section, 3- and 4-fluorobenzoic acid monolayers on Ni(111) will be investigated with regards to bonding character, molecular orientation, thermal stability and charge transfer dynamics. The main difference compared to 4-Fluorothiophenol is the different anchoring or headgroup: The thiol moiety is changed to a carboxyl group. This is motivated by the fact that 4-FTP monolayers on Ni(111) showed C-F bond scission for temperatures above 200 K, which hinders the use of such layers for, e.g. molecular electronic devices or well-defined surface protection coatings for nickel. In contrast to that, previous investigations of Neuber et al. have shown that benzoic acid (BA), C_6H_5-COOH, monolayers adsorbed on Ni(110) are stable even at elevated temperatures of 350 K [123]. The carboxyl group adsorbs on most transition metal substrates with the molecular plane perpendicular to the surface, as, e.g. in formic acid (H-COOH) [123]. Upon adsorption of formic acid on Ni(111), the molecule undergoes O-H bond scission and adsorbs as formate ($H\text{-}COO^-$) on the surface in a bidentate configuration, i.e. with two chemically identical oxygen atoms [175, 176]. The same mechanism is proposed for the adsorption of BA on Cu(110) [177, 178] and Ni(110) [123], leading to the formation of dense packed layers with the molecules in an upright geometry.

Here, two different precursor molecules with the fluorine either in the para (4)- or meta (3)-position of the phenyl ring of the fluorobenzoic acid will be investigated upon adsorption on Ni(111).

5.3.1 Electronic Structure and Adsorbate Geometry

A saturated monolayer of 4-FBA and 3-FBA on Ni(111) can be easily prepared by dosing[1] the molecules for 5 minutes through a gate valve and a stainless steel tube directly onto the 80 K cold sample, followed by annealing to 300 K. This leads to desorption of the multilayer (as monitored by, e.g. XPS, TPD) and leaves a saturated monolayer behind, which will be the starting point for the following discussion.

Figure 5.15 shows the XPS spectra of O1s, C1s and F1s acquired for the 4-FBA (top) and 3-FBA (bottom) monolayers on Ni(111).

[1] Due to the high vapor pressure of 4-FBA and 3-FBA, they can be directly sublimated from the solid phase without using a heated evaporator.

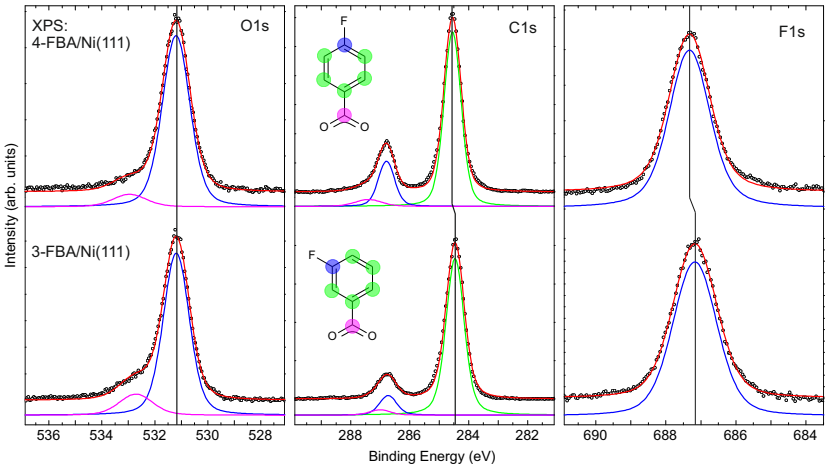

Figure 5.15: XPS spectra of 4-FBA (top) and 3-FBA (bottom), featuring the raw data (circles) and corresponding curve fits (solid lines) to facilitate the peak separation. The inset in the middle spectrum shows the origin of the different C1s emission lines from the adsorbed molecules. The energy positions of the main peaks and corresponding shifts are depicted with vertical lines.

XPS of 4-FBA First, the spectra for 4-FBA will be discussed, beginning with the O1s spectrum, which shows a pronounced maximum at a binding energy of 531.2 eV together with a weaker feature at 533.0 eV. The existence of mainly one peak points towards two chemically equivalent oxygen atoms in contact with the nickel substrate, following deprotonation of the carboxyl group and subsequent formation of a symmetrically bonded carboxylate [123, 179]. Nevertheless, the O1s binding energy of 531.2 eV is by 1.7 eV larger compared to the observed value of 529.5 eV for benzoic acid on Ni(110) in Ref. [123], whereas the binding energy of the carboxylate species for terephtalic acid (TPA) on Cu(100) is 531.4 eV [180], namely very close to our observed value. This illustrates that the binding energy of the chemisorbed carboxylate oxygen is very sensitive to the exact bonding geometry, which can be different for a hexagonal close packed (111) surface, compared to the more "open" (110) surface. The small O1s component at 533.0 eV can therefore be attributed to 4-FBA adsorbed with non-equivalent oxygens or in a minority adsorption site [123, 179], however it only contributes with 7% to the total oxygen signal and therefore represents a minority species.

In the top middle panel of Figure 5.15, the C1s XPS shows the main emis-

sion peak at 284.6 eV, characteristic for the C-H carbon in the phenyl ring, whereas the peak at 286.8 eV can be assigned to the carbon of the phenyl ring bonded to fluorine, similar to the case of 4-FTP/Ni(111) (see 5.2.1). The small shoulder of this peak at an even higher binding energy of 278.4 eV is due to emission from carbon bonded to the two oxygen atoms [123], as indicated in the inset of Figure 5.15. The low apparent intensity of the C-OO carbon emission is presumably due to the attenuation of the photoelectrons originating from the carbon closest to the surface, an attenuation that is very strong at the chosen 100 eV kinetic energy of the outgoing photoelectrons [155, 156]. Finally, the F1s XPS spectrum in the right part of Figure 5.15 shows a single emission line at 687.3 eV, comparable to the value of 687.0 eV for fluorine in 4-FTP/Ni(111) and thus indicating an intact molecule with the fluorine not in direct contact with the surface.

XPS of 3-FBA The binding energy of the main O1s emission line of 3-FBA shows no difference compared to 4-FBA, indicating a similar carboxylate formation and bonding mechanism as in 4-FBA. However, the intensity of the high binding energy peak at 532.7 eV is now larger by a factor of 2, suggesting that in the 3-FBA monolayer, 14% of the molecules are in a different chemical state other than that of the majority species as far as the oxygen atoms are concerned. This could be realized by a configuration where only one oxygen atom undergoes bond formation with the substrate and the other stays in its hydroxylated form.

In the C1s spectrum, the main emission line from the C-H aromatic carbon is now at a slightly lower binding energy of 284.5 eV, whereas the relative intensity of the C-F carbon has decreased by almost a factor of 2 compared to 4-FBA. This decrease in relative intensity can be understood by the substitution of the fluorine in the *meta*-position, which is, in an upright molecular geometry, less exposed (see NEXAFS section below) for 3-FBA than for 4-FBA. Following this discussion, the binding energy of the F1s level in 3-FBA is with 687.2 eV also lower than in 4-FBA, which is most likely due to the different electron densities of the phenyl ring at the para (4-FBA) and meta (3-FBA) positions, with respect to the carboxyl group [181].

The binding energies and relative intensities of the two systems together with the uncertainties derived from the curve fitting and energy calibration procedures are summarized in Table 5.2. When comparing the relative intensities of the C1s emission features from 4- and 3-FBA, it seems as if the C-F and C-OO components decrease by about 50% from 4-FBA to 3-FBA. This apparent change could be related to the different position of the fluorine atom, which attenuates the C-H emission more efficiently in 4-FBA than in

3-FBA. Therefore, the different relative intensities are most likely due to a normalization artifact and do not reflect the "true" chemical composition.

Table 5.2: Binding energies and relative intensities of the C1s, O1s and F1s XPS core levels for monolayers of 3- and 4-FBA on Ni(111) together with the uncertainties in the binding energies. The percentages are given with respect to corresponding core level.

		4-FBA		3-FBA	
Core Level	Type	BE (eV)	%	BE (eV)	%
C1s	C-H	284.6 ±0.05	77	284.5 ±0.05	87
	C-F	286.8 ±0.10	18	286.7 ±0.20	10
	C-OO	287.4 ±0.20	5	287.0 ±0.20	3
O1s	O-Ni	531.2 ±0.05	93	531.2 ±0.05	86
	OH	533.0 ±0.20	7	532.7 ±0.20	14
F1s	F	687.3 ±0.05	100	687.2 ±0.05	100

To obtain more detailed information on the bonding geometry and adsorption angles for the two systems, x-ray absorption spectra at the carbon, oxygen and fluorine K-edges have been acquired under three different polarizations (angle of electric field vector 7°, 50° and 90° with respect to surface normal). A typical set of partial electron yield NEXAFS spectra for the two systems is shown in Figure 5.16, where only spectra taken at 7° and 90° are plotted to improve the visibility of the absorption features.

NEXAFS of 4-FBA The low-energy range of the carbon K-edge spectrum for 4-FBA is dominated by 3 sharp peaks (labeled 1-3 in Figure 5.16) at 285.0 eV, 287.1 eV and 288.1 eV, which are most intense for 90° polarization. They can be mainly attributed to π^* resonances originating from excitations of the C-H, C-F and C-OO carbon, respectively, into the $1\pi^*$ orbital [182]. Excitations from the C-H carbon into the $2\pi^*$ are energetically very close to the $1\pi^*$ excitations [182] and can therefore not be resolved in the presented spectra, whereas excitations into the higher-lying $3\pi^*$ orbital are present at 289.3 eV (peak 4). An additional excitation from the C-H carbon into the lowest $1\sigma^*$ orbital is possible at nearly the same photon energy as the C-F$\rightarrow 1\pi^*$ excitation, resulting in a crossing point of the spectra with different polarizations. Above 290 eV, broad σ^* resonances dominate the spectrum, which shall not be further discussed here. The energetic positions and assignment of the NEXAFS resonances are summarized in Table 5.3. The small dip in the carbon spectra at 284.0 eV is due to contaminations on the beamline optics [77]

and could not be removed by the normalization procedure as described in Section 3.4, however it does not influence the quantitative determination of the adsorption angle within the given error bars of $\pm 10^\circ$.

Furthermore, the NEXAFS spectra for the carbon K-edge also show a pronounced linear dichroism, with the π^*-derived resonances almost vanishing for 7° polarization, indicating an upright geometry of the phenyl ring with respect to the underlying surface. Quantitative analysis of the absorption spectra yields an adsorption angle of the phenyl ring of $20 \pm 10^\circ$. Due to the aforementioned partially mixed π^* and σ^* resonances above 286 eV, only the most intense C-H$\rightarrow 1\pi^*$ resonance was used for determining the adsorption angle.

The main structure in the oxygen K-edge spectrum acquired at 90° polarization is dominated by two sharp resonances at 532.3 eV and 535.0 eV, labeled 1 and 2 in Figure 5.16, respectively. Excitations from the symmetrically bonded carboxylate oxygen into the $2\pi^*$ orbital are responsible for the largest resonance 1 [123], whereas promoting electrons from the intact hydroxyl group into the same unoccupied $2\pi^*$ orbital gives rise to the second resonance 2 [183]. Above photon energies of 537 eV, mainly broad σ^* resonances dominate the x-ray absorption profile [123]. The occurrence of the resonances 1 and 2 also support the assignment of the chemically different oxygens in XPS (cf. fig. 5.15). The NEXAFS spectrum recorded for 7° polarization shows a strong suppression of the two π^* resonances, which points towards an almost upright standing carboxyl group. Accordingly, the adsorption angle for the plane of the carboxyl group with respect to the surface normal is calculated to $5 \pm 10^\circ$. Considering the dotted lines in the oxygen NEXAFS spectrum, which illustrate the Fermi step, it is apparent that the step for 7° polarization is shifted to lower excitation energies compared to the step for the 90° curve. The appearance of a step-like behavior *before* the main resonance can be interpreted as an excitation of electrons to molecule-metal hybrid states above the Fermi level, which is typical for adsorbates that interact strongly with the metal substrate [77], and also in accordance with results of BA/Ni(110) [123]. Since the intensity of the step depends on the number and symmetry of electronic levels near the Fermi level in both adsorbate and metal surface [77], a polarization dependent difference of theses properties could explain the shift of the Fermi step. If, e.g. the density of available metal-molecule hybrid states near the Fermi level is larger for states with d_z-character (where z points along the surface normal) compared to in-plane orbitals, a more intense and even shifted Fermi step associated with a resonance could be observed for 7° polarization. However, further experiments are needed to validate this hypothesis.

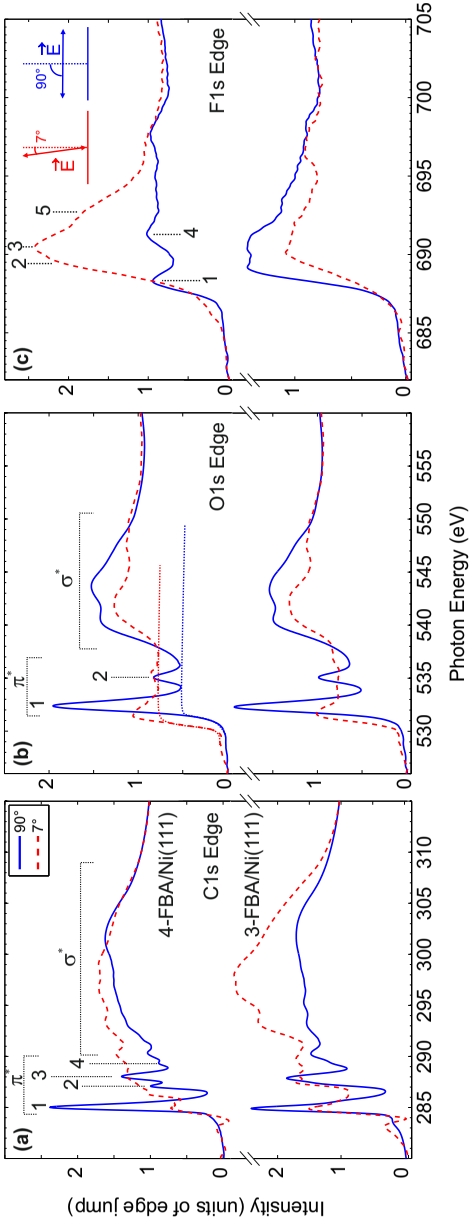

Figure 5.16: NEXAFS spectra of 4-FBA (top) and 3-FBA (bottom) monolayers on Ni(111) taken at different polarizations on the carbon (left), oxygen (middle) and fluorine (right) K-edges. The individual peak positions are numbered and assigned in the main text and summarized in Table 5.3. The dotted lines in the oxygen spectrum for 4-FBA illustrate the Fermi edge, as discussed in the main text.

Inspecting the fluorine K-edge spectrum, the similarity in lineshape and dichroism compared to 4-FTP/Ni described in Section 5.2.1 is apparent, and thus the peak assignment is analogous as well. This is justified by the fact that the fluorine substituent is hardly affected by the different headgroups, and the same holds for the unoccupied orbitals on the phenyl ring in the vicinity of the fluorine. Since the σ^* resonances are most intense for 7°, the C-F bond follows the orientation of the phenyl ring and is almost parallel to the surface normal. However, a quantitative analysis of the F1s NEXAFS spectrum is hindered by the fact that it consists of several overlapping π^* and σ^* resonances (cf. section 5.2.1).

Table 5.3: NEXAFS resonance energies and assignments for monolayers of 3- and 4-FBA on Ni(111).

Edge	hν (eV)	No.	Assignment
C-K	285.0	1	C-H$\rightarrow 1\pi^*$ C-H$\rightarrow 2\pi^*$
	287.1	2	C-F$\rightarrow 1\pi^*$ C-H$\rightarrow 1\sigma^*$
	288.1	3	C-OO$\rightarrow 1\pi^*$
	289.3	4	C-H$\rightarrow 3\pi^*$
O-K	532.3	1	OO-Ni$\rightarrow 2\pi^*$
	535.0	2	OH$\rightarrow 2\pi^*$
F-K	688.3	1	F$\rightarrow \pi^*$
	689.5	2	F$\rightarrow \sigma^*$
	690.5	3	F$\rightarrow \sigma^*$
	691.3	4	F$\rightarrow \pi^*$
	693.0	5	F$\rightarrow \sigma^*$

NEXAFS of 3-FBA The C1s NEXAFS spectrum for 3-FBA in Figure 5.16 is very similar to that previously shown for 4-FBA, with the only apparent changes being the different linear dichroism and the less clear separation of the peaks labeled 2 and 3 for 90° in the 4-FBA spectrum. Evaluating the polarization dependence results in an adsorption angle belonging to the phenyl ring of $30 \pm 10°$, which means the molecules are slightly more tilted towards the horizontal plane than 4-FBA, but still in an overall upright configuration. Since peak 2 has also σ^* contributions, which are more pronounced at this adsorption angle at 90° polarization, the separation between the resonances 2 and 3 gets less pronounced, thus resulting in the rather broad peak around 287.5 eV.

The oxygen K-edge spectrum is very similar to the one discussed for 4-FBA, with a resulting adsorption angle of the carboxylate group of $7 \pm 10°$ and a comparable shift of the Fermi step.

Finally, the F1s NEXAFS spectrum shows distinct changes, compared to 4-FBA, among which the weaker and reversed dichroism is the most prominent one. Here, the overall intensity belonging to the 90° curve is slightly larger, in contrast to 4-FBA, thus suggesting an approximately 45° alignment of the C-F bond to the surface plane. This can be understood as a consequence of the fluorine substitution in the meta position, which results in a 60° angle of the fluorine with respect to the vertical axis of the phenyl ring in the gas phase.

The positions and assignments of the NEXAFS resonances for 4-FBA and 3-FBA adsorbed on Ni(111) are summarized in Table 5.3. A model of the adsorption geometry as derived from the NEXAFS data is shown in Figure 5.17. In the presented model, only the adsorption angle is realistic, since NEXAFS without further theoretical modeling is not capable of obtaining reliable information on, e.g. adsorption sites. Furthermore, due to the 3-fold symmetric Ni(111) surface, no information on the azimuthal orientation of the molecules with respect to the substrate can be extracted. However, the observed, mostly upright geometry of both molecules is in good agreement with investigation of benzoic acid (BA) on Ni(110), where the tilt angle of the molecule was determined to be 30° with respect to the surface normal [123]. According to that, the substitution of a hydrogen with a fluorine in the meta or para position of the phenyl ring does not seem to influence the resulting adsorption geometry, at least as long as the polar angle is concerned.

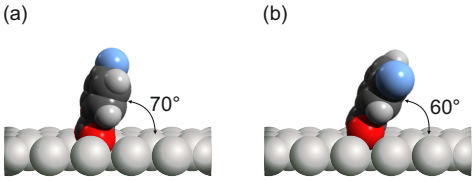

Figure 5.17: Proposed model of adsorption geometries for **(a)** 4-FBA and **(b)** 3-FBA on Ni(111) derived from the NEXAFS data. The adsorption angles of 70° for 4-FBA and 60° for 3-FBA are given with respect to the surface plane.

5.3.2 Thermal Stability of the SAMs

In this subsection, the thermal stability of 3- and 4-FBA on Ni(111) will be discussed, using fast-XPS to follow the changes during annealing. In fast-XPS, the temperature of the sample is linearly increased (2 K/s in this case) while, simultaneously, XPS spectra with about 10 s acquisition time are acquired. This allows a direct monitoring of the temperature dependent evolution of core level XPS spectra, without the necessity of carefully selecting the temperature steps before acquiring the corresponding spectra. For each presented temperature-dependent core level spectrum, a new preparation cycle was performed. Figure 5.18 shows the fast-XPS spectra for 4-FBA (top panels) and 3-FBA (bottom panels) in the temperature range of 300 to 750 K using a color-coded 2-D representation. Apparently, the set of spectra for 4-FBA and 3-FBA is very similar, therefore we will first focus the discussion on the spectra acquired for 4-FBA and address possible differences later on.

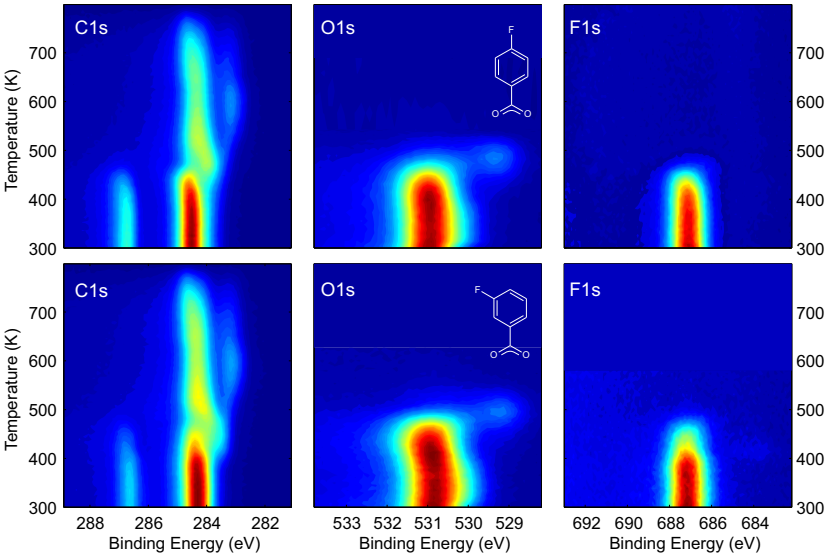

Figure 5.18: Fast-XPS spectra of 4-FBA (top panels) and 3-FBA (bottom) monolayers adsorbed on Ni(111) for the C1s (left), O1s (middle) and F1s (right) core levels. The contour plots show the intensity of the XPS signals as a function of binding energy and sample temperature. The intensity ranges from dark blue (lowest) to dark red (highest) and is normalized for each spectrum.

Firstly, all three (C1s, O1s and F1s) spectra do not show major changes below 380 K, in intensity as well as peak shape, which implies that the molecules are thermally stable, even at relatively elevated temperatures, in contrast to the thiolate-coupled 4-FTP/Ni (cf. 5.2.2). The first changes appear simultaneously in all spectra slightly above 400 K, with the most notable change in the oxygen and fluorine 1s spectra. Considering the F1s emission, the overall intensity decreases dramatically, resulting in a complete disappearance of fluorine at 500 K. During the decrease of the F1s intensity, the lineshape of the emission signal stays almost constant, indicating no chemically different intermediate product and suggesting a direct dissociation of the C-F bond with subsequent desorption of fluorine. A different scenario could involve atomic fluorine directly adsorbed on the metal surface as a result of the C-F bond scission, but apart from a minority species (see below), this is not the main decomposition channel.

Inspecting the traces of the O1s emission, a similar behavior as for fluorine is observed: small variations in lineshape and intensity below 440 K, but a significant change starting at higher temperatures. Similarly to the F1s spectra, the intensity of the O1s emission shows a strong decrease starting around 450 K, which is completed at 530 K. This also suggests that the oxygen is split off from the phenyl ring at elevated temperatures and finally desorbs, which is the dominant desorption channel for this fragment. Since desorption of CO from BA/Ni(110) does not occur below 500 K [123], we also conclude that the oxygen does not desorb as CO, but rather as O_2. Nevertheless, the O1s spectra show some intensity at a lower binding of 529.3 eV, with a maximum at a temperature around 500 K. According to the binding energy, this photoemission signal originates from oxygen that is chemisorbed on the nickel surface, namely as NiO [184]. This intermediate species disappears at temperatures above 530 K, most likely due to diffusion into the bulk.

The evolution discussed so far can also be followed by analyzing the C1s contour plot in Figure 5.18 for 4-FBA (top left). No apparent change is visible below 380 K, in very good agreement with the previously analyzed F1s and O1s XPS spectra. Beginning at 380 K, the intensity of the main carbon emission at 284.5 eV as well as the C-F and C-OO carbon signals at higher binding energies start to decrease, indicating C-F and C-OO bond scission as well as decomposition of the phenyl ring. Since the intensity of the C-H carbon has decreased by about 80% at 480 K, a first decomposition reaction seems to be completed. For comparison, (deuterated) benzene on Ni(111) shows an onset of the D_2 desorption around 380 K followed by a maximum at 450 K and a weaker, broad tail up to temperatures of 700 K which was interpreted as the stepwise dehydrogenation of the phenyl ring [185]. Similarly, BA/Ni(110) does not desorb intact, but undergoes decomposition and

shows a maximum of phenyl desorption around 545 K [123]. Above 500 K, the main species on the surface in our case are hydrocarbon fragments, since the XPS emission lines of fluorine and oxygen have vanished almost completely at this temperature. These fragments finally disappear at temperatures above 780 K, most likely by diffusion into the bulk, thus completing the decomposition reaction. Another intermediate carbon product appears at temperatures around 600 K, at a binding energy of 283 eV, and vanishes above 650 K. According to the low binding energy, it is most likely due to a nickel-carbide species [186].

The discussion above applies to both 4-FBA and 3-FBA, with only minor differences between the two systems. Nevertheless, close inspection of the F1s trace of 3-FBA reveals a new species at a binding energy of 684 eV, with a maximum intensity around 420 K, that is not present in the corresponding 4-FBA spectrum. This species is likely to be atomic fluorine chemisorbed onto the nickel surface, according to the low binding energy [187]. It is only present up to 450 K, above this temperature desorption lead to the disappearance of this intermediate species. Due to the low intensity of this emission signal, only a very small amount of fluorine is adsorbed directly on the surface for 3-FBA, in contrast to 4-FBA, where this species is not present at all. This could be understood from the closer proximity of the fluorine to the surface in 3-FBA compared to 4-FBA, which will increase the probability of this channel. Apart from this effect, the decomposition reactions of 3- and 4-FBA do not show major differences and are thus considered to be very similar.

Summarizing these results, the monolayers of 3- and 4-FBA are stable up to approximately 380 K. Above this temperature, fluorine and oxygen abstraction, accompanied by a stepwise decomposition of the phenyl ring at higher temperatures, leads to the complete dissociation of the molecules on the surface. The most striking difference compared to the 4-FTP monolayers on Ni(111), is the increased temperature stability by approximately 180 K, achieved by changing the headgroup from a thiolate to a carboxyl group. In a simple chemical picture, this can be understood by the different coupling strengths of the thiolate-nickel and carboxyl-nickel bonds. Assuming that the thiolate bond is stronger than the carboxylate bond (c.f. Section 2.1.1), less electron density remains for the bond to the phenyl ring, thus making it more susceptible for bond dissociation [134, 135, 188]. In the following subsection, the charge transfer dynamics of the carboxyl-coupled monolayers will be investigated and compared to the results obtained for 4-FTP in Section 5.2.4.

5.3.3 Charge Transfer Dynamics

Figure 5.19 shows the decay electron spectra following resonant F1s excitation for monolayers of 4-FBA (top panels) and 3-FBA (bottom panels) as a function of the excitation energy in a 2D contour plot diagram. For both systems, two excitation geometries were chosen to investigate possible polarization dependent effects of the charge transfer dynamics, as already observed for SAMs on gold (cf. Chapter 4 and Refs. [45,94]). For the panels labeled (a) and (c), the polarization vector is tilted 20° from the surface normal, whereas for (b) and (d), the angle between polarization and surface normal was 20°, as indicated in the insets of Figure 5.19.

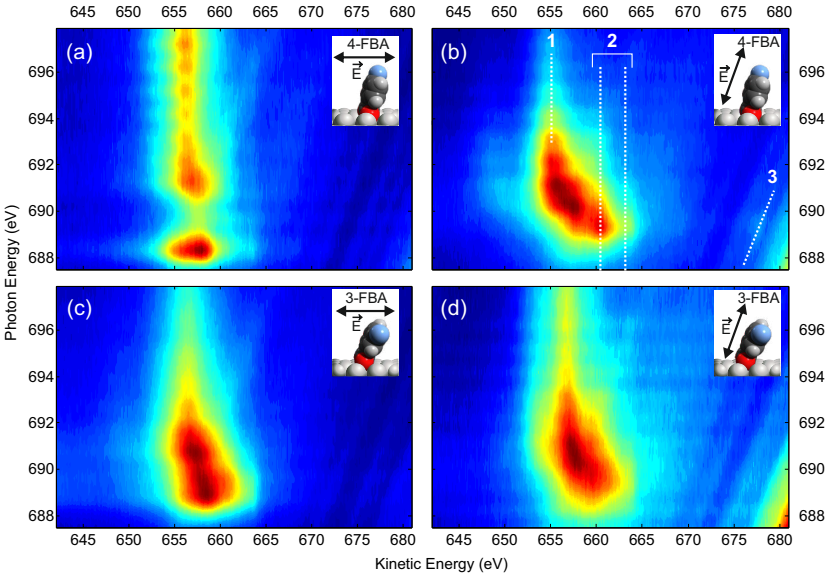

Figure 5.19: Decay electron spectra following resonant F1s excitation as a function of the excitation energy for monolayers of 4-FBA (top) and 3-FBA (bottom) on Ni(111). Shown are contour plot representations of the normalized 2D datasets, where dark red (dark blue) corresponds to the highest (lowest) intensity. The insets indicate the adsorption geometries as derived from NEXAFS, together with the different polarizations used in the experiment, as detailed in the main text.

The contour plot (b) of 4-FBA is very similar to that shown in Figure 5.10 for the monolayer of 4-FTP, with the main features assigned analogously. The

channel labeled (1) is the normal Auger decay band at constant kinetic energies, (2) denotes the channels arising from Auger decay of atomic fluorine after dissociation (cf. Section 5.2.3) and (3) can be identified as the participator decay of the intact molecule. Differences are found however, when comparing the spectra acquired for 4-FBA with two polarizations, as shown in panels (a) and (b). For 90° polarization, the decay spectra are dominated by an Auger like channel centered around 656 eV, whereas resonant participator decay features are missing or strongly suppressed. This is consistent with the observation that for (a), the kinetic energy distribution of the decay electrons on the main resonance (688 eV to 694 eV) is very narrow, basically resembling the Auger channel, in contrast to (b), where an admixture of autoionization channels leads to a broadening of the resonance. Hence, the charge transfer for 90° polarization seems more efficient, since channels, which represent no charge transfer (autoionization channels) are strongly suppressed compared to 20° polarization.

On the contrary, the corresponding spectra for 3-FBA (lower panels in Figure 5.19) show only very subtle differences depending on the polarization. This can be understood by considering the different adsorption and molecular geometries for 3-FBA (inset in fig. 5.19), where the C-F bond is tilted by ∼45° with respect to the surface normal, thus minimizing the differences between 20° and 90° polarization. This is also supported by the fluorine K-edge NEXAFS spectra of 3-FBA, which showed almost no linear dichroism (cf. Section 5.3.1). Therefore, the decay spectra for 3-FBA can be seen as a superposition of spectra (a) and (b). Nevertheless, the appearance of participator decay bands, as well as the overall slightly broader (in terms of kinetic energy) resonance for 20° polarization, point towards a less efficient coupling to the substrate and therefore longer charge transfer times than for excitation under 90°.

To investigate the charge transfer times quantitatively, an analysis of the 2D decay spectra within the core hole clock framework was performed, analogously to the procedure described for 4-FTP in Section 5.2.4. Due to unavailable 3- and 4-FBA multilayer decay spectra, we used the multilayer data acquired for 4-FTP (cf. Figure 5.10, panel (a)) throughout the analysis. This is motivated by the fact that the different headgroups should only marginally influence the decay spectra following resonant excitation in the multilayer. It is also common practice in the CHC analysis of SAMs on gold to use different molecules (e.g. C16CN vs. C2CN) for obtaining "pure" autoionization spectra [41, 44, 45, 94, 110].

Figure 5.20 shows the obtained[2] Auger ratios ($\frac{I_{Auger}}{I_{auto}}$) and corresponding

[2]For a detailed description of the fitting procedure and extraction of the Auger ratios

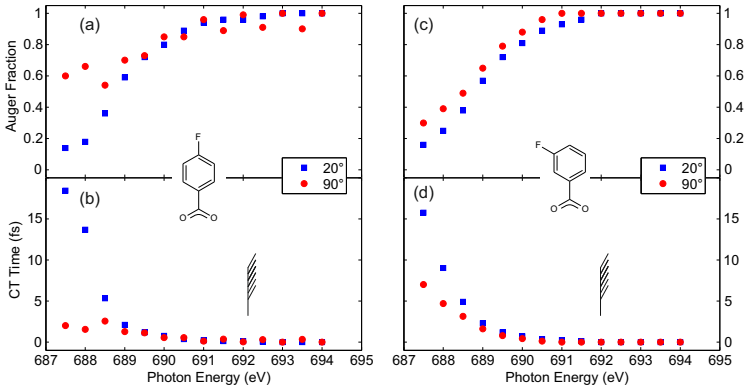

Figure 5.20: Auger fractions (top) and charge transfer times (bottom) obtained for 4-FBA (left) and 3-FBA (right) monolayers on Ni(111) for resonant F1s excitation. Values for excitation with the electric field vector 20° (90°) with respect to the surface normal are shown with blue squares (red circles). The vertical bars in the charge transfer time plots mark the ionization threshold. Error bars have been omitted for the sake clarity, the ranges of the errors are similar as in Figure 5.10.

charge transfer times for the 4-FBA (left panels) and 3-FBA (right panels) monolayers on Ni(111). Depending on the polarization, the CT times obtained for 4-FBA show remarkable differences, with overall larger CT times for 20° polarization in the region below 689 eV. At 687.5 eV excitation energy, the CT time for 20° is 18 fs, in contrast to only 2 fs for 90° polarization. With increasing photon energy, the transfer times for both polarizations decrease until they finally converge around 690 eV, advancing the ionization threshold and showing no more polarization dependence. Focusing on 3-FBA (right panels), the situation is quite different. As already suspected from the decay spectra, the obtained CT times are similar for the two polarizations, with slightly larger values for 20° polarization, but the same overall trend. Apart from the distinct dependence on the polarization, the charge transfer times for 4- and 3-FBA show similarities and both lie between 18 fs to 1 fs in the range of the main resonance.

In the following, the peculiar dependence of the CT times on the polarization will be discussed, focusing on 4-FBA, where the contrast is the strongest. The much faster CT times for 90° polarization suggest a very efficient coupling of the resonance to empty metal states. As previously discussed (cf. Sec-

and charge transfer times, refer to Section 5.2.4.

tion 5.3.1), the F1s x-ray absorption spectrum consists of several overlapping σ^* and π^* states that are populated during the excitation step. Previous investigations have shown that the charge transfer times in adsorbate/substrate systems depended mainly on three parameters: the energy position of the resonance relative to the Fermi level, the coupling of the populated resonance to the empty states [45, 94] and the available empty density of states (DOS) together with the band structure of the metal [63].

The first parameter, the resonance energy, has direct impact on the effective tunneling barrier, since an *increase* of the resonance energy leads to a *decrease* of the effective barrier height and therefore results in a faster charge transfer. The overall almost exponentially decreasing CT times for 20° polarization of 4-FBA and both polarizations of 3-FBA could be explained by this parameter, in contrast to the polarization dependence, which is present at the *same* excitation energy. Nevertheless, investigations of charge transfer dynamics of argon on metal surfaces have shown that often the *inverse* behavior is observed: *Increasing* the excitation energy leads to an *increase* in CT time [63]. In this case, the explanation is based on the available DOS and band structure of the adsorbate/substrate system. This explanation is also unlikely since the overall empty density of states is not affected by the polarization of the radiation, when keeping the photon energy constant[3]. The situation is different when the coupling of the resonance to the substrate is investigated. Here, it has been shown that the overlap of the resonantly populated states with the mediating phenyl backbone [45] or methylene units (cf. Chapter 4) and the anchoring group is essential for the efficiency of the charge transport. Excitation of the F1s resonance in 4-FBA with 20° polarization leads to a population of mainly σ^*-type orbitals, according to NEXAFS data (see section 5.3.1), whereas 90° polarization populates π^*-type states. Since the conjugated π electron system of the phenyl backbones is important for the charge transport [35], a more efficient transfer can be expected for promoting the electron into a π^*-type states with 90° polarization. Conversely, the coupling of σ^* resonances with the π electron system of the ring can be expected to be poor; therefore the larger CT for 20° polarization can be explained using this simple model. Furthermore, the similar behavior of the CT times for 3-FBA can be understood by considering the simultaneous population of σ^* and π^* type resonant states, due to the different structure and adsorption geometry of the molecule.

[3] It should be noted that the possibility of more available empty metal states with mainly d_z character exists, as discussed in Section 5.3.1. However, since here the excited fluorine is located rather far away from the metal and therefore not directly hybridized, a purely substrate dependent effect seems unconvincing.

5.3.4 Conclusions for 3- and 4-FBA/Ni(111)

Summarizing these results, deposition of 3- and 4-FBA onto the Ni(111) substrate leads to the formation of well-defined self-assembled monolayers that are stable at room temperature and even above, in contrast to thiolate-bonded monolayers (cf. Section 5.2.2). Bonding of the molecules to the surface is accomplished by deprotonation of the carboxyl group and subsequent formation of a symmetrically bonded carboxylate. The adsorption geometries of 3- and 4-FBA are both upright, with similar angles between phenyl rings and surface normal of 30° and 20°, respectively. Detailed investigations of the thermal stability have shown that both systems stay intact up to temperatures of 380 K, whereas above that temperature, the molecules do not desorb intact but they rather undergo a stepwise decomposition with fluorine and oxygen abstraction as the starting processes. Apart from minor differences, the thermal behavior of both systems is very similar and mostly affected by the headgroup-substrate binding mechanism.

Examination of electron decay spectra following resonant F1s excitation revealed an interesting polarization dependence of the charge transfer times. For 4-FBA, excitation with the polarization parallel to the surface normal resulted in delocalization times between 18 to 2 fs, whereas perpendicular excitation yielded in faster times always below 3 fs. This effect was shown to be related to the predominant population of either σ^* or π^* type resonances, which couple differently to the phenyl backbone, depending on the polarization.

5.4 Conclusions

The adsorption of two types of aromatic precursor molecules with thiol and carboxyl headgroups on Ni(111) was investigated by means of angle-resolved NEXAFS spectroscopy, TPD, XPS, UPS, PSD and resonant Auger spectroscopy. Both systems form well-defined self-assembled monolayers, in which the molecules adopt an almost upright adsorption geometry. The main difference between 4-FTP and 3/4-FBA is the thermal stability: Whereas 4-FTP dissociates above 200 K by S-C bond cleavage, 3- and 4-FBA monolayers stay intact up to temperatures of 380 K. This behavior could be explained with the different coupling strengths of the thiol and carboxyl groups to the nickel surface. Furthermore, all investigated system showed evidence for ultrafast C-F dissociation upon resonant excitation of a F1s electron into unoccupied σ^* orbitals of the molecule. This behavior also enabled the assignment of

the resonances in the fluorine K-edge NEXAFS spectrum, which consists of several overlapping σ^* and π^* resonances.

The charge transfer dynamics following the resonant F1s excitation showed similarities in all systems, with charge transfer times in the low femtosecond regime. Differences in the delocalization times measured for 3- and 4-FBA could be explained by the different position of the fluorine atom and the therefore different population of σ^* or π^* type resonances. Nevertheless, the charge transfer from 4-FTP to the substrate was overall faster compared to 4-FBA measured with the same polarization. This points towards a stronger coupling of the thiolate-bonded molecules compared to the carboxyl-bonded entities, similar to what has been observed on gold [189]. With regard to potential applications, carboxyl-coupled SAMs were shown to be superior to the conventional, thiolate-bonded monolayers due to their enhanced temperature stability.

Chapter 6

Spin-Dependent Electron Transfer Dynamics Probed by Resonant Photoemission Spectroscopy

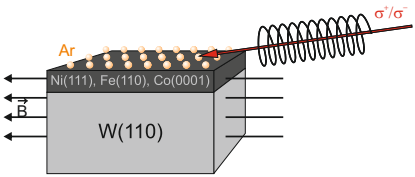

Abstract Resonant photoemission spectroscopy has been used to investigate the spin-dependent electron transport from core excited argon monolayers to ferromagnetic substrates with sub-femtosecond precision. Three systems have been studied to examine the dependence of the charge transfer times on the spin of the resonantly excited electron: Ar/Fe(110), Ar/Co(0001) and Ar/Ni(111). For argon adsorbed on iron and cobalt, a significantly faster charge transfer is found for minority electrons, whereas no evidence for a dependence on the electron's spin is seen on nickel. The results are explained considering the different empty densities of states of the metals for minority and majority electrons.

This chapter will be submitted as Ref. [190].

6.1 Introduction

Charge transport through atoms or molecules is important for redox reactions in chemistry and electrochemistry [98–100], the creation and cleavage of bonds by electronic excitations [191], ranging from unwanted beam damage in spectroscopy and microscopy [102] to sophisticated beam induced patterning of thin films [192], and the atom-selective bond modification by core-electron excitations [101]. Charge transfer reactions between atoms or molecules, and continua of states coupled to them, e.g. the occupied and unoccupied band states of metallic or semiconducting substrates at interfaces, are an important subset of these reactions. These processes are exceptionally important for dye-sensitized solar cells [104, 105], the entire field of DIET (desorption induced by electronic transitions) [193,194] and molecular electronics [35]. Recently it was recognized that the spin, apart from charge, bears additional information, stimulating widening of the field of molecular electronics to molecular spintronics [49, 50, 53]. Like molecular electronics, molecular spintronics requires coupling of molecular entities to electrodes for the communication with the macroscopic world; in this case, however, not only the transfer of charge, but also that of spins is an important topic.

As yet, most experiments on spin transport between electrodes and atoms or molecules have been performed by coupling two electrodes to the particle under investigation, typically such of ferromagnetic materials, and by recording the current through this arrangement as a function of applied voltage and magnetization of the two terminals [48, 195]. However, from a microscopic point of view, this approach has the disadvantage that always convolutions of effects from both electrodes are recorded, implying that electrode effects can cancel out. Consider, e.g. a non-magnetic molecule embedded between two electrodes of magnetized 3d metals, where transport data will yield conductance as a function of applied voltage and parallel or antiparallel electrode magnetization. However, it does not reveal the orientation of the traveling spins, i.e. it will not discriminate between tunneling of rather localized d electrons that cause the itinerant magnetism of these materials, or sp electrons, which have far reaching wave functions that support tunneling and transfer despite their lower density of states. Theoretical work for alkali atoms adsorbed on iron surfaces predicts prevalence of transport by coupling to sp states with different spin orientation than the d states over the entire energy range [196].

A method with direct access to the spin orientation inside the electrode and within the molecules is therefore necessary. We show that the core hole clock (CHC) approach is well suited for this purpose [74, 108, 109]. CHC uses the

known lifetimes of innershell vacancies (= core holes) as a time-ruler for the investigation of electron dynamics. A core electron is resonantly excited to an empty but bound electronic level, and the core-decay spectra are recorded. Depending if the core decay precedes or follows the delocalization of the resonantly excited electron in time, autoionization spectra with one-hole and two-hole one-electron final states (I_{auto}), or Auger-like spectra (I_{Auger}) with two-hole final states are obtained, respectively. Disentangling the measured data into these two contributions and taking the lifetime of the core-hole τ_C as a time standard yields the lifetime of the resonance, i.e. the delocalization time of the electron as $\tau_{CT} = (I_{auto}/I_{Auger}) \times \tau_C$. As an innershell-related technique CHC is atom-selective and, by excitation with narrow bandwidth photons of well-defined energy and polarization, also orbital selective [45, 94], for atoms as well as for molecules, covering time scales from sub-femtoseconds (fs, 10^{-15} s) to ∼100 fs.

In this Letter, we demonstrate that CHC can successfully be used for investigations of spin transport dynamics between a particle and a ferromagnetic substrate. We investigate monolayers of Ar on in-plane magnetized thin films of Ni(111), Co(0001) and Fe(110) on a W(110) substrate. We have chosen physisorbed Ar because it has been a model system in the development of CHC; its behavior is known in great detail [59–65, 197]. It is worth noting that spin selective CHC of adsorbates on magnets can be done in different ways. In this Letter we demonstrate CHC by spin polarizing the resonantly excited electron and recording the autoionization/Auger fractions for parallel and antiparallel alignments of photon spin and film magnetization. A suggestion for an alternative approach, based on spin resolved detection of the decay electrons rather than spin-polarized excitation, is presented in the outlook.

6.2 Experimental Methods

The experiments were performed under ultrahigh vacuum conditions at the undulator beamline UE56/2-PGM2 of the synchrotron facility BESSY II in Berlin. The ferromagnetic films were grown on a freshly cleaned W(110) surface, while their thickness (25-30 Å) was monitored during growth by a quartz microbalance. After subsequent annealing according to standard procedures [198–200], the film quality was checked by x-ray photoelectron spectroscopy (XPS) and low energy electron diffraction (LEED); the films were then magnetized in-plane by applying a magnetic field of 250 mT for 2 seconds. X-ray magnetic circular dichroism (XMCD) spectra were recorded at the $L_{2,3}$ edges of Ni, Co and Fe to verify the magnetization of the layer (see

Appendix C). For the experiments, the W[1$\bar{1}$0] direction was aligned within $\pm 15^{\circ}$ parallel to the incoming photon beam, which results in a polarization efficiency above 96%. Afterwards, a multilayer of argon was adsorbed onto the sample at 15 K and subsequently annealed until only a monolayer remained, as verified by XPS. X-ray absorption (XAS) spectra of the [Ar2p$_{3/2}$]4s resonance were acquired in the partial electron yield mode to determine the exact position of the resonance maximum, which is independent of the substrate at $E_{res} = 244.63$ eV. Taking into account the binding energy of the Ar2p$_{3/2}$ core level, the position of the Ar 4s resonance with respect to the Fermi level results in values of 2.97, 3.11 and 3.14 eV above E_F for Fe, Co and Ni, respectively. We note that the resonance position was not affected by the helicity direction of the circularly polarized radiation.

Electron decay spectra were then recorded for both parallel (I^+) and antiparallel (I^-) alignment of photon spin and sample magnetization, where both magnetization and direction of helicity were changed independently to eliminate systematical errors. Due to the selection rules for a $p \rightarrow s$ transition with right- (σ^+) and left- (σ^-) circularly polarized radiation, a spin selective population of the [Ar2p$_{3/2}$]4s resonance is accomplished with an efficiency of 3:1 [201]. For, e.g. parallel film magnetization and photon propagation direction, σ^+ radiation will predominately populate the Ar 4s resonance with "spin-down" electrons, which are in this case, referring to the density of states (DOS) of the underlying magnetized film, majority electrons. Briefly, I^+ excitation conditions result in a population of the resonance with majority electrons, whereas I^- excitation favors minority electrons[1]. This method enables us to control the spin of the electron in the resonance with respect to the spins of the ferromagnetic film, and therefore allows to investigate the spin-dependent charge transfer dynamics within the CHC framework.

6.3 Results and Discussion

Figure 6.1 shows a set of typical decay electron spectra of the three investigated systems for I^+ (solid line) and I^- (dashed) excitation conditions. Inspecting the traces belonging to the decay spectra measured on Fe and Co, a clear difference between I^+ and I^- excitation is present, most notably within the kinetic energy range of 216 - 220 eV. In both cases, the intensity of the decay spectra measured with I^+ excitation is significantly higher compared to I^- within that region. This suggests that the cross-section of the different

[1] We use the convention according to Refs. [82, 202] for defining the directions of helicity, photon spin and magnetization throughout the manuscript.

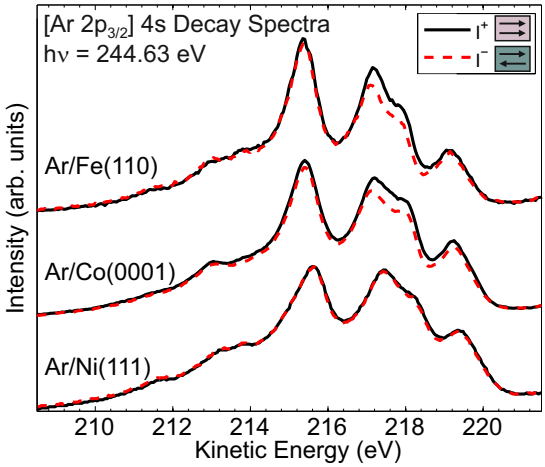

Figure 6.1: Electron decay spectra of an argon monolayer deposited on in-plane magnetized Fe(110), Co(0001) and Ni(111) thin films following resonant [Ar$2p_{3/2}$]4s excitation. Depicted are the intensities for parallel (I^+) and antiparallel(I^-) alignment of photon spin and substrate magnetization.

decay channels (autoionization vs. Auger) depends on whether the electron in the resonance possesses majority or minority spin. In contrast to that, no apparent difference is visible for the Ar/Ni system, thus indicating no dependence of the decay channels on the excitation conditions.

To quantify the changes in the respective decay channel intensities, the spectra were decomposed into the separate final state contributions by a fitting routine. Prior to that, the non-resonant background, recorded with an excitation energy 10 eV below the resonance, was subtracted from the spectra. A combination of asymmetric Voigt peaks was used to model the contributions of the different final states, with all lineshape parameters (relative height, width, position and asymmetry) kept fixed for the two different excitation conditions. The only varied parameter between the fitting of I^+ and I^- spectra was the ratio of autoionization intensity to Auger intensity, resulting in a very robust fitting procedure.

Figure 6.2 shows an exemplary fit of the decay spectra recorded for Ar/Co with two magnetization/photon spin combinations. The final states of the Ar 4s decay can be decomposed into two main groups: the autoionization states (orange) at highest kinetic energies and the Auger final states (blue),

which are shifted to lower energies. According to previous literature [59–65], each group consists of 3 (resolvable) multiplet configurations, as assigned in Figure 6.2, giving rise to the rather complex form of the decay spectra. At lowest kinetic energies, an additional group of peaks is visible, which is due to satellites (light orange) of the autoionization group and therefore also contains autoionization intensity [59,64]. Integrating the extracted Auger and autoionization intensities yields the ratio I_{auto}/I_{Auger}, and, together with the core hole lifetime of 6 fs [62], the charge transfer time.

For the representative case presented in Fig. 6.2, the charge transfer time for I^- excitation, i.e. for minority electrons, calculates to 2.94 ± 0.05 fs, whereas the majority electrons tunnel within 3.28 ± 0.05 fs into the substrate. This implies that the delocalization process for minority electrons is about 10% faster than for majority electrons. The error range given above is mainly due to systematic errors, whereas most error sources cancel when only the differences in charge transfer times for one preparation are considered. We also note the excellent reproducibility of our results: The standard deviation of the delocalization times extracted from 6 independent preparations of Ar/Co are below 0.04 fs.

Figure 6.3 shows the charge transfer times in dependence of the spin of the resonantly excited electron for all three investigated systems, which were derived analogously to the above described procedure. Argon adsorbed on iron shows overall smaller CT times than on cobalt, but minority electrons also delocalize faster by 0.32 ± 0.05 fs, thus very similar to the difference derived for Ar/Co. These results are further supported by an analysis of the width of the $[Ar2p_{3/2}]4s$ XAS spectra on Fe and Co: The full width at half maximum (FWHM) is larger by $\sim$5% for excitation of minority electrons compared to majority electrons. This also points towards a shorter lifetime of the resonance and a corresponding faster charge transfer time (see Appendix C for details).

Considering nickel as a substrate, the quantitative analysis confirms the initial expectation derived from Figure 6.1: There is no difference at all for the transfer times of minority and majority electrons for Ar/Ni. Compared to the work of Föhlisch *et al.* in Ref. [63], the delocalization times for Ar/Ni(111) obtained in this work are smaller by $\sim$1.5 fs. Preliminary investigations showed that this difference might be a result of the different excitation geometries (direction of electric field vector with respect to the surface) used in [63] and this work. Since here, the focus is on the *differences* in charge transfer times depending on the spin, we will not further detail the origin of this effect.

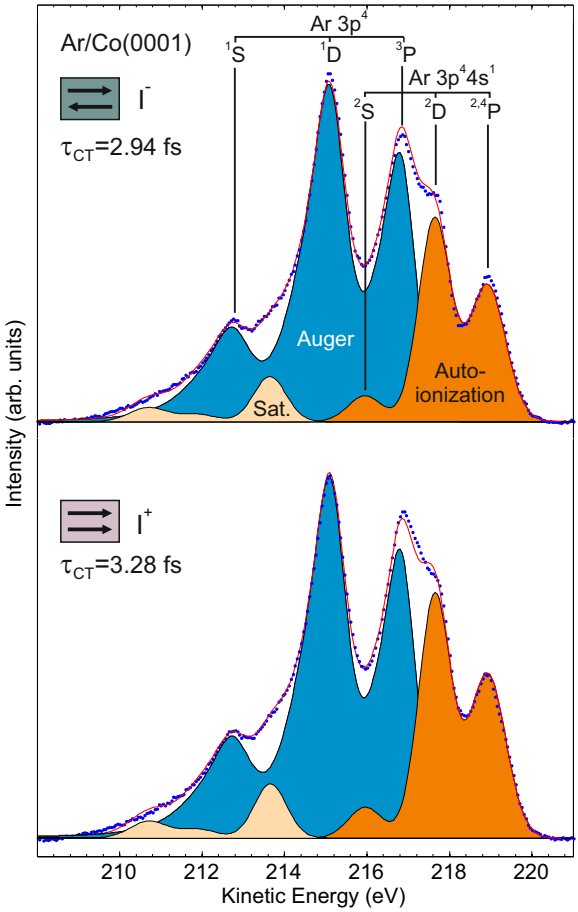

Figure 6.2: Exemplary decomposition of decay spectra for Ar/Co into autoionization (orange), Auger (blue) and autoionization satellite (light orange) final states by a strongly constrained fitting routine. Evaluation of spectra for parallel (bottom) and anti-parallel (top) alignment of photon spin and layer magnetization yield the corresponding charge transfer times as indicated in the figure. The final states of the decay are assigned in the top spectrum and discussed in the main text.

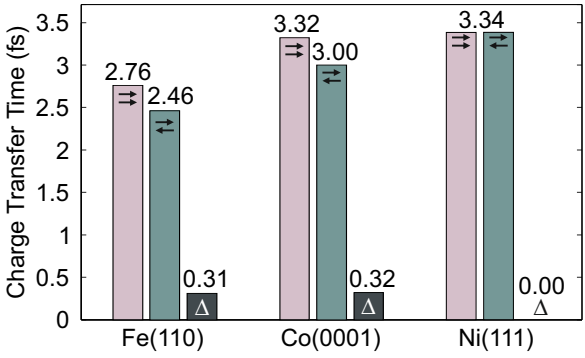

Figure 6.3: Comparison of spin-resolved charge transfer times for an argon monolayer adsorbed on thin films of Fe(110), Co(0001) and Ni(111). The direction of the spin of the excited electron and the magnetization of the layer are indicated with arrows in the figure. Δ denotes the difference of charge transfer times for parallel and antiparallel configuration of spin and magnetization.

In order to elucidate the mechanism that is responsible for the different charge transfer times, we will focus on the density of states (DOS) of the adsorbate/substrate system. Different CT times for Ar/Cu(111) and Ar/Cu(110) have been theoretically explained by differences in the projected electronic band structure of the two surfaces [64]; also for Ar/Ru(0001), detailed first-principle calculations showed that the unoccupied DOS and the coupling of the resonance to these empty states determines the charge transfer times [66]. As already mentioned in the introduction, recent theoretical work predicted different charge transfer times for majority and minority electrons of core-excited Cs/Fe(110) [196]. Mũino *et al.* explained the *faster* charge transfer of *majority* electrons with the fact that, despite the larger DOS for empty d states ("minority" states) at the resonance energy, the coupling of the core excited state is more efficient to empty sp states. Since the magnetization of d and sp states is opposite [58], this results in a faster charge transfer time for majority electrons, in contrast to our results. However, Mũino *et al.* note that this behavior is system-dependent and not a general result.

According to these findings, we plot the calculated empty DOS, at the Ar 4s resonance energy, of the d and sp states of iron, cobalt and nickel in Figure 6.4. For Fe and Co, the overall unoccupied DOS for minority electrons is larger than for majority electrons, due to the higher DOS of the d states. As discussed above, the sp states show a reversed behavior, with more available

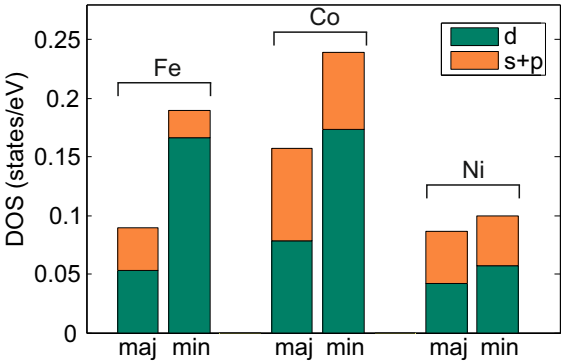

Figure 6.4: Spin-resolved, empty density of state of iron, cobalt and nickel at the Ar 4s resonance energies. The data were taken from [58].

states for majority electrons, in accordance with Ref. [196]. The same trend is also observed for nickel, but to a much smaller extent. These (limited) calculations provide the basis for understanding our findings: The difference between empty d states for *minority* and *majority* electrons of iron and cobalt seems to be responsible for driving the charge transfer, whereas this difference is very small (also the relative difference) for nickel, therefore leading to identical charge transfer times for both types of electrons.

These findings imply a more efficient coupling of the Ar 4s resonance to the empty d states for iron and cobalt. However, we stress that detailed theoretical investigations are needed for a quantitative understanding of the observed effects. We further note that this experimental approach is suitable for a variety of adsorbate/substrate system and not limited to adsorbed rare gases. Nevertheless, the possibility of spin-polarizing the resonance with circularly polarized radiation is mandatory, thus limiting the systems to a class with accessible, well-resolved spin-orbit split core levels to start from. For many organic systems of interest, which mainly consist of carbon, nitrogen and oxygen like molecular nano-structures on ferromagnetic substrates, no such initial states are available. Concerning these types of systems, which have possible technological applications as, e.g. organic spin vales [56], we propose a different type of experiment: Following the excitation of a $s \rightarrow p$ type resonance (e.g. [N1s]π^*), the decay electrons can be recorded using a spin-sensitive detector. Since the spin of the detected decay electron and the spin of the transferred electron are correlated for many elements of interest [174, 203], spin-dependent charge transfer investigations also become feasible for this

large and interesting class of materials.

6.4 Conclusions

In summary, we have shown that resonant photoemission spectroscopy can be utilized for investigating the spin-dependent charge transport from a rare gas adsorbate to a ferromagnetic substrate with sub-femtosecond precision. Our results showed that the charge transport process of core-excited argon is about 0.3 fs faster for minority electrons compared to majority electrons on iron and cobalt, whereas the delocalization times do not depend on the spin for argon on nickel. These findings were explained by considering the empty DOS of the substrates, where a more efficient coupling of the resonance to metal d states seems responsible for the faster charge transfer times for minority electrons.

Chapter 7

Summary, Conclusions and Outlook

Within this thesis, the electronic and structural properties of self-assembled monolayers and physisorbed noble gas layers have been explored by means of synchrotron-based electron spectroscopy methods. Understanding the bonding mechanisms of chemical entities to surfaces and the resulting formation of ordered nanostructures enables the identification of suitable molecular building blocks, which can then be used to create systems with tailored properties. Furthermore, the adsorption of molecules or atoms onto ferromagnetic substrates, rather than the more inert coinage metal surfaces, offers new exciting possibilities such as the spectroscopic investigation of spin-dependent electron transport.

In a first set of experiments, the core hole clock method has been used to extract subtle differences in the electron transfer times from cyano-terminated alkanethiolate monolayers on gold as a function of the initially populated resonance. In the case of these C2CN monolayers, two nearly-degenerate $[\mathrm{N1s}]\pi^*_{1,2}$ resonances exist, which cannot be separated by simple energetic selection. Therefore, linearly polarized synchrotron radiation was used to selectively populate these two resonance states, which showed significantly different charge transfer times for electron tunneling into the substrate. Faster charge transfer times were obtained for excitation of core electrons into the π^*_1 orbital, despite its lower resonance energy compared to the π^*_2 orbital. Theoretical calculations identified the different extension of the resonances onto the molecular backbone and the anchoring thiol group as the dominant factor responsible for the different electron transfer times. This experiment illustrated the potential of the CHC method as an orbital and symmetry selective probe, as well as the importance of these parameters for ultrafast charge transfer processes.

To further extend the well-established concepts of self-assembled monolayers on coinage metals to ferromagnetic substrates, different types of precursor molecules have been used to prepare SAMs on Ni(111) under UHV conditions in the second set of experiments of this thesis. The first precursor

molecule was 4-fluorothiophenol, which was shown to form a thiolate bond to nickel at temperatures below 200 K. In this state, the molecules form a well-defined monolayer, standing almost upright on the surface and exposing the fluorine tailgroup. Based on this stable configuration, the tailgroup-to-substrate charge transfer was investigated by means of the CHC method. The electron transfer times after resonant F1s excitation were examined and found to lie in the low femtosecond regime, illustrating the good conductivity of the molecule due to its aromatic backbone and the efficient coupling to the substrate. Furthermore, it could be shown that the resonant F1s excitation is accompanied by an ultrafast dissociation process, which results in the desorption of F^+ ions. A major difference to thiolate-bonded SAMs on gold was found after annealing the monolayer to room temperature: S-C bond scission led to the formation of atomic sulfur on the surface and "destroyed" the initially well-defined layer. This effect was understood by considering the higher reactivity of nickel compared to the reasonably inert gold surface and the increased strength of the thiolate-metal bond. Furthermore, some conflicting evidence in prior literature concerning the stability of wet-chemically prepared thiolate-bonded SAMs on nickel could be resolved, and the necessity of high-resolution spectroscopy for investigating these systems could be emphasized.

Motivated by the thermal decomposition for thiolate-coupled SAMs on Ni(111) at room temperature, carboxyl-substituted entities were used as precursor molecules in the subsequent set of experiments in the effort to create SAMs with enhanced thermal stability. 4- and 3-fluorobenzoic acid monolayers on nickel were prepared by sublimation in UHV, resulting in a carboxyl-metal bond and well-defined, upright standing monolayers, similar to 4-FTP. Analogous charge transfer investigations of 4-FBA monolayers resulted in CT times of 18 to 2 fs, and 3 fs for polarization parallel and perpendicular to the surface normal, respectively. These differences were explained by the polarization-dependent population of σ^* or π^* type resonances, which couple differently to the phenyl backbone. Compared to the CT times obtained for 4-FTP under the same excitation conditions, the values for 4-FBA are larger throughout the resonance, which was ascribed to the less effective coupling of the carboxyl group to the substrate. The most striking difference, compared to 4-FTP, is the thermal stability of both 3- and 4-FBA on nickel: Annealing up to temperatures of 380 K does not result in a dissociation of the molecules. Only temperatures above 400 K lead to a stepwise decomposition of the layer, as monitored by fast-XPS and explained by the effect of the different headgroup-substrate interaction. Therefore, 3- and 4-FBA monolayers on Ni(111) are more suitable systems for possible applications in molecular electronics, thanks to their superior stability in comparison to

thiolate-bonded SAMs. Moreover, they also exhibit ultrafast charge transfer; at a price of an only slightly slower charge transfer process compared to thiolate-coupling.

The results obtained for the charge transfer dynamics of 4-FTP and 3- and 4-FBA on Ni(111) raise the question of spin-dependent electron transport from adsorbates to ferromagnetic substrates. This is further motivated by the significance of spin transport within the emerging field of molecular spintronics. Therefore, physisorbed argon on ferromagnetic layers was used as a model system for investigating the spin-dependent adsorbate-to-substrate charge transfer with the core hole clock method in a proof-of-principle experiment. By selectively populating the $[Ar2p_{3/2}]4s$ resonance with minority or majority electrons by means of circularly polarized radiation and by monitoring the decay electrons, spin-dependent electron transport could be observed with resonant photoemission spectroscopy. Minority electrons were found to delocalize about 10% faster than majority electrons for argon adsorbed on Fe(110) and Co(0001), which could be understood by the larger available unoccupied density of states for minority electrons. This also suggested a more efficient coupling of the resonance to empty *d* states, instead of *sp* states. For Ar/Ni(111), no such contrast was observed, which is consistent with the almost equal unoccupied DOS for minority and majority electrons at the resonance energy. Therefore, this experiment proved the capability of the CHC method to accurately resolve spin-dependent differences in charge transfer dynamics.

In conclusion, the toolbox of the core hole clock method could be extended to resolve polarization and spin-dependent differences in charge transfer dynamics with sub-femtosecond precision. Moreover, two systems of self-assembled monolayers were successfully prepared on the reactive nickel substrate and investigated in detail. Future research could apply a slightly altered spin-dependent CHC approach to these monolayers, namely spin-selective *detection* instead of *excitation*, and obtain interesting insight into electron- and spin-transport through molecular entities. Furthermore, the identification of candidate systems for applications in molecular spintronics might become possible.

Appendix A

Partial Electron Yield Detector Appendix

Calculation of White Noise Current of the OP-Amp For OP-Amps of this kind (Dielectrically Isolated FET or DIFET OP-Amps), the input current noise is dominated by the white shot noise of the amplifier's bias current for frequencies below approximately 10 kHz. For higher frequencies that are not relevant here, the noise current increases with frequency (see, e.g. Ref. [204] for the shape of the input current noise spectral density of this OP-Amp type). For the OPA 129 in our design we obtain for the typical bias current of 30 fA [89] a noise current density of $\sqrt{2eI_{bias}} = 1\times10^{-16}\,\mathrm{A}/\sqrt{\mathrm{Hz}}$, i.e. the value given in the datasheet [89]; where e is the elementary charge.

Noise Current Produced by the Capacitance The noise current by this source is the amplifier noise voltage multiplied by the capacitive conductance of C_1+C_2. Up to ∼300 Hz the voltage noise spectral density shows the $f^{-1/2}$ frequency dependence of flicker noise with a value of $85\,\mathrm{nV}/\sqrt{\mathrm{Hz}}$ at 10 Hz corresponding to $270\,\mathrm{nV}/\sqrt{\mathrm{Hz}}$ at 1 Hz (see data on "voltage noise" and "input voltage noise spectral density" in Ref. [89]). In combination with our C_1+C_2 value of 70 pF and averaging from 0 to 10 Hz we obtain for the related current noise spectral density:

$$\frac{2\pi}{10\,\mathrm{Hz}}\cdot\frac{270\,\mathrm{nV}}{\sqrt{\mathrm{Hz}}}\cdot 70\,\mathrm{pF}\int_0^{10\,\mathrm{Hz}}\frac{f}{\sqrt{f}}\mathrm{df} = 2.4\times10^{-16}\,\mathrm{A}/\sqrt{\mathrm{Hz}} \qquad (A.1)$$

Electron Transmission of the Grids The real transmission of the grids in a retarding assembly can deviate from the optical transmission due to secondary electron emission from the grids [205] and due to lens effects by the grid meshes [206], the latter particularly for narrow electron beams as in LEED. This modulation of the transmission function depends on the energy and angular distribution of the decay electrons. Because these quantities are not available without further, very detailed spectroscopic investigations, and because we believe that the error introduced by this modulation

is smaller than the uncertainty of the photon flux (see above), we neglect it.

Noise Coupled in From the Retarding Voltage Supply The capacitance C_2 between retarding grid and collector is 15 pF in our assembly. To keep capacitive pick-up currents at 10 Hz within the same order of magnitude as the amplifier noise, the noise of the retarding voltage should not exceed 1 to 2 μV. For this purpose we use passive RC filters with low cut-off frequencies of 0.1 Hz mounted directly at the electric feedthrough. Batteries as voltage source perform best, but low noise power supplies can also be used.

Appendix B

Determination of Polarization Ratios and Correction of Charge Transfer Times

The measurement geometry together with a schematic sketch of the molecule and the CN $\pi_{1,2}$ orbitals is shown in Figure 4.1 (b). The angle β_{CN} describes the tilt angle of the CN group with respect to the surface normal (z-axis), whereas the angle γ is defined as the twist of the backbone. We employed two polarizations in our experiment, realized by rotating the sample with respect to the incoming radiation. The E vector of the A_{xy} polarization lies in the xy-plane (in fig. 4.1 (b) parallel to the x-axis), the vector of the A_z polarized light lies in the yz-plane and is tilted by 10° with respect to the surface normal. A_z light therefore nearly exclusively excites the π_1 resonance, whereas, due to the random orientation of the substrate domains (different azimuthal angles φ), A_{xy} light has a lower polarization contrast. Since this effect results in a mixture of the measured charge transfer times for both polarizations, we calculated the excitation efficiencies in both geometries and corrected the charge transfer times for this effect. We define the excitation efficiencies S_i (resp. P_i) as the azimuthally integrated, squared dot product of the normalized polarization vector $\vec{E_z}$ ($\vec{E_{xy}}$) and the vector of the $\pi_i(\varphi, \beta_{CN}, \gamma)$ (i=1,2) orbitals:

$$S_i = \int_0^{2\pi} \left(\vec{E_z} \cdot \pi_i(\varphi, \beta_{CN}, \gamma)\right)^2 \mathrm{d}\varphi; \tag{B.1}$$

$$P_i = \int_0^{2\pi} \left(\vec{E_{xy}} \cdot \pi_i(\varphi, \beta_{CN}, \gamma)\right)^2 \mathrm{d}\varphi; \tag{B.2}$$

S_i and P_i are proportional to the respective transition dipole moment (TDM) and therefore a measure of the x-ray absorption efficiency, i.e. S_1 is proportional to the TDM of an excitation into the π_1 orbital with A_z polarized light. The excitation efficiencies are then evaluated with a numerical routine using an azimuthal angular step width of 1° after the tilt and twist angles have been set. Figure B.1 (top) shows the calculated excitation efficiency ratios

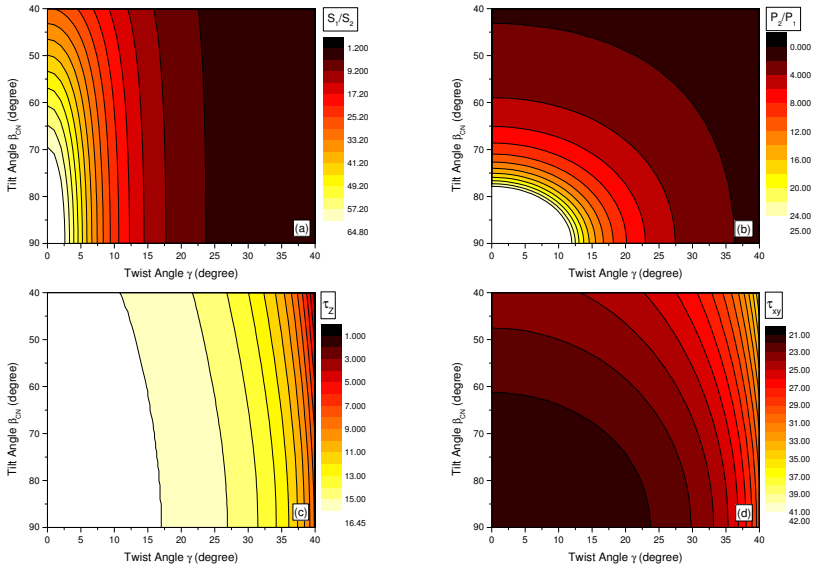

Figure B.1: Excitation efficiency ratios (top) and corrected CT times (bottom) as a function of the tilt and twist angles as calculated with the above mentioned corrections.

S1/S2 (a) and P2/P1 (b) in dependence of the tilt and twist angle. For 60° tilt and 0° twist, we calculate excitation ratios of S1/S2 = 49/1 and P2/P1 = 4/1, which turn into S1/S2 = 2.3/1 and P2/P1 = 1.9/1 for the 60° tilt and 30° twist configuration.

The normalized excitation efficiencies are calculated as:

$$S_i' = \frac{S_i}{S_1 + S_2} \tag{B.3}$$

$$P_i' = \frac{P_i}{P_1 + P_2} \tag{B.4}$$

Due to the different excitation efficiencies, the measured CT times $\hat{\tau}_z$ and $\hat{\tau}_{xy}$ are connected to the "real" values τ_z and τ_{xy} via the following transformation:

$$\begin{pmatrix} \hat{\tau}_z \\ \hat{\tau}_{xy} \end{pmatrix} = \begin{pmatrix} S_1' & S_2' \\ P_1' & P_2' \end{pmatrix} \cdot \begin{pmatrix} \tau_z \\ \tau_{xy} \end{pmatrix} \tag{B.5}$$

Using the inverse of the above transformation, we can then extract the real CT times for given tilt and twist angles. Figure B.1 (bottom) shows the dependence of the calculated corrected CT times τ_z (c) and τ_{xy} (d) on the tilt and twist angle. Employing the experimentally obtained tilt angle of 60° and a reasonable twist angle of 30°, the measured CT times of $\hat{\tau}_z = 16.5\,\text{fs}$ and $\hat{\tau}_{xy} = 21.0\,\text{fs}$ turn into 11.7 fs and 26.0 fs, respectively.

Appendix C

XMCD and XAS Spectra of Ar/Ni,Co,Fe

XMCD Spectra of Thin Ferromagnetic Films Figure C.1 shows the XMCD spectra of the nickel (left), cobalt (middle) and iron (right) thin films prepared on the W(110) substrate. The top panels depict the x-ray absorption intensity as a function of the excitation energy and the magnetization/photon spin alignment, whereas the bottom panels show the difference spectra and illustrate the achieved film magnetization.

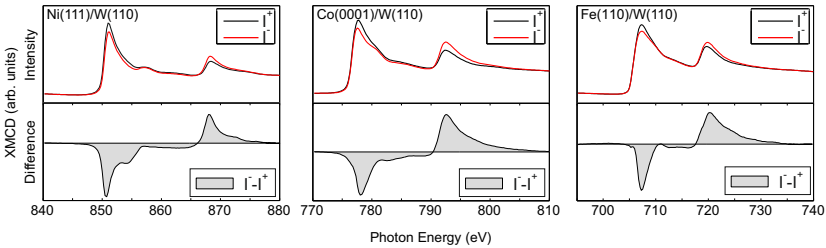

Figure C.1: XMCD spectra of the prepared thin ferromagnetic films. In the top panels, the black (red) line corresponds to the x-ray absorption intensity for parallel (antiparallel) alignment of magnetization direction and photon spin. The difference spectra are shown in the bottom panels. The directions of magnetization and photon helicity are defined according to Ref. [83].

NEXAFS Spectra of Ar[$2p_{3/2}$]4s Resonance Figure C.2 shows the x-ray absorption spectra of the Ar[$2p_{3/2}$]4s resonance for a monolayer of argon adsorbed on an in-plane magnetized cobalt film as a function of the alignment of magnetization direction and photon spin. The procedure for extracting the full width at half maximum (FWHM) of the resonance is also indicated in Figure C.2, as well as the obtained FWHMs of 268 meV and 283 meV for I^+ and I^- excitation, respectively. We note that plotting the spectra on top of

each other would obscure the comparably small difference of 15 meV in the FWHMs.

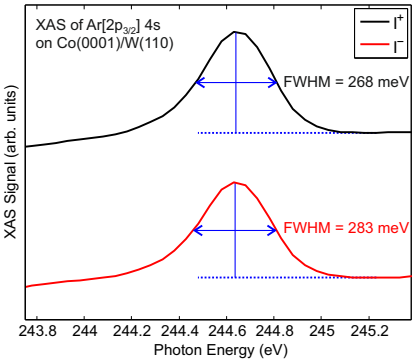

Figure C.2: X-ray absorption spectra of an argon monolayer adsorbed on a thin film of cobalt. Black (red) curve shows the absorption profile for parallel (antiparallel) alignment of magnetization direction and photon spin. The procedure for extracting the full width at half maximum (FWHM) is indicated in the figure.

The same procedure results in values of 312 meV and 331 meV for Ar/Fe with I^+ and I^- excitation, respectively. For Ar/Ni, no absorption spectra with suitable quality for a reliable extraction of the FWHMs have been measured.

List of Publications

1. F. Blobner, R. Han, A. Kim, W. Wurth, and P. Feulner, "Spin-Dependent Electron Transfer Dynamics Probed by Resonant Photoemission Spectroscopy", *to be submitted*, 2013.

2. F. Bischoff, K. Seufert, W. Auwärter, S. Joshi, S. Vijayaraghavan, D. Ecija, K. Diller, A. Papageorgiou, S. Fischer, F. Allegretti, D. Duncan, F. Klappenberger, F. Blobner, R. Han and J.V. Barth, "How surface bonding and repulsive interactions cause phase transformations: ordering of a prototype macrocyclic compound on Ag(111)," *ACS Nano*, http://dx.doi.org/10.1021/nn305487c, 2013

3. R. Flesch, E. Serdaroglu, F. Blobner, P. Feulner, X. O. Brykalova, A. A. Pavlychev, N. Ko- sugi, and E. Ruhl, "Gas-to-solid shift of c 1s-excited benzene," *Phys. Chem. Chem. Phys.*, vol. 14, pp. 9397–9402, 2012.

4. A. C. Papageorgiou, S. Fischer, J. Reichert, K. Diller, F. Blobner, F. Klappenberger, F. Allegretti, A. P. Seitsonen, and J. V. Barth, "Chemical transformations drive complex self-assembly of uracil on close-packed coinage metal surfaces," *ACS Nano*, vol. 6, no. 3, pp. 2477–2486, 2012.

5. F. Blobner, P. B. Coto, F. Allegretti, M. Bockstedte, O. Rubio-Pons, H. Wang, D. L. Allara, M. Zharnikov, M. Thoss, and P. Feulner, "Orbital-symmetry-dependent electron transfer through molecules assembled on metal substrates," *J. Phys. Chem. Lett*, vol. 3, no. 3, pp. 436–440, 2012.

6. F. Blobner, S. Neppl, and P. Feulner, "A versatile partial electron yield detector with large acceptance angle and well-defined threshold energy and gain," *J. Electron Spectrosc. Relat. Phenom.*, vol. 184, no. 8-10, pp. 483–486, 2011.

7. B. Bures, M. Krishnan, R. Madden, and F. Blobner, "Enhancing neutron emission from a 500-J plasma focus by altering the anode geometry and gas composition," *Plasma Science, IEEE Transactions on*, vol. 38, pp. 667–671, 2010.

8. A. Cattani-Scholz, D. Pedone, F. Blobner, G. Abstreiter, J. Schwartz, M. Tornow, and L. Andruzzi, "PNA-PEG modified silicon platforms as functional bio-interfaces for applications in DNA microarrays and biosensors," *Biomacromolecules*, vol. 10, no. 3, pp. 489–496, 2009.

Bibliography

[1] American Physical Society, "November 17 - december 23, 1947: Invention of the first transistor," *APS News*, vol. 9, p. 10, 2000.

[2] B. D. Ratner, "New ideas in biomaterials science: a path to engineered biomaterials," *J. Biomed. Mater. Res.*, vol. 27, no. 7, pp. 837–850, 1993.

[3] D. G. Castner and B. D. Ratner, "Biomedical surface science: Foundations to frontiers," *Surf. Sci.*, vol. 500, no. 13, pp. 28–60, 2002.

[4] S. Gunes, H. Neugebauer, and N. S. Sariciftci, "Conjugated polymer-based organic solar cells," *Chem. Rev.*, vol. 107, no. 4, pp. 1324–1338, 2007.

[5] A. K. Geim and K. S. Novoselov, "The rise of graphene," *Nat. Mater.*, vol. 6, no. 3, pp. 183–191, 2007.

[6] "Intel core i7-3770k processor datasheet." http://ark.intel.com/de/products/65523, 18.03.2013.

[7] J. V. Barth, G. Costantini, and K. Kern, "Engineering atomic and molecular nanostructures at surfaces," *Nature*, vol. 437, no. 7059, pp. 671–679, 2005.

[8] G. Whitesides, J. Mathias, and C. Seto, "Molecular self-assembly and nanochemistry: a chemical strategy for the synthesis of nanostructures," *Science*, vol. 254, no. 5036, pp. 1312–1319, 1991.

[9] P. W. K. Rothemund, "Folding DNA to create nanoscale shapes and patterns," *Nature*, vol. 440, no. 7082, pp. 297–302, 2006.

[10] S. M. Douglas, H. Dietz, T. Liedl, B. Hogberg, F. Graf, and W. M. Shih, "Self-assembly of DNA into nanoscale three-dimensional shapes," *Nature*, vol. 459, no. 7245, pp. 414–418, 2009.

[11] D. P. Woodruff and T. A. Delchar, *Modern Techniques of Surface Science*. Cambridge University Press, 2008.

[12] Y. Feng, W.-K. Teo, K.-S. Siow, Z. Gao, K.-L. Tan, and A.-K. Hsieh, "Corrosion protection of copper by a self-assembled monolayer of alkanethiol," *J. Electrochem. Soc.*, vol. 144, no. 1, pp. 55–64, 1997.

[13] L. Bogani and W. Wernsdorfer, "Molecular spintronics using single-molecule magnets," *Nat. Mater.*, vol. 7, no. 3, pp. 179–186, 2008.

[14] A. Ulman, "Formation and structure of self-assembled monolayers," *Chem. Rev.*, vol. 96, no. 4, pp. 1533–1554, 1996.

[15] F. Schreiber, "Structure and growth of self-assembling monolayers," *Prog. Surf. Sci.*, vol. 65, no. 5-8, pp. 151–256, 2000.

[16] D. K. Schwartz, "Mechanisms and kinetic of self-assembled monolayer formation," *Annu. Rev. Phys. Chem.*, vol. 52, no. 1, pp. 107–137, 2001.

[17] J. C. Love, L. A. Estroff, J. K. Kriebel, R. G. Nuzzo, and G. M. Whitesides, "Self-assembled monolayers of thiolates on metals as a form of nanotechnology," *Chem. Rev.*, vol. 105, no. 4, pp. 1103–1169, 2005.

[18] W. Bigelow, D. Pickett, and W. Zisman, "Oleophobic monolayers: I. films adsorbed from solution in non-polar liquids," *J. Colloid Sci.*, vol. 1, no. 6, pp. 513–538, 1946.

[19] R. G. Nuzzo and D. L. Allara, "Adsorption of bifunctional organic disulfides on gold surfaces," *J. Am. Chem. Soc.*, vol. 105, no. 13, pp. 4481–4483, 1983.

[20] M. D. Porter, T. B. Bright, D. L. Allara, and C. E. D. Chidsey, "Spontaneously organized molecular assemblies. 4. structural characterization of n-alkyl thiol monolayers on gold by optical ellipsometry, infrared spectroscopy, and electrochemistry," *J. Am. Chem. Soc.*, vol. 109, no. 12, pp. 3559–3568, 1987.

[21] T. Ishida, S. Yamamoto, W. Mizutani, M. Motomatsu, H. Tokumoto, H. Hokari, H. Azehara, and M. Fujihira, "Evidence for cleavage of disulfides in the self-assembled monolayer on Au(111)," *Langmuir*, vol. 13, no. 13, pp. 3261–3265, 1997.

[22] F. Tarazona-Vasquez and P. B. Balbuena, "Complexation of the lowest generation poly(amidoamine)-NH_2 dendrimers with metal ions, metal atoms, and Cu(II) hydrates: An ab initio study," *J. Phys. Chem. B*, vol. 108, no. 41, pp. 15992–16001, 2004.

[23] H.-J. Himmel, K. Weiss, B. Jäger, O. Dannenberger, M. Grunze, and C. Wöll, "Ultrahigh vacuum study on the reactivity of organic surfaces terminated by OH and COOH groups prepared by self-assembly of functionalized alkanethiols on Au substrates," *Langmuir*, vol. 13, no. 19, pp. 4943–4947, 1997.

[24] G. M. Whitesides and P. E. Laibinis, "Wet chemical approaches to the characterization of organic surfaces: self-assembled monolayers, wetting, and the physical-organic chemistry of the solid-liquid interface," *Langmuir*, vol. 6, no. 1, pp. 87–96, 1990.

[25] K. Prime and G. Whitesides, "Self-assembled organic monolayers: model systems for studying adsorption of proteins at surfaces.," *Science*, vol. 252, no. 5009, pp. 1164–1167, 1991.

[26] M. Mrksich and G. Whitesides, "Using self-assembled monolayers to understand the interactions of man-made surfaces with proteins and cells.," *Annu. Rev. Biophys. Biomol. Struct.*, vol. 25, pp. 55–78, 1996.

[27] D. M. Alloway, M. Hofmann, D. L. Smith, N. E. Gruhn, A. L. Graham, R. Colorado, V. H. Wysocki, T. R. Lee, P. A. Lee, and N. R. Armstrong, "Interface dipoles arising from self-assembled monolayers on gold: UV photoemission studies of alkanethiols and partially fluorinated alkanethiols," *J. Phys. Chem. B*, vol. 107, no. 42, pp. 11690–11699, 2003.

[28] B. de Boer, A. Hadipour, M. Mandoc, T. van Woudenbergh, and P. Blom, "Tuning of metal work functions with self-assembled monolayers," *Adv. Mater.*, vol. 17, no. 5, pp. 621–625, 2005.

[29] I. H. Campbell, S. Rubin, T. A. Zawodzinski, J. D. Kress, R. L. Martin, D. L. Smith, N. N. Barashkov, and J. P. Ferraris, "Controlling Schottky energy barriers in organic electronic devices using self-assembled monolayers," *Phys. Rev. B*, vol. 54, pp. R14321–R14324, 1996.

[30] S. Kobayashi, T. Nishikawa, T. Takenobu, S. Mori, T. Shimoda, T. Mitani, H. Shimotani, N. Yoshimoto, S. Ogawa, and Y. Iwasa, "Control of carrier density by self-assembled monolayers in organic field-effect transistors," *Nat. Mater.*, vol. 3, no. 5, pp. 317–322, 2004.

[31] G. E. Poirier, "Characterization of organosulfur molecular monolayers on Au(111) using scanning tunneling microscopy," *Chem. Rev.*, vol. 97, no. 4, pp. 1117–1128, 1997.

[32] J. M. Tour, "Molecular electronics. synthesis and testing of components," *Acc. Chem. Res.*, vol. 33, no. 11, pp. 791–804, 2000.

[33] P. Avouris, "Molecular electronics with carbon nanotubes," *Acc. Chem. Res.*, vol. 35, no. 12, pp. 1026–1034, 2002.

[34] A. Salomon, D. Cahen, S. Lindsay, J. Tomfohr, V. Engelkes, and C. Frisbie, "Comparison of electronic transport measurements on organic molecules," *Adv. Mater.*, vol. 15, no. 22, pp. 1881–1890, 2003.

[35] J. Cuevas and E. Scheer, *Molecular Electronics*, vol. 1 of *World Scientific Series in Nanoscience and Nanotechnology*. Singapore: World Scientific, 2010.

[36] A. Aviram and M. A. Ratner, "Molecular rectifiers," *Chem. Phys. Lett.*, vol. 29, no. 2, pp. 277–283, 1974.

[37] H. Haick and D. Cahen, "Making contact: Connecting molecules electrically to the macroscopic world," *Prog. Surf. Sci.*, vol. 83, no. 4, pp. 217–261, 2008.

[38] H. B. Akkerman and B. de Boer, "Electrical conduction through single molecules and self-assembled monolayers," *J. Phys.: Condens. Matter*, vol. 20, no. 1, p. 013001, 2008.

[39] S. Lindsay and M. A. Ratner, "Molecular transport junctions: Clearing mists," *Adv. Mater.*, vol. 19, no. 1, pp. 23–31, 2007.

[40] W. R. French, C. R. Iacovella, I. Rungger, A. M. Souza, S. Sanvito, and P. T. Cummings, "Structural origins of conductance fluctuations in gold-thiolate molecular transport junctions," *J. Phys. Chem. Lett.*, vol. 4, no. 6, pp. 887–891, 2013.

[41] L. Wang, W. Chen, and A. T. S. Wee, "Charge transfer across the molecule/metal interface using the core hole clock technique," *Surf. Sci. Rep.*, vol. 63, no. 11, pp. 465–486, 2008.

[42] C. Joachim and M. A. Ratner, "Molecular electronics: Some views on transport junctions and beyond," *Proc. Natl. Acad. Sci. USA*, vol. 102, no. 25, pp. 8801–8808, 2005.

[43] I. Ron, I. Pecht, M. Sheves, and D. Cahen, "Proteins as solid-state electronic conductors," *Acc. Chem. Res.*, vol. 43, no. 7, pp. 945–953, 2010.

[44] S. Neppl, U. Bauer, D. Menzel, P. Feulner, A. Shaporenko, M. Zharnikov, P. Kao, and D. Allara, "Charge transfer dynamics in self-assembled monomolecular films," *Chem. Phys. Lett.*, vol. 447, no. 4-6, pp. 227–231, 2007.

[45] H. Hamoudi, S. Neppl, P. Kao, B. Schüpbach, P. Feulner, A. Terfort, D. Allara, and M. Zharnikov, "Orbital-dependent charge transfer dynamics in conjugated self-assembled monolayers," *Phys. Rev. Lett.*, vol. 107, p. 027801, 2011.

[46] F. v. Wrochem, F. Scholz, A. Schreiber, H.-G. Nothofer, W. E. Ford, P. Morf, T. Jung, A. Yasuda, and J. M. Wessels, "Structure and conductance of aromatic and aliphatic dithioacetamide monolayers on Au(111)," *Langmuir*, vol. 24, no. 13, pp. 6910–6917, 2008.

[47] I. Žutić, J. Fabian, and S. Das Sarma, "Spintronics: Fundamentals and applications," *Rev. Mod. Phys.*, vol. 76, pp. 323–410, 2004.

[48] S. Wolf, D. Awschalom, R. Buhrman, J. Daughton, S. Von Molnar, M. Roukes, A. Chtchelkanova, and D. Treger, "Spintronics: A spin-based electronics vision for the future," *Science*, vol. 294, no. 5546, p. 1488, 2001.

[49] E. G. Emberly and G. Kirczenow, "Molecular spintronics: Spin-dependent electron transport in molecular wires," *Chem. Phys.*, vol. 281, no. 2-3, pp. 311–324, 2002.

[50] A. R. Rocha, V. M. García-Suárez, S. W. Bailey, C. J. Lambert, J. Ferrer, and S. Sanvito, "Towards molecular spintronics," *Nat. Mater.*, vol. 4, no. 4, pp. 335–339, 2005.

[51] S. Sanvito and A. Rocha, "Molecular-spintronics: The art of driving spin through molecules," *J. Comput. Theor. Nanosci.*, vol. 3, no. 5, pp. 624–642, 2006.

[52] D. Waldron, P. Haney, B. Larade, A. MacDonald, and H. Guo, "Nonlinear spin current and magnetoresistance of molecular tunnel junctions," *Phys. Rev. Lett.*, vol. 96, p. 166804, 2006.

[53] S. Sanvito, "Molecular spintronics," *Chem. Soc. Rev.*, vol. 40, pp. 3336–3355, 2011.

[54] M. Ouyang and D. D. Awschalom, "Coherent spin transfer between molecularly bridged quantum dots," *Science*, vol. 301, no. 5636, pp. 1074–1078, 2003.

[55] J. R. Petta, S. K. Slater, and D. C. Ralph, "Spin-dependent transport in molecular tunnel junctions," *Phys. Rev. Lett.*, vol. 93, p. 136601, 2004.

[56] Z. H. Xiong, D. Wu, Z. Valy Vardeny, and J. Shi, "Giant magnetoresistance in organic spin-valves," *Nature*, vol. 427, no. 6977, pp. 821–824, 2004.

[57] M. Mannini, F. Pineider, P. Sainctavit, C. Danieli, E. Otero, C. Sciancalepore, A. M. Talarico, M.-A. Arrio, A. Cornia, D. Gatteschi, and R. Sessoli, "Magnetic memory of a single-molecule quantum magnet wired to a gold surface," *Nat. Mater.*, vol. 8, no. 3, pp. 194–197, 2009.

[58] "Computational Electronic Structure Database (CompES), National Institute for Materials Science." http://caldb.nims.go.jp/index_en.html, 19.03.2013.

[59] O. Karis, A. Nilsson, M. Weinelt, T. Wiell, C. Puglia, N. Wassdahl, N. Mårtensson, M. Samant, and J. Stöhr, "One-step and two-step description of deexcitation processes in weakly interacting systems," *Phys. Rev. Lett.*, vol. 76, pp. 1380–1383, 1996.

[60] C. Keller, M. Stichler, G. Comelli, F. Esch, S. Lizzit, D. Menzel, and W. Wurth, "Resonant Auger processes in adsorbates," *J. Electron Spectrosc. Relat. Phenom.*, vol. 93, no. 1-3, pp. 135–141, 1998.

[61] C. Keller, M. Stichler, G. Comelli, F. Esch, S. Lizzit, D. Menzel, and W. Wurth, "Femtosecond dynamics of adsorbate charge-transfer processes as probed by high-resolution core-level spectroscopy," *Phys. Rev. B*, vol. 57, pp. 11951–11954, 1998.

[62] W. Wurth and D. Menzel, "Ultrafast electron dynamics at surfaces probed by resonant Auger spectroscopy," *Chem. Phys.*, vol. 251, no. 1-3, pp. 141–149, 2000.

[63] A. Föhlisch, D. Menzel, P. Feulner, M. Ecker, R. Weimar, K. Kostov, G. Tyuliev, S. Lizzit, R. Larciprete, F. Hennies, and W. Wurth, "Energy dependence of resonant charge transfer from adsorbates to metal substrates," *Chem. Phys.*, vol. 289, no. 1, pp. 107–115, 2003.

[64] S. Vijayalakshmi, A. Föhlisch, F. Hennies, A. Pietzsch, M. Nagasono, W. Wurth, A. Borisov, and J. Gauyacq, "Surface projected electronic band structure and adsorbate charge transfer dynamics: Ar adsorbed on Cu(111) and Cu(100)," *Chem. Phys. Lett.*, vol. 427, no. 1-3, pp. 91–95, 2006.

[65] S. Lizzit, G. Zampieri, K. L. Kostov, G. Tyuliev, R. Larciprete, L. Petaccia, B. Naydenov, and D. Menzel, "Charge transfer from core-excited argon adsorbed on clean and hydrogenated Si(100): Ultra-

short timescales and energetic structure," *New J. Phys.*, vol. 11, no. 5, p. 053005, 2009.

[66] D. Sánchez-Portal, D. Menzel, and P. M. Echenique, "First-principles calculation of charge transfer at surfaces: The case of core-excited Ar on Ru(0001)," *Phys. Rev. B*, vol. 76, p. 235406, 2007.

[67] M. P. Seah and W. A. Dench, "Quantitative electron spectroscopy of surfaces: A standard data base for electron inelastic mean free paths in solids," *Surf. Interface Anal.*, vol. 1, no. 1, pp. 2–11, 1979.

[68] S. Hüfner, *Photoelectron Spectroscopy Principles and Applications*. Springer, 2003.

[69] K. Oura, V. Lifshits, A. Saranin, A. Zotov, and M. Katayana, *Surface Science An Introduction*. Springer, 2003.

[70] Y. Park, V. Choong, Y. Gao, B. R. Hsieh, and C. W. Tang, "Work function of indium tin oxide transparent conductor measured by photoelectron spectroscopy," *Appl. Phys. Lett.*, vol. 68, no. 19, pp. 2699–2701, 1996.

[71] G. Wertheim and S. Dicenzo, "Least-squares analysis of photoemission data," *J. Electron Spectrosc. Relat. Phenom.*, vol. 37, no. 1, pp. 57–67, 1985.

[72] D. A. Shirley, "High-resolution x-ray photoemission spectrum of the valence bands of gold," *Phys. Rev. B*, vol. 5, no. 12, pp. 4709–4714, 1972.

[73] G. S. Brown, M. H. Chen, B. Crasemann, and G. E. Ice, "Observation of the Auger resonant Raman effect," *Phys. Rev. Lett.*, vol. 45, pp. 1937–1940, 1980.

[74] P. A. Brühwiler, O. Karis, and N. Mårtensson, "Charge-transfer dynamics studied using resonant core spectroscopies," *Rev. Mod. Phys.*, vol. 74, pp. 703–740, 2002.

[75] J. L. Campbell and T. Papp, "Widths of the atomic K-N7 levels," *Atom. Data Nucl. Data Tables*, vol. 77, no. 1, pp. 1–56, 2001.

[76] M. N. Piancastelli, "Auger resonant raman studies of atoms and molecules," *J. Electron Spectrosc. Relat. Phenom.*, vol. 107, no. 1, pp. 1–26, 2000.

[77] J. Stöhr, *NEXAFS Spectroscopy*. Springer, 2003.

[78] F. Blobner, S. Neppl, and P. Feulner, "A versatile partial electron yield detector with large acceptance angle and well-defined threshold energy and gain," *J. Electron Spectrosc. Relat. Phenom.*, vol. 184, no. 8-10, pp. 483–486, 2011.

[79] M. Krumrey, E. Tegeler, J. Barth, M. Krisch, F. Schäfers, and R. Wolf, "Schottky type photodiodes as detectors in the VUV and soft x-ray range," *Appl. Opt.*, vol. 27, no. 20, pp. 4336–4341, 1988.

[80] J. L. Erskine and E. A. Stern, "Calculation of the M_{23} magneto-optical absorption spectrum of ferromagnetic nickel," *Phys. Rev. B*, vol. 12, pp. 5016–5024, 1975.

[81] G. Schütz, W. Wagner, W. Wilhelm, P. Kienle, R. Zeller, R. Frahm, and G. Materlik, "Absorption of circularly polarized x rays in iron," *Phys. Rev. Lett.*, vol. 58, pp. 737–740, 1987.

[82] J. Stöhr, "Exploring the microscopic origin of magnetic anisotropies with x-ray magnetic circular dichroism (XMCD) spectroscopy," *J. Magn. Magn. Mater.*, vol. 200, no. 13, pp. 470–497, 1999.

[83] J. Stöhr and H. C. Siegmann, *Magnetism: From Fundamentals to Nanoscale Dynamics*, vol. 152. Springer, 2006.

[84] P. Carra, B. T. Thole, M. Altarelli, and X. Wang, "X-ray circular dichroism and local magnetic fields," *Phys. Rev. Lett.*, vol. 70, pp. 694–697, 1993.

[85] B. T. Thole, P. Carra, F. Sette, and G. van der Laan, "X-ray circular dichroism as a probe of orbital magnetization," *Phys. Rev. Lett.*, vol. 68, pp. 1943–1946, 1992.

[86] R. Romberg, *Photochemie von Kondensaten und Chemiesorbaten nach Innerschalen-Anregungen.* PhD thesis, Technische Universität München, 2001.

[87] M. O. Krause, "Atomic radiative and radiationless yields for K and L shells," *J. Phys. Chem. Ref. Data*, vol. 8, no. 2, pp. 307–327, 1979.

[88] E. Umbach and Z. Hussain, "Angle-dependent changes of Auger line shapes from adsorbed molecules," *Phys. Rev. Lett.*, vol. 52, pp. 457–460, 1984.

[89] "OP-Amp datasheet OPA129, ultra-low bias current difet operational amplifier." http://focus.ti.com/lit/ds/symlink/opa129.pdf, 01.05.2011.

[90] E. D. Williams and W. Weinberg, "The geometric structure of carbon monoxide chemisorbed on the ruthenium (001) surface at low temperatures," *Surf. Sci.*, vol. 82, no. 1, pp. 93–101, 1979.

[91] A. Hitchcock and C. Brion, "K-shell excitation spectra of CO, N_2 and O_2," *J. Electron Spectrosc. Relat. Phenom.*, vol. 18, no. 1, pp. 1–21, 1980.

[92] A. Hitchcock, "Bibliography of atomic and molecular inner-shell excitation studies," *J. Electron Spectrosc. Relat. Phenom.*, vol. 67, no. 1, pp. 1–132, 1994.

[93] A. Föhlisch, M. Nyberg, P. Bennich, L. Triguero, J. Hasselström, O. Karis, L. G. M. Pettersson, and A. Nilsson, "The bonding of CO to metal surfaces," *J. Chem. Phys.*, vol. 112, no. 4, pp. 1946–1958, 2000.

[94] F. Blobner, P. B. Coto, F. Allegretti, M. Bockstedte, O. Rubio-Pons, H. Wang, D. L. Allara, M. Zharnikov, M. Thoss, and P. Feulner, "Orbital-symmetry-dependent electron transfer through molecules assembled on metal substrates," *J. Phys. Chem. Lett*, vol. 3, no. 3, pp. 436–440, 2012.

[95] S. I. Weissman, "Intramolecular electron exchange in anions of paracyclophanes," *J. Am. Chem. Soc.*, vol. 80, no. 23, pp. 6462–6463, 1958.

[96] V. Voevodskij, S. Solodovnikov, and V. Chibrikin *Doklady Akad. Nauk S.S.S.R.*, vol. 129, p. 1082, 1959.

[97] H. McConnell, "Intramolecular charge transfer in aromatic free radicals," *J. Chem. Phys.*, vol. 35, no. 2, pp. 508–515, 1961.

[98] R. Marcus and N. Sutin, "Electron transfer in chemistry and biology," *Biochim. Biophys. Acta*, vol. 811, no. 3, pp. 265–322, 1985.

[99] M. Bixon and J. Jortner, *Electron Transfer - From Isolated Molecules to Biomolecules*, pp. 35–202. John Wiley & Sons, Inc., 2007.

[100] P. Barbara, T. Meyer, and M. Ratner, "Contemporary issues in electron transfer research," *J. Phys. Chem.*, vol. 100, no. 31, pp. 13148–13168, 1996.

[101] N. Itoh and A. M. Stoneham, *Materials Modification by Electronic Excitation*. Cambridge University Press, 2001.

[102] M. Zharnikov, S. Frey, K. Heister, and M. Grunze, "Modification of alkanethiolate monolayers by low energy electron irradiation: Dependence on the substrate material and on the length and isotopic composition of the alkyl chains," *Langmuir*, vol. 16, no. 6, pp. 2697–2705, 2000.

[103] D. B. Williams and C. B. Carter, "The transmission electron microscope," in *Transmission Electron Microscopy*, pp. 3–22, Springer US, 2009.

[104] W. R. Duncan and O. V. Prezhdo, "Theoretical studies of photoinduced electron transfer in dye-sensitized TiO2," *Annu. Rev. Phys. Chem.*, vol. 58, no. 1, pp. 143–184, 2007.

[105] A. Hagfeldt, G. Boschloo, L. Sun, L. Kloo, and H. Pettersson, "Dye-sensitized solar cells," *Chem. Rev.*, vol. 110, no. 11, pp. 6595–6663, 2010.

[106] D. Secker, S. Wagner, S. Ballmann, R. Hartle, M. Thoss, and H. B. Weber, "Resonant vibrations, peak broadening, and noise in single molecule contacts: The nature of the first conductance peak," *Phys. Rev. Lett.*, vol. 106, no. 13, 2011.

[107] M. Tsutsui, M. Taniguchi, and T. Kawai, "Single-molecule identification via electric current noise," *Nat. Commun.*, vol. 1, p. 138, 2010.

[108] O. Björneholm, A. Nilsson, A. Sandell, B. Hernnäs, and N. Mårtensson, "Determination of time scales for charge transfer screening in physisorbed molecules," *Phys. Rev. Lett.*, vol. 68, no. 12, pp. 1892–1895, 1992.

[109] D. Menzel, "Ultrafast charge transfer at surfaces accessed by core electron spectroscopies," *Chem. Soc. Rev.*, vol. 37, no. 10, pp. 2212–2223, 2008.

[110] P. Kao, S. Neppl, P. Feulner, D. L. Allara, and M. Zharnikov, "Charge transfer time in alkanethiolate self-assembled monolayers via resonant auger electron spectroscopy," *J. Phys. Chem. C*, vol. 114, no. 32, pp. 13766–13773, 2010.

[111] N. Ballav, B. Schüpbach, S. Neppl, P. Feulner, A. Terfort, and M. Zharnikov, "Biphenylnitrile-based self-assembled monolayers on Au(111): Spectroscopic characterization and resonant excitation of the nitrile tail group," *J. Chem. Phys. C*, vol. 114, no. 29, pp. 12719–12727, 2010.

[112] M. Deppe, A. Föhlisch, F. Hennies, M. Nagasono, M. Beye, D. Sanchez-Portal, P. M. Echenique, and W. Wurth, "Ultrafast charge transfer and atomic orbital polarization," *J. Chem. Phys.*, vol. 127, no. 17, p. 174708, 2007.

[113] S. Frey, A. Shaporenko, M. Zharnikov, P. Harder, and D. L. Allara, "Self-assembled monolayers of nitrile-functionalized alkanethiols on gold and silver substrates," *J. Phys. Chem. C*, vol. 107, no. 31, pp. 7716–7725, 2003.

[114] B. Kempgens, A. Kivimäki, M. Neeb, H. M. Köppe, A. M. Bradshaw, and J. Feldhaus, "A high-resolution N1s photoionization study of the N_2 molecule in the near-threshold region," *J. Phys. B: At., Mol. Opt. Phys.*, vol. 29, no. 22, p. 5389, 1996.

[115] I. Kondov, M. Cizek, C. Benesch, H. Wang, and M. Thoss, "Quantum dynamics of photoinduced electron-transfer reactions in dye-semiconductor systems: First-principles description and application to coumarin 343-TiO_2," *J. Phys. Chem. C*, vol. 111, no. 32, pp. 11970–11981, 2007.

[116] J. Li, M. Nilsing, I. Kondov, H. Wang, P. Persson, S. Lunell, and M. Thoss, "Dynamical simulation of photoinduced electron transfer reactions in dye-semiconductor systems with different anchor groups," *J. Phys. Chem. C*, vol. 112, no. 32, pp. 12326–12333, 2008.

[117] J. Li, I. Kondov, H. Wang, and M. Thoss, "Theoretical study of photoinduced electron-transfer processes in the dye-semiconductor system alizarin-TiO_2," *J. Phys. Chem. C*, vol. 114, no. 43, pp. 18481–18493, 2010.

[118] J. McMurry, *Fundamentals of organic chemistry*. Thomson Brooks/Cole, 2010.

[119] H. H. Law, J. Sapjeta, C. E. D. Chidsey, and T. M. Putvinski, "Protective treatments for nickel-based contact materials," *J. Electrochem. Soc.*, vol. 141, no. 7, pp. 1977–1982, 1994.

[120] A. D. Vogt, T. Han, and T. P. Beebe, "Adsorption of 11-mercaptoundecanoic acid on Ni(111) and its interaction with probe molecules," *Langmuir*, vol. 13, no. 13, pp. 3397–3403, 1997.

[121] Z. Mekhalif, J. Riga, J. Pireaux, and J. Delhalle, "Self-assembled monolayers of n-dodecanethiol on electrochemically modified polycrystalline nickel surfaces," *Langmuir*, vol. 13, no. 8, pp. 2285–2290, 1997.

[122] Z. Mekhalif, J. Delhalle, J.-J. Pireaux, S. Noell, F. Houze, and L. Boyer, "Surface modifications of nickel substrates with self-assembled monolayers of alkanethiols for electrical contact applications," *Surf. Coat. Technol.*, vol. 100-101, pp. 463–468, 1998.

[123] M. Neuber, M. Zharnikov, J. Walz, and M. Grunze, "The adsorption geometry of benzoic acid on Ni(110)," *Surf. Rev. Lett.*, vol. 6, no. 1, pp. 53–75, 1999.

[124] S. Noel, F. Houze, L. Boyer, Z. Mekhalif, J. Delhalle, and R. Caudano, "Self-assembled monolayers of alkanethiols on nickel surfaces for low level electrical contact applications," *IEEE Trans. Comp. Packag. Technol.*, vol. 22, no. 1, pp. 79–84, 1999.

[125] Z. Mekhalif, F. Laffineur, N. Couturier, and J. Delhalle, "Elaboration of self-assembled monolayers of n-alkanethiols on nickel polycrystalline substrates: Time, concentration, and solvent effects," *Langmuir*, vol. 19, no. 3, pp. 637–645, 2003.

[126] S. Bengió, M. Fonticelli, G. Benítez, A. H. Creus, P. Carro, H. Ascolani, G. Zampieri, B. Blum, and R. C. Salvarezza, "Electrochemical self-assembly of alkanethiolate molecules on Ni(111) and polycrystalline Ni surfaces," *J. Phys. Chem. B*, vol. 109, no. 49, pp. 23450–23460, 2005.

[127] L. Tortech, Z. Mekhalif, J. Delhalle, F. Guittard, and S. Garibaldi, "Self-assembled monolayers of semifluorinated thiols on electrochemically modified polycrystalline nickel surfaces," *Thin Solid Films*, vol. 491, no. 12, pp. 253–259, 2005.

[128] P. G. Hoertz, J. R. Niskala, P. Dai, H. T. Black, and W. You, "Comprehensive investigation of self-assembled monolayer formation on ferromagnetic thin film surfaces," *J. Am. Chem. Soc.*, vol. 130, no. 30, pp. 9763–9772, 2008.

[129] Y. Takata, T. Yokoyama, S. Yagi, N. Happo, H. Sato, K. Seki, T. Ohta, Y. Kitajima, and H. Kuroda, "Thiophenol adsorption on Ni(100) studied by S K-edge SEXAFS and XANES," *Surf. Sci.*, vol. 259, no. 3, pp. 266–274, 1991.

[130] D. R. Huntley, "The mechanism of the desulfurization of benzenethiol by nickel (110)," *J. Phys. Chem.*, vol. 96, no. 11, pp. 4550–4558, 1992.

[131] T. S. Rufael, D. R. Huntley, D. R. Mullins, and J. L. Gland, "Adsorption and reactions of benzenethiol on the Ni(111) surface," *J. Phys. Chem.*, vol. 98, no. 49, pp. 13022–13027, 1994.

[132] T. S. Rufael, D. R. Huntley, D. R. Mullins, and J. L. Gland, "Adsorption and reaction of dimethyl disulfide on the Ni(111) surface," *J. Phys. Chem. B*, vol. 102, no. 18, pp. 3431–3440, 1998.

[133] R. Musket, W. McLean, C. Colmenares, D. Makowiecki, and W. Siekhaus, "Preparation of atomically clean surfaces of selected elements: A review," *Applications of Surface Science*, vol. 10, no. 2, pp. 143–207, 1982.

[134] M. Konôpka, R. Rousseau, I. Štich, and D. Marx, "Electronic origin of disorder and diffusion at a molecule-metal interface: Self-assembled monolayers of CH_3S on Cu(111)," *Phys. Rev. Lett.*, vol. 95, p. 096102, 2005.

[135] M. Konôpka, R. Rousseau, I. Štich, and D. Marx, "Detaching thiolates from copper and gold clusters: Which bonds to break?," *J. Am. Chem. Soc.*, vol. 126, no. 38, pp. 12103–12111, 2004.

[136] S. M. Kane, D. R. Huntley, and J. L. Gland, "Benzenethiol reaction on the clean and hydrogen pretreated Ni(100) surface," *J. Phys. Chem. B*, vol. 102, no. 50, pp. 10216–10222, 1998.

[137] S. M. Kane, D. R. Huntley, and J. L. Gland, "Toluene formation from coadsorbed methanethiol and benzenethiol on nickel surfaces," *J. Phys. Chem. B*, vol. 105, no. 39, pp. 9548–9556, 2001.

[138] C. M. Whelan, C. J. Barnes, C. G. Walker, and N. M. Brown, "Benzenethiol adsorption on Au(111) studied by synchrotron ARUPS, HREELS and XPS," *Surf. Sci.*, vol. 425, no. 23, pp. 195–211, 1999.

[139] L.-J. Wan, M. Terashima, H. Noda, and M. Osawa, "Molecular orientation and ordered structure of benzenethiol adsorbed on gold(111)," *J. Phys. Chem. B*, vol. 104, no. 15, pp. 3563–3569, 2000.

[140] C. Schmidt, A. Witt, and G. Witte, "Tailoring the Cu(100) work function by substituted benzenethiolate self-assembled monolayers," *J. Phys. Chem. A*, vol. 115, no. 25, pp. 7234–7241, 2011.

[141] N. Ballav, B. Schüpbach, O. Dethloff, P. Feulner, A. Terfort, and M. Zharnikov, "Direct probing molecular twist and tilt in aromatic self-assembled monolayers," *J. Am. Chem. Soc.*, vol. 129, no. 50, pp. 15416–15417, 2007.

[142] L. Wang, L. Liu, W. Chen, Y. Feng, and A. T. S. Wee, "Configuration-dependent interface charge transfer at a molecule-metal junction," *J. Am. Chem. Soc.*, vol. 128, no. 24, pp. 8003–8007, 2006.

[143] W. Chen and A. T. S. Wee, "Synchrotron PES and NEXAFS studies of self-assembled aromatic thiol monolayers on Au(111)," *J. Electron Spectrosc. Relat. Phenom.*, vol. 172, no. 1-3, pp. 54–63, 2009.

[144] K. L. Wong, X. Lin, K.-Y. Kwon, G. Pawin, B. V. Rao, A. Liu, L. Bartels, S. Stolbov, and T. S. Rahman, "Halogen-substituted thiophenol molecules on Cu(111)," *Langmuir*, vol. 20, no. 25, pp. 10928–10934, 2004.

[145] D. G. Castner, K. Hinds, and D. W. Grainger, "X-ray photoelectron spectroscopy sulfur 2p study of organic thiol and disulfide binding interactions with gold surfaces," *Langmuir*, vol. 12, no. 21, pp. 5083–5086, 1996.

[146] D. G. de Oteyza, A. Sakko, A. El-Sayed, E. Goiri, L. Floreano, A. Cossaro, J. M. Garcia-Lastra, A. Rubio, and J. E. Ortega, "Inversed linear dichroism in F K-edge NEXAFS spectra of fluorinated planar aromatic molecules," *Phys. Rev. B*, vol. 86, p. 075469, 2012.

[147] A. P. Hitchcock, P. Fischer, A. Gedanken, and M. B. Robin, "Antibonding sigma valence MOs in the inner-shell and outer-shell spectra of the fluorobenzenes," *J. Phys. Chem.*, vol. 91, no. 3, pp. 531–540, 1987.

[148] O. Plashkevych, L. Yang, O. Vahtras, H. Agren, and L. G. Petterson, "Substituted benzenes as building blocks in near-edge x-ray absorption spectra," *Chem. Phys.*, vol. 222, no. 2-3, pp. 125–137, 1997.

[149] B. Sexton and A. Hughes, "A comparison of weak molecular adsorption of organic molecules on clean copper and platinum surfaces," *Surf. Sci.*, vol. 140, no. 1, pp. 227–248, 1984.

[150] P. E. Laibinis, G. M. Whitesides, D. L. Allara, Y. T. Tao, A. N. Parikh, and R. G. Nuzzo, "Comparison of the structures and wetting properties of self-assembled monolayers of n-alkanethiols on the coinage metal surfaces, copper, silver, and gold," *J. Am. Chem. Soc.*, vol. 113, no. 19, pp. 7152–7167, 1991.

[151] D. Mullins, D. Huntley, and S. Overbury, "The nature of the sulfur induced surface reconstruction on Ni(111)," *Surf. Sci.*, vol. 323, no. 1-2, pp. L287 – L292, 1995.

[152] T. Ishida, M. Hara, I. Kojima, S. Tsuneda, N. Nishida, H. Sasabe, and W. Knoll, "High resolution x-ray photoelectron spectroscopy measurements of octadecanethiol self-assembled monolayers on Au(111)," *Langmuir*, vol. 14, no. 8, pp. 2092–2096, 1998.

[153] H. Takiguchi, K. Sato, T. Ishida, K. Abe, K. Yase, and K. Tamada, "Delicate surface reaction of dialkyl sulfide self-assembled monolayers on Au(111)," *Langmuir*, vol. 16, no. 4, pp. 1703–1710, 2000.

[154] K. Heister, H.-T. Rong, M. Buck, M. Zharnikov, M. Grunze, and L. S. O. Johansson, "Odd-even effects at the S-metal interface and in the aromatic matrix of biphenyl-substituted alkanethiol self-assembled monolayers," *J. Phys. Chem. B*, vol. 105, no. 29, pp. 6888–6894, 2001.

[155] C. L. A. Lamont and J. Wilkes, "Attenuation length of electrons in self-assembled monolayers of n-alkanethiols on gold," *Langmuir*, vol. 15, no. 6, pp. 2037–2042, 1999.

[156] S. Tanuma, C. J. Powell, and D. R. Penn, "Calculations of electron inelastic mean free paths. V. data for 14 organic compounds over the 50-2000 eV range," *Surf. Interface Anal.*, vol. 21, no. 3, pp. 165–176, 1994.

[157] F. Blobner, P. Abufager, F. Allegretti, R. Han, J. Bauer, H. F. Busnengo, K. Reuter, and P. Feulner, "in preparation," 2013.

[158] H. B. Michaelson, "The work function of the elements and its periodicity," *J. Appl. Phys.*, vol. 48, no. 11, pp. 4729–4733, 1977.

[159] S.-Y. Hong, P.-C. Yeh, J. I. Dadap, and R. M. Osgood, "Interfacial dipole formation and surface-electron confinement in low-coverage self-assembled thiol layers: Thiophenol and p-fluorothiophenol on Cu(111)," *ACS Nano*, vol. 6, no. 12, pp. 10622–10631, 2012.

[160] L. Romaner, G. Heimel, and E. Zojer, "Electronic structure of thiol-bonded self-assembled monolayers: Impact of coverage," *Phys. Rev. B*, vol. 77, p. 045113, 2008.

[161] A. Natan, L. Kronik, H. Haick, and R. T. Tung, "Electrostatic properties of ideal and non-ideal polar organic monolayers: Implications for electronic devices," *Adv. Mater.*, vol. 19, no. 23, pp. 4103–4117, 2007.

[162] E. Delamarche, B. Michel, H. Kang, and C. Gerber, "Thermal stability of self-assembled monolayers," *Langmuir*, vol. 10, no. 11, pp. 4103–4108, 1994.

[163] G. Held, J. Schuler, W. Sklarek, and H.-P. Steinrück, "Determination of adsorption sites of pure and coadsorbed CO on Ni(111) by high resolution x-ray photoelectron spectroscopy," *Surf. Sci.*, vol. 398, no. 1-2, pp. 154–171, 1998.

[164] M. Weinelt, N. Wassdahl, T. Wiell, O. Karis, J. Hasselström, P. Bennich, A. Nilsson, J. Stöhr, and M. Samant, "Electronic structure of benzene on Ni(100) and Cu(110): An x-ray-spectroscopy study," *Phys. Rev. B*, vol. 58, pp. 7351–7360, 1998.

[165] A. Klekamp and E. Umbach, "Photon-induced dissociation of physisorbed SF_6 on Ni(111)," *Chem. Phys. Lett.*, vol. 171, no. 3, pp. 233–238, 1990.

[166] T. S. Rufael, D. R. Huntley, D. R. Mullins, and J. L. Gland, "Methyl thiolate on Ni(111): Multiple adsorption sites and mechanistic implications," *J. Phys. Chem.*, vol. 99, no. 29, pp. 11472–11480, 1995.

[167] P. Morin and I. Nenner, "Atomic autoionization following very fast dissociation of core-excited HBr," *Phys. Rev. Lett.*, vol. 56, pp. 1913–1916, 1986.

[168] F. Gelmukhanov and H. Ågren, "X-ray resonant scattering involving dissociative states," *Phys. Rev. A*, vol. 54, pp. 379–393, 1996.

[169] E. Pahl, L. S. Cederbaum, H.-D. Meyer, and F. Tarantelli, "Controlled interplay between decay and fragmentation in resonant auger processes," *Phys. Rev. Lett.*, vol. 80, pp. 1865–1868, 1998.

[170] E. Kukk, H. Aksela, S. Aksela, F. Gel'mukhanov, H. Ågren, and S. Svensson, "Raman versus non- Raman behavior in resonant auger spectra of HCl," *Phys. Rev. Lett.*, vol. 76, pp. 3100–3103, 1996.

[171] P. Salek, V. Carravetta, F. Gel'mukhanov, H. Agren, B. Schimmelpfennig, M.-N. Piancastelli, L. Sorensen, R. Feifel, I. Hjelte, M. Bässler, S. Svensson, O. Björneholm, and A. N. de Brito, "Dynamical suppression of atomic peaks in resonant dissociative photoemission," *Chem. Phys. Lett.*, vol. 343, no. 3-4, pp. 332–338, 2001.

[172] O. Travnikova, J.-C. Liu, A. Lindblad, C. Nicolas, J. Söderström, V. Kimberg, F. Gel'mukhanov, and C. Miron, "Circularly polarized x rays: Another probe of ultrafast molecular decay dynamics," *Phys. Rev. Lett.*, vol. 105, p. 233001, 2010.

[173] K. Wiesner, A. N. de Brito, S. Sorensen, F. Burmeister, M. Gisselbrecht, S. Svensson, and O. Björneholm, "The dynamic Auger-Doppler effect in HF and DF: control of fragment velocities in femtosecond dissociation through photon energy detuning," *Chem. Phys. Lett.*, vol. 354, no. 5-6, pp. 382–388, 2002.

[174] J. Fuggle, C. Brundle, and A. Baker, "Electron spectroscopy," *Academic, London*, p. 85, 1981.

[175] W. Erley and D. Sander, "The adsorption and decomposition of formic acid on Ni(111): The identification of formic anhydride by vibrational spectroscopy," *J. Vac. Sci. Technol. A*, vol. 7, no. 3, pp. 2238–2244, 1989.

[176] A. Bandara, J. Kubota, A. Wada, K. Domen, and C. Hirose, "Adsorption and decomposition of formic acid (DCOOD) on NiO(111) and Ni(111) surfaces probed by SFG," *Appl. Phys. B*, vol. 68, pp. 573–578, 1999.

[177] B. Frederick, T. Jones, P. Pudney, and N. Richardson, "HREELS and RAIRS: A complete vibrational study of the surface benzoate species adsorbed on copper," *J. Electron Spectrosc. Relat. Phenom.*, vol. 64-65, pp. 115–122, 1993.

[178] B. Frederick, M. Ashton, N. Richardson, and T. Jones, "Orientation and bonding of benzoic acid, phthalic anhydride and pyromellitic dianhydride on Cu(110)," *Surf. Sci.*, vol. 292, no. 1-2, pp. 33–46, 1993.

[179] L. H. Dubois, B. R. Zegarski, and R. G. Nuzzo, "Spontaneous organization of carboxylic acid monolayer films in ultrahigh vacuum. kinetic constraints to assembly via gas-phase adsorption," *Langmuir*, vol. 2, no. 4, pp. 412–417, 1986.

[180] S. Stepanow, T. Strunskus, M. Lingenfelder, A. Dmitriev, H. Spillmann, N. Lin, J. V. Barth, C. Wöll, and K. Kern, "Deprotonation-driven phase transformations in terephthalic acid self-assembly on Cu(100)," *J. Phys. Chem. B*, vol. 108, no. 50, pp. 19392–19397, 2004.

[181] Y. Tan, M. Srinivasan, S. Pehkonen, and S. Y. Chooi, "Effects of ring substituents on the protective properties of self-assembled benzenethiols on copper," *Corros. Sci.*, vol. 48, no. 4, pp. 840–862, 2006.

[182] T. Bitzer, N. Richardson, S. Reiss, M. Wühn, and C. Wöll, "Sodium-induced ordering of the benzoate species on Si(100)-2x1: a combined HREELS, XPS and NEXAFS study," *Surf. Sci.*, vol. 458, no. 1-3, pp. 173–184, 2000.

[183] U. Hergenhahn, A. Rädel, K. Maier, A. Bradshaw, R. Fink, and A. Wen, "The resonant auger spectra of formic acid, acetaldehyde, acetic acid and methyl formate," *Chem. Phys.*, vol. 289, no. 1, pp. 57–67, 2003.

[184] P. Norton, R. Tapping, and J. Goodale, "A photoemission study of the interaction of Ni(100), (110) and (111) surfaces with oxygen," *Surf. Sci.*, vol. 65, no. 1, pp. 13–36, 1977.

[185] H.-P. Steinrück, W. Huber, T. Pache, and D. Menzel, "The adsorption of benzene mono- and multilayers on Ni(111) studied by TPD and LEED," *Surf. Sci.*, vol. 218, no. 2-3, pp. 293–316, 1989.

[186] T. Nakayama, K. Inamura, Y. Inoue, S. Ikeda, and K. Kishi, "Adsorption of benzonitrile and alkyl cyanides on evaporated nickel and palladium films studied by XPS," *Surf. Sci.*, vol. 179, no. 1, pp. 47–58, 1987.

[187] F. Blobner, "Adsorbat-Substrat-Ladungstransferdynamik von atomaren Phosphorschichten auf Metalloberflächen," Master's thesis, Technische Universität München, 2008.

[188] M. M. Sung, K. Sung, C. G. Kim, S. S. Lee, and Y. Kim, "Self-assembled monolayers of alkanethiols on oxidized copper surfaces," *J. Phys. Chem. B*, vol. 104, no. 10, pp. 2273–2277, 2000.

[189] F. Chen, X. Li, J. Hihath, Z. Huang, and N. Tao, "Effect of anchoring groups on single-molecule conductance: Comparative study of thiol-, amine-, and carboxylic-acid-terminated molecules," *J. Am. Chem. Soc.*, vol. 128, no. 49, pp. 15874–15881, 2006.

[190] F. Blobner, R. Han, A. Kim, W. Wurth, and P. Feulner, "Spin-dependent electron transfer dynamics probed by resonant photoemission spectroscopy," *to be submitted*, 2013.

[191] M. F. Kling, C. Siedschlag, A. J. Verhoef, J. I. Khan, M. Schultze, T. Uphues, Y. Ni, M. Uiberacker, M. Drescher, F. Krausz, and M. J. J. Vrakking, "Control of electron localization in molecular dissociation," *Science*, vol. 312, no. 5771, pp. 246–248, 2006.

[192] F. Stellacci, C. A. Bauer, T. Meyer-Friedrichsen, W. Wenseleers, V. Alain, S. M. Kuebler, S. J. Pond, Y. Zhang, S. R. Marder, and J. W. Perry, "Laser and electron-beam induced growth of nanoparticles for 2D and 3D metal patterning," *Adv. Mater.*, vol. 14, no. 3, p. 194, 2002.

[193] D. Menzel, "Desorption induced by electronic transitions: Some recent progress," *Nuclear Instruments and Methods in Physics Research Section B: Beam Interactions with Materials and Atoms*, vol. 13, no. 1-3, pp. 507–517, 1986.

[194] P. Avouris and R. E. Walkup, "Fundamental mechanisms of desorption and fragmentation induced by electronic-transitions at surfaces," *Annu. Rev. Phys. Chem.*, vol. 40, pp. 173–206, 1989.

[195] X. Lou, C. Adelmann, S. A. Crooker, E. S. Garlid, J. Zhang, K. S. M. Reddy, S. D. Flexner, C. J. Palmstrom, and P. A. Crowell, "Electrical detection of spin transport in lateral ferromagnet-semiconductor devices," *Nat. Phys.*, vol. 3, no. 3, pp. 197–202, 2007.

[196] R. D. Muiño, D. Sánchez-Portal, V. M. Silkin, E. V. Chulkov, and P. M. Echenique, "Time-dependent electron phenomena at surfaces," *Proc. Natl. Acad. Sci. USA*, vol. 108, no. 3, pp. 971–976, 2011.

[197] W. Wurth, G. Rocker, P. Feulner, R. Scheuerer, L. Zhu, and D. Menzel, "Core excitation and deexcitation in argon multilayers: Surface- and bulk-specific transitions and autoionization versus auger decay," *Phys. Rev. B*, vol. 47, pp. 6697–6704, 1993.

[198] U. Gradmann and G. Waller, "Periodic lattice distortions in epitaxial films of Fe(110) on W(110)," *Surf. Sci.*, vol. 116, no. 3, pp. 539–548, 1982.

[199] Y. Li and K. Baberschke, "Dimensional crossover in ultrathin Ni(111) films on W(110)," *Phys. Rev. Lett.*, vol. 68, pp. 1208–1211, 1992.

[200] H. Pinkvos, H. Poppa, E. Bauer, and J. Hurst, "Spin-polarized low-energy electron microscopy study of the magnetic microstructure of ultra-thin epitaxial cobalt films on W(110)," *Ultramicroscopy*, vol. 47, no. 4, pp. 339–345, 1992.

[201] D. T. Pierce and F. Meier, "Photoemission of spin-polarized electrons from GaAs," *Phys. Rev. B*, vol. 13, pp. 5484–5500, 1976.

[202] C. T. Chen, Y. U. Idzerda, H.-J. Lin, N. V. Smith, G. Meigs, E. Chaban, G. H. Ho, E. Pellegrin, and F. Sette, "Experimental confirmation of the x-ray magnetic circular dichroism sum rules for iron and cobalt," *Phys. Rev. Lett.*, vol. 75, pp. 152–155, Jul 1995.

[203] J. V. Ortiz, "Qualitative propagator theory of CH_3CN, CH_3NC, and CH_3CCH auger spectra," *J. Chem. Phys.*, vol. 83, no. 9, pp. 4604–4617, 1985.

[204] "OP-Amp datasheet OPA111, low noise precision difet operational amplifier." http://focus.ti.com/lit/ds/symlink/opa111.pdf, 01.05.2011.

[205] P. S. P. Wei, A. Y. Cho, and C. W. Caldwell, "Instrumental effects of the retarding grids in a LEED apparatus," *Rev. Sci. Instrum.*, vol. 40, no. 8, pp. 1075–1079, 1969.

[206] N. R. Avery, "Instrumental effects in the electron loss spectra from surfaces due to the use of LEED optics," *J. Phys. E: Sci. Instrum.*, vol. 9, no. 8, p. 676, 1976.

Acknowledgments

First of all, I would like to thank my supervisor, Prof. Peter Feulner for giving me the opportunity to spend my last years at E20 for my PhD research. During this time, I greatly benefited from his vast experience, both experimentally and theoretically, as well as from his open-mindedness. His presence during the many synchrotron beamtimes was always of great help in combination with providing a perfect working atmosphere. Furthermore, I would like to thank the following people, who all contributed directly or indirectly to the success of this work:

Prof. Johannes Barth, for providing the PhD position at E20.
Dr. Francesco Allegretti, for being a great colleague whose door was always open for me and for the important support during the beamtimes and in the lab, as well as for distraction during the various tennis matches
Dr. Paula Abufager, Prof. Karsten Reuter, Prof. Michael Zharnikov and Dr. Roman Flesch for the fruitful collaborations.
Prof. Wilfried Wurth and Prof. Dietrich Menzel for sharing their expertise on physisorbed argon and spin-polarized electron transport.
Prof. Oliver Rader, Dr. Silvano Lizzit and Dr. Paolo Lacovig for their support during beamtimes at Bessy and Elettra.
My colleagues Runyuan Han and Johannes Bauer for providing help during the beamtimes and spending much time in the lab together, as well as during discussions in the office.
Katharina Diller and Dr. Florian Klappenberger, who provided very useful data analysis programs together with free 24/7 support!
Dr. Daniel Gerster, Dr. Francesco Allegretti and Lisa Blobner for proofreading my thesis and for providing helpful suggestions.
My office mates Tobias Kaposi, Runyuan Han and Nacho Urgel for establishing a very nice working atmosphere at all times!
My "second" office mates, Daniel Gerster, Claudia Majer, Matthias Marschall, Knud Seufert, Wolfgang Krenner, Richard Steinacher, Dirk Kühne, Sebastian Jakob, Felix Bischoff and their successors, for providing a place to hide, chat and drink coffee, and for becoming friends outside work.
Karl Kölbl, Karl Eberle, Reinhold Schneider, Kamila Wilson and Viktoria Blascheck for making almost everything available that is needed for efficient working!
All the other people I forgot to mention, and the entire crew of E20!

Last but not least, I am deeply indebted to my family and to my wife Lisa for always being there for me in good and not-so-good times and for giving me a shoulder to lean on!